Single Molecule Spin valves

Zur Erlangung des akademischen Grades eines
DOKTORS DER NATURWISSENSCHAFTEN (Dr. rer. nat.)
von der KIT-Fakultät für Physik des
Karlsruher Instituts für Technologie (KIT)

angenommene

DISSERTATION

von

M.Sc. Olivares Peña, Jorge Enrique
aus Mexiko Stadt

Tag der mündlichen Prüfung:	24.06.2022
Referent:	Prof. Dr. Wolfgang Wenzel
Korreferent:	Prof. Dr. Markus Garst

Abstract

Transport in the frame of the Landauer formalism for the single particle case is examined for carbon nanotubes decorated with magnetic molecules. Non-standard ab-initio calculations using constrained density functional theory to ensure the correct charge and magnetization densities are performed. Density functional calculations are performed on magnetic molecules in different spatial configurations: gas phase, crystal phase, and compound; the latter configuration type corresponds to a close-to-experiment system in which magnetic molecules are attached to a non-magnetic one. Based on the magnetization of the sitting molecules, two different magnetic states are examined. They are termed as *antiparallel* and *parallel* cases. They correspond to the experimental realizations shown elsewhere. The Kohn-Sham matrices, which are the result of the density functional simulations, are then used as an input for the transmission simulations which is performed using the Landauer formalism. Two transmission spectra are calculated corresponding to the alpha and beta spin channels per simulation. Differential conductance maps show a higher conductance for the parallel case compared to the antiparallel one for all the gate voltages where the conductance is different from zero. An empirical model is presented which mimics the real systems' behaviour. It consists on a spin polarized tight-binding chain with two atoms per site where two defects are added to the central region simulating the real magnets. To model the CNT small bandgap, two orbitals per atom site were used. Similar results to those of the real system are calculated. It was found that the reason of the difference in conductance between one spin state and the other is that in the parallel case, the transmission for alpha and beta spin channels around the region of interest overlap giving a total transmission (which is the sum of both spins' transmissions) larger to that of the antiparallel case where the alpha and beta transmissions are separated.

Zusammenfassung

Diese Arbeit befasst sich mit dem spinabhängigen Transports durch Nanosysteme. Insbesondere fokussieren wir uns dabei auf die Leitfähigkeit von Kohlenstoffnanoröhren, auf welchen Einzelmolekülmagneten angebracht wurden. Das Ziel dieser Arbeit ist den Spin-Ventil-Mechanismus, welcher in Kohlenstoffnanoröhren und Einzelmolekülmagneten gemessen wurde, zu erklären. Hierfür benutzen wir die Dichtefunktionaltheorie in einer ihrer verschiedenen Formen: Beschränkte Dichtefunktionaltheorie. CDFT schränkt die Elektrondichte sowie die Magnetisierung eines oder verschiedener Atome eines Moleküls ein. Diese Berechnungen erzeugen die Kohn-Sham Matrizen, welche den eingeschränkten Zustand des Moleküls enthalten. Die Matrizen dienen als Eingabe für den Landauer-Formalismus, wo der Transmissionkoeffizient für jeden Spin-Kanal berechnet wurde.

Zu diesem Zweck wird Kapitel zwei eine kurze aber dennoch vollständig Einführung zu allgemeinen Konzepten und Formeln beinhalten, welche für die Behandlung von Transport in Nanosystemen notwendig ist. Hier stellen wir unter Anderem den Landauer Formalismus mit seinen Hypothesen, Formeln und der Verbindung zu Greensche Funktionen vor. Letztendlich präsentieren wir die sogennante Matrixformulierung der Greenschen Funktion, mit der die Transport-Berechnungen duerchgeführt werden.

Kapitel drei befasst sich mit den Grundlagen der Dichtefunktionaltheorie, welche für Ab-initio Berechnungen benötigt werden.

Der Kern dieser Dissertation ist in Kapitel vier zu finden. Wir beginnen mit der Beschreibung der genutzt Methoden (CDFT + NEGF) für die Berechnung der elektrischen Ströme. Danach beschreiben wir eines der wichtigsten Konzepte für Quantumchemiesoftware, nämlich dem Basissatz, welcher im Rahmen dieser Arbeit untersucht wird. Der Einfluss des Spektrums von Kohlenstoffnanoröhren wird diskutiert.

Danach, eine Einleitung zur Molekularen Elektronik, Feldeffekttransistoren und Einzelmolekülmagneten sowie DFT Ergebnisse von den Magnetenarten, welche in dieser Arbeit untersucht werden. Terbium/Yttrium Phthalocyanine SMMs in Gasphase sowie deren Kristallstruktur werden präsentiert und ihre geometrische und magnetischen Eigenschaften dargestellt. Hier veranschaulichen wir, wie die CDFT die Konvergenz einer üblichen DFT-Rechnung verbessert.

Danach werden die Transport-Simulationen von echten Systemen, die aus (9, 0) CNT + 1 SMM und (9, 0) CNT + 2 SMMs bestehen, beschreiben. Zwei Simulationsarten werden untersucht: die erste entspricht einer antiparallelen Orientierung (FE-AF) von den Magneten Spin Liganden. Die

zweite zeigt eine parallele Orientierung (FE-FE) desselben Spins. Wir berichten, dass der Spin-Ventil-Mechanismus eine Konsequenz der unterschiedlichen Energieniveauanordnung zwischen den FE-AF und FE-FE Zuständen ist. Im Fall von FE-AF, der Transmissionkoeffizient für Alpha ('Spin hoch') und Beta ('Spin runter') Kanälen innerhalb das sogennante Fermi Fenster zeigen Spitzen bei verschiedenen Energien, wogegen im FE-FE Fall beide Spitzen bei derselbe Energie überlappen. Dieses Verhalten bleibt für die meisten Steuerspannungen bestehen, bei denen die Leitfähigkeit nicht verschwindet. Zu diesem Zweck, haben wir ein Spielzeugmodell entwickelt, welches einer Tight-Binding-Kette mit zwei Defekten in die zentrale Umgebung entspricht. Um die Bandlücke des CNT nachzuahmen, wurden zwei Orbitale pro Stelle benutzt.

Contents

1. Introduction

Molecular electronics is the miniaturization of the components of electrical circuits, and hence the electrical currents through systems are modulated by single atoms or molecules [1]. Molecular electronics have been an active field of reasearch for almost 50 years [2, 3]. As per-se, molecular electronics is a big branch of nanotechnology, it includes the design, synthesis, characterization and theoretical explanation of nanoelectronics such as switches, transistors, memory devices, rectifiers and a whole bunch of other interesting electrical components [1, 4, 5].

Even though the ideas of using single molecules as the building blocks of electronics is not new, the technological capabilities to fabricate as well as the computational resources to simulate them has been reached only in the past 20 years. For instance, the first system in which the transport on a molecular junction was measured that consisted on a metal-molecule-metal structure in which benzene-1,4-dithiol sticked to gold electrodes separated ~ 8 Å and in which the current as well as the conductance were measured as a function of a bias voltage, dates from 1997 [6].

On the other hand, spintronics, which is another branch of nanotechnology, is a relatively young branch dating from 1985 when Johnson and Silsbee [7] measured spin transport in a paramagnetic-ferromagnetic metal interface. Another great advance towards using the electronic spin as a degree of freedom in nanosystems was the observation of giant magnetoresistance in antiferromagnetic coupled (001)Fe/(001)Cr superlattices by Baibich et al. [8].

In the present work, we adress the problem of spin modulated transport in carbon nanotubes. The magnetic properties of the system are given by the magnetic molecules attached to the carbon nanotube. Thus, the transport is a spin polarized, ballistic problem which is treated in a mean-field level using first principles calculations and Landauer formalism.

The thesis is organized as follows: Chapter 2 is dedicated to give a rough but to certain extent complete idea of the type of systems we are going to work with; it also underlines basic concepts necessary for understanding the charge transport in systems where the quantum effects predominate. Landauer formalism is also introduced in this section and three central quantities are defined and explained: the Green's function, the density of states and the transmission coefficient.

Chapter 3 deals with the ab-initio method used to simulate our nanosystems in an atomistic scale: the density functional theory. Three different schemes are presented to understand the advantages and limitations of them.

Finally, chapter 4 presents the results of the DFT simulations in single molecule magnets in several configurations that go from gas phase to crystal arrangements. The ab-initio as well as the transport simulations performed on several systems ranging from bare carbon nanotubes to decorated (with magnetic molecules) carbon nanotubes. An explanation to the spin-valve effects on such a systems is provided using an empirical model which mimics the real systems.

2. Electrical current through nanosystems

This chapter introduces the concepts of electronic current through nanosystems. The way we attack the problem of electron transport in nanosystems is by first presenting general ideas / justifications of why our systems fall into the category of nanosystems and thus, why we will be able to use the formalism described in later chapters. Afterwards, a general picture of the type of physical configurations we are going to deal with in this thesis is presented together with a physical explanation of the current through a nanosystem. Then, fundamental concepts such as the density of states for different dimensions as well as its interpretation is shortly discussed. Once we have establish some preliminary concepts, we explore the Schrödinger equation for single particle Hamiltonians which introduces naturally the concept of bands and channels. Then, using all that knowledge, the quantization of the conductance is studied in a heuristic level.
This completes the part of fundamental concepts in electronic transport which we then can use for the upcoming sections: the Landauer approach and the Green's function formalism from which the transmission can then be calculated.

1. Nanosystems: characteristic lengths

To begin with a study of how the electric currents behave in nanosystems, we must first give a picture to what we refer to a nanosystem. The obvious answer is: a physical system whose spatial dimensions range from the size of an atom to the nano scale regime (1×10^{-9} m) [9], but we can say a bit more about it. When talking about nanosystems, characteristic lenghts have to be discussed. A big difference between conductors in the macroscale and nanoscale is that the formers present ohmic behaviour while the laters don't. In order for a conductor to show non-ohmic behaviour, its physical dimensions have to be shorter than 3 characteristic lengths: the de Broglie wavelength, the mean free path and the phase-coherence length [9, 10, 11]. The de Broglie wavelength is defined as the inverse of the Fermi wavenumber [10]

$$\lambda = \frac{2\pi}{k}. \tag{2.1}$$

At the same time, the Fermi wavenumber can be obtained from the Fermi velocity (which can be calculated using the energy dispersion relation of a system)

$$v_f = \frac{\hbar k_f}{m^*} \tag{2.2}$$

with $\hbar$ the reduced Planck constant and m^* the effective mass of the electrons in the system under consideration and depends on the energy dispersion relation.
As an example, let us take carbon nanotubes (which are in principle 1 dimensional structures); in this case, the effective mass is related to the bandgap of the carbon nanotube as follows [12]

$$m^* = \frac{E_g}{7.3eV} m_e \tag{2.3}$$

with m_e the electron mass. The value for the Fermi velocity on graphene, as well as for carbon nanotubes (which can be regarded as folded graphene nanoribbons), can be calculated from tight binging approaches [13, 14] or from experiments like ballistic electron resonance [15]. In the low energy regime its value is $v_f = 8.0 \times 10^{-5}$ m/s [12, 14, 16]. Substituting the values for the electron mass, the Fermi velocity and $\hbar$ into equation 2.2 we get a value for the Fermi wavenumber for carbon nanotubes of $k_f = 1.36 \times 10^6$ m^{-1} which finally gives a value for the de Broglie wavenumber of $\lambda = 4619$ nm.
The mean free path (λ_m) is defined as the average distance that a particle travels through a material before its energy and momentum change with respect to its initial values. Mathematically is expressed as

$$\lambda_m = v_f \tau_m \tag{2.4}$$

where τ_m is energy (or momentum) relaxation time. In the case of quasi-metallic cabron nanotubes, the mean free path can have values up to $\lambda_m = 20000$ nm [15].
Finally, a somehow more complicated concept is the phase-coherence length λ_ϕ. It can be regarded as the distance over which the electron wavefunction retains its phase coherence and it can be expressed as

$$\lambda_\phi = v_f \tau_\phi \tag{2.5}$$

where τ_ϕ is the phase relaxation time.
For example, when we refer to phase coherent transport, we are assuming that the time-dependent wavefunction of the electron has a simple oscillatory behaviour over the whole time evolution (with constant frequency) [9]. Of course, such a situation could only happen on a perfect crystal with no impurities, no lattice vibrations (which also interact with electrons thus changing their phases) and electron-electron interactions. Hence, one can say that, the phase of an electron is just altered by fluctuating scatterers [10]. In the case of metallic carbon nanotubes, τ_ϕ can be measured by four probe transport experiments which give estimate values at $T = 1$ K of $\tau_\phi \sim [1 - 10]$ ps. Introducing this value and the Fermi velocity on equation 2.5 we get a value for the phase-coherence length of $\lambda_\phi = 5810$ nm.

All the previously discussed characteristic lengths, are way larger than the systems considered on this work, justifying the methods used to describe the transport properties of our molecules.

2. A general description of our nanosystems

This thesis will consider nanomolecules which will comprise mainly three parts: two *reservoirs* connected by a *junction*. The electrons will then travel from one of the reservoirs to the other via the junction which can be a single atom or a molecule. The definition of a reservoir can vary from author to author, but in the most simplistic picture, a reservoir is a system that supplies or receives any number of charge carriers and energy without changing its internal state. In reality, ideal reservoirs which means infinitely large systems that can provide electrons and energy indefinitely without any energy loss, do not exist. Therefore, one usually refers to the concept of *electrodes* which are finite reservoirs charged differently (for instance positive and negative). The device that charges the surface of the electrodes is called *battery*. It is important to mention that the electrodes define also the confinement potential of the electrons travelling through the system, thus the geometry of the electrodes plays an important role. This different charge in the electrodes, is the reason why we can measure current through the junction (more of this will become transparent in the next chapters.) We then state that in general, *electronic transport is a non-equilibrium problem* and because of this, attention has to be put on not only properly describing the junction but the effect of the electrodes on it.

2.1. Quantum Wire and Quantum Dot

At this point we have information about the size of the systems we are interested in and the general physical systems we are going to discuss in the next sections. Now we describe more specific electronic features of the molecules into consideration. As the dimensions of the sample reduce, the energy levels resemble more a discrete spectra rather than a continuum. This is usually refered to *size quantization* [17]. When we talk about confinement we mean that the movement of the electrons is restricted in some specific direction(s). For example, if there is no size quantization on a sample, then the electrons are free to move in x-, y- and z-directions; in this case we have a homogeneous solid. Size quantization can occur in one, two or the three spatial directions, and depending on it one refers to a *quantum well* (confinement on one spatial dimension), *quantum wire* (confinement on two spatial dimensions) or *quantum dot* (confinement on three dimensions).
The density of states (DOS) is an important quantity that can be measured experimentally and reflects the effects of the size quantization. In the physics of semiconductors it is defined as the number of eigenstates per unit energy range. The general form of the DOS for the different dimensionalities are [18]

1. For 3-dimensions: $N(E) = \dfrac{m^* \sqrt{2m^* E}}{\pi^2 \hbar^3}$
2. For 2-dimensions (confinement in x-direction): $N(E) = \dfrac{m^* i}{\pi \hbar^2 L_x}$
3. For 1-dimensions (confinement in x- and y-directions): $N(E) = \dfrac{\sqrt{2m^*}}{\pi \hbar L_x L_y} \sum_{i,j} (E - E_{i,j})^{-1/2}$
   with $E_{i,j} = \dfrac{\hbar^2 \pi^2}{2m^*} \left(\dfrac{i^2}{L_x^2} + \dfrac{j^2}{L_y^2} \right)$
4. Meanwhile for a 0D system is a continuous independent of the energy:
   $N(E) = \dfrac{2}{L_x L_y L_z} \sum_{i,j,k} \delta(E - E_{i,j,k})$ where $E_{i,j,k} = \dfrac{\hbar^2 \pi^2}{2m^*} \left(\dfrac{i^2}{L_x^2} + \dfrac{j^2}{L_y^2} + \dfrac{k^2}{L_z^2} \right)$

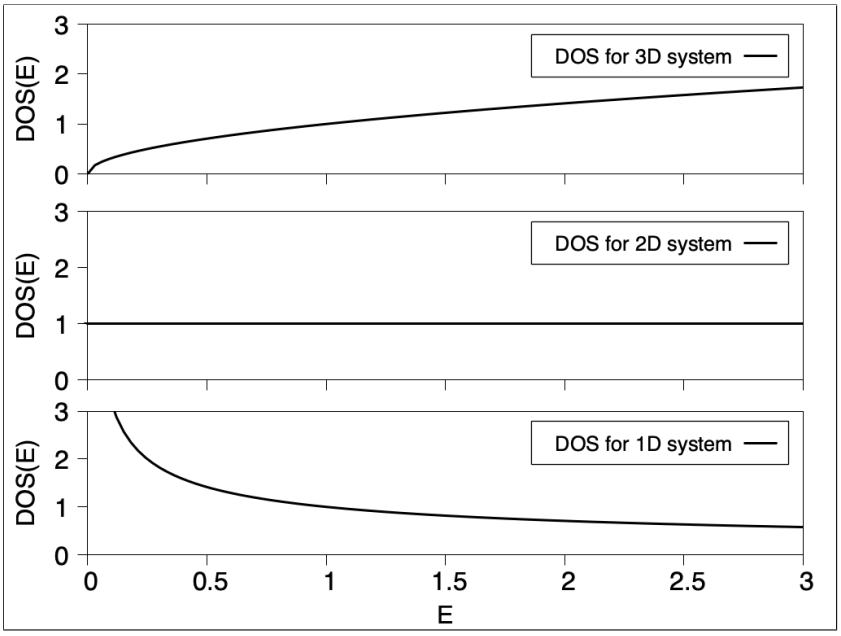

Figure 2.1.: General form of DOS for different a bulk solid, a quantum well and a quantum wire.

The importance of the DOS is that the conduction of a system is closely related to it (nevertheless, it is not the only important quantity in order to observe higher or lower electron transport as we may see later). The density of states is also related to a very interesting concept which we are going to talk in the next section: the *sub-bands*.

2.2. Single particle Hamiltonian in confined systems: Sub-bands

To describe the effects of size quantization in nanosystems, the concept of sub-bands is quite handy to understand the phenomena behind the observed quantities.

To this end, let us consider a very simple system which exists in two dimensions. The electrons are free to move on the x direction but confined by a potential on the y direction which we

denote $U(y)$. We then use the so called effective mass equation which describes the dynamics of the electrons in the conduction band on semiconductors.

$$\left[E_s + \frac{(i\hbar\boldsymbol{\nabla} + e\mathbf{A})^2}{2m} + U(y)\right]\Psi(x,y) = E\Psi(x,y) \tag{2.6}$$

where $\mathbf{A}$ is the vector potential of a magnetic field in the z-direction. $\Psi(x,y)$ the full wavefunction of the electrons in the conductor, m the electron mass and E_s the bottom end of the conduction band. Equation 2.6 differs for instance from the regular Schrödinger equation for periodic solids (i.e. Bloch electrons) in the sense that the lattice potential does not appear on the equation. As a consequence, the wavefunctions obtained by 2.6 are plane waves but not Bloch waves. Since we will not consider explicitely a magnetic field in this work, we can safely make the vector potential $\mathbf{A} = 0$. For random confinement potentials $U(y)$ there are in general no analytical solutions. Nevertheless, in the simple case of a parabollic type potential of the form

$$U(y) = \frac{1}{2}m\omega_0^2 y^2 \tag{2.7}$$

one can obtain analytical expressions. With these considerations, equation 2.6 takes the form

$$\left[E_s + \frac{(i\hbar\boldsymbol{\nabla})^2}{2m} + \frac{1}{2}m\omega_0^2 y^2\right]\Psi(x,y) = E\Psi(x,y) \tag{2.8}$$

we then separate the variables in the x and y components with the Ansatz: $\Psi(x,y) = \phi(x)\phi(y)$ which lead us to

$$\left[E_s + \frac{p_x^2}{2m} + \frac{p_y^2}{2m} + \frac{1}{2}m\omega_0^2 y^2\right]\phi(x)\phi(y) = E\phi(x)\phi(y) \tag{2.9}$$

$p_x = -i\hbar\dfrac{\partial}{\partial x}$ and $p_y = -i\hbar\dfrac{\partial}{\partial y}$.
The x dependent equation in 2.9 is simply the free electron problem which has planewaves as eigenfunctions $\phi(x) = e^{ikx}$ and eigenenergies $E_x = \dfrac{\hbar^2 k_x^2}{2m}$. Thereby, equation 2.8 becomes

$$\left[E_s + \frac{\hbar^2 k_x^2}{2m} + \frac{p_y^2}{2m} + \frac{1}{2}m\omega_0^2 y^2\right]\phi(y) = E\phi(y) \tag{2.10}$$

which is, in principle, the Schrödinger equation for a harmonic potential (with some constant energy terms) with the following solutions

$$\phi_{n_y}(k_y) = H_{n_y}(q), \qquad \text{where} \qquad q = \sqrt{(m\omega_0\hbar)} \tag{2.11}$$

and

$$\boxed{E_n(k_y) = E_s + \frac{\hbar^2 k_x^2}{2m} + \left(n_y + \frac{1}{2}\right)\hbar\omega_0, \quad n_y = 0, 1, 2, ...} \tag{2.12}$$

where H_{n_y} denotes the Hermite polinomial of order n.

The velocity is obtained as usual taking the derivative of the energy with respect to the k-vector:

$$\boxed{v_{n_y}(k_y) = \frac{1}{\hbar}\frac{\partial E_{n_y}(k_y)}{\partial k_y} = \frac{\hbar k_y}{m}.} \tag{2.13}$$

As a side note, in the case when the potential $U(y)$ is zero, but there is a magnetic field $B_y \neq 0$, one can solve the problem in a similar fashion. The bands obtained are the so called *Landau levels*.

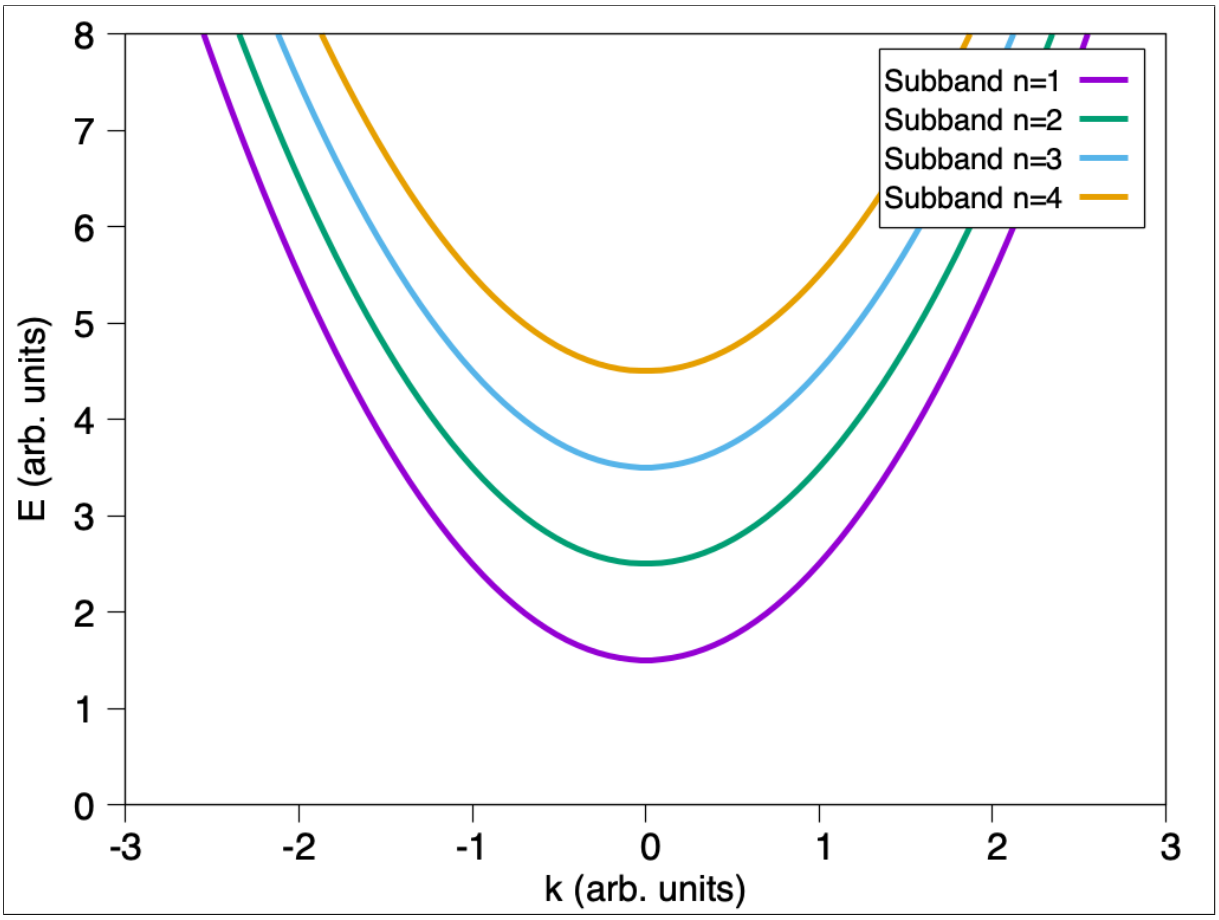

Figure 2.2.: Energy sub-bands defined in Eq. (2.12). $E_s = 0$ and $\hbar\omega_0 = \frac{\hbar^2}{2m} = 1$.

In the case of a quantum well (in a three dimensional system), where one spatial dimension is confined (say the z-direction), we have p-bands

$$E_p(k_x, k_y) \approx E_s + p^2\epsilon_z + \frac{\hbar^2\left(k_x^2 + k_y^2\right)}{2m} \tag{2.14}$$

and for a quantum wire ($y-$ and $z-$confinement)

$$E_{n,p}(k_x) \approx E_s + n^2\epsilon_y + p^2\epsilon_z + \frac{\hbar^2 k_x^2}{2m} \tag{2.15}$$

3. Conductance from transmission

3.1. Resistance in ballistic conductors

Whenever the dimensions of the conductor are larger than the de Broglie wavelength (i.e. macroscopic conductors), then the conductance if given by the Ohm's law

$$G = \frac{\sigma W}{L} \tag{2.16}$$

where the conductivity σ is a material parameter, L is the length of the conductor and W the cross-sectional area. As L would become smaller and smaller (i.e. the mean free path becomes larger than the size of the conductor), one would expect G to growth indefinitely, but this is not the case, instead it approaches a limiting value G_c when the length of the conductor is shorter than the mean free path of the electrons. The resistance arising in such a device, called ballistic conductor, is due to the interface between the conductor and the contact pads. This resistance is given by G_c^{-1} and it is called *contact resistance*.

Our goal now, is to provide an heuristic derivation of the contact resistance in a nano-conductor. Imagine a conductor between two contact pads. Let us name the contacts left and right and allow the current to flow on the x-direction under a small applied bias and small temperatures. We refer to reflectionless contacts to those in which the electrons leave the conductor without suffering reflection.

Electrons travelling from left to right through the conductor will carry a wave vector k_x, that for the purpouses of explanation we can assume they fulfill a dispersion relation like in Fig. (2.2). $+k_x$ states in the conductor are occupied only by electrons originating in the left contact, while $-k_x$ states are occupied only by electrons originating in the right contact.

Let us assume that the quasi-Fermi level, E_f^+, for the $+k$ states is always equal to μ_L even when a bias is applied. Why? Suppose both contacts are at the same potential μ_L, then the Fermi level of a $+k$ state (or any other for that matter) is equal to μ_L. If we change the potential at the right contact to $\mu_L + \delta\mu_R$ there is no effect on the quasi-Fermi level of the left contact, since there is no *causal relationship* between left and right contacts. This means that **no electron originating in the right contact ever makes its way to a $+k$ state**. The same reasoning applies for $-k$ states. Thus, the the current at low temperature and small bias is only due to the electrons in state $+k$ which lie between μ_L and $\mu_R = \mu_L + \delta\mu_R$.

We now proceed to calculate the current on a conductor with one sub-band. We assume that the states $+k$ are filled accordingly to the Fermi distribution function $f^+(E)$.

An uniform electron gas with n electrons per unit length moving with a velocity v (equation (2.13)) carries a current equal to $e \cdot n \cdot v$. Since the electron density associated with a single $k-$state in a conductor of length L_x is $(1/L_x)$ we can write the current I^+ carried by the $+k$ states as

$$I^+ = \frac{e}{L_x} \sum_{k_x} v f^+(E) = \frac{e}{L_x} \sum_{k_x} \frac{1}{\hbar} \frac{\partial E}{\partial k_x} f^+(E) \tag{2.17}$$

which is the current produced by the electrons in one sub-band. Assuming periodic boundary conditions

$$k_x = n_x(2\pi/L_x) \rightarrow dn_x = \frac{dk_x L_x}{2\pi} \tag{2.18}$$

with n_x an integer, and changing the sum to an integral $\sum_{k_x} \rightarrow 2\frac{L_x}{2\pi} \int dk_x$ we get

$$I^+ = \frac{2e}{h} \int_{\epsilon}^{\infty} f^+(E) dE \tag{2.19}$$

The factor of 2 comes from the spin; the integral runs from the cut-off energy on the waveguide mode (see figure 2.3 and the next discussion).

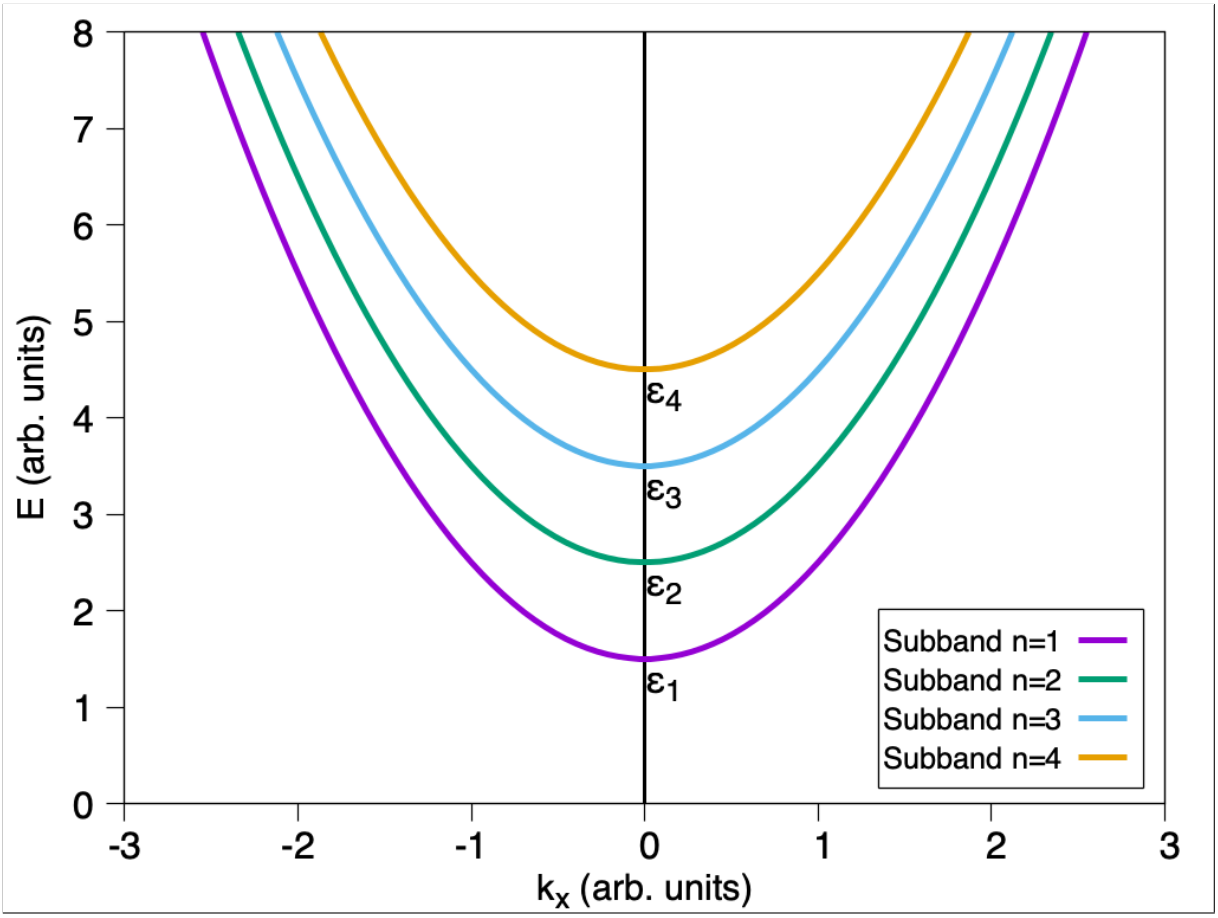

Figure 2.3.: Sub-bands for a conductor. Each sub-band has a dispersion relation $E_n(k_x)$ and a cut-off energy ϵ_n.

The total current due to the electrons with wavenumber $+k_x$ is then the sum of the electrons in all sub-bands. Each sub-band in Fig. (2.3) has a cut-off energy $\epsilon_n = E_n(k_x = 0)$ below which it can not propagate. For an energy E, the number of sub-bands up to E is given by

$$M(E) = \sum_n \Theta(E - \epsilon_n) \tag{2.20}$$

where Θ is the Heavyside function. The quantity $M(E)$ is also termed as the number of channels. Extending equation 2.19 to several modes we get

$$I^+ = \frac{2e}{h} \int_\epsilon^\infty f^+(E) M(E) dE \tag{2.21}$$

If we assume the number of modes M is constant over the energy range $\mu_1 > E > \mu_2$ we can write

$$I = \frac{2e^2}{h} M \frac{\mu_1 - \mu_2}{e} \rightarrow \boxed{G_c = \frac{2e^2}{h} M} \tag{2.22}$$

i.e. the contact resistance is

$$\boxed{G_c^{-1} \equiv \frac{h}{2e^2 M} \approx \frac{12.9k\Omega}{M}} \tag{2.23}$$

from which we can easily see that for a single-mode conductor the resistance is not negligible. The more modes are involved in the conductor, the less contact resistance a conductor has. Also, equation 2.22 defines the well known *quantum of conductance*:

$$\boxed{G_0 = \frac{2e^2}{h}} \tag{2.24}$$

which is a fundamental quantity in the development of the transmission in nanosystems. At an energy E_f a mode can only propagate if $-k_f < k_x < k_f$.
This concludes the part on the preliminary concepts of electrical currents through nanosystems. All of the main ideas treated here will be used on the upcoming sections where we are going to analyse more in detail the specific methods to calculate currents and the conductance of systems in the nanoscale domain.

4. Landauer formalism

In this section we aim to describe the current through a system consisting in 3 parts: a nanojunction connected to two electrodes (left (L) and right (R)) which are open to a reservoir of electrons. The total Hamiltonian of the system can be written as:

$$\hat{H}_{tot} = \hat{H}_S + \hat{H}_{leads} + \hat{H}_{Sb} \tag{2.25}$$

where the Hamiltonians on the right hand side belong to the nanojunction, the leads and the interaction between them, respectively. Landauer formalism is based on the following approximations to solve the transport problem with the Hamiltonian defined in Eq. (2.25):

1. *Open Quantum systems*: The full Hamiltonian of the leads could include different type of interactions that are not possible to describe in a simple manner. For this reason, one usually treats the electrodes as infinite reservoirs of electrons (infinite capacitor). The system is then replaced by a nanojunction 'sandwiched' between two chunks of material with open contact to electron reservoirs. The contacts are characterized by the following properties:

    a) *Electrochemical potential*: In this scope, the electrochemical potential is defined as the energy required to extract an electron from one of the reservoirs and bring it to the system S. In general, the chemical potentials of both reservoirs are different: $\mu_L \neq \mu_R$. (If they are equal, the system is said to be in equilibrium).

b) We define the *voltage bias* by the difference between the chemical potentials

$$eV = \mu_L - \mu_R \tag{2.26}$$

2. *Ideal steady state*: In general, the equation of motion for the density matrix describing the dynamics of the system S, $\rho_S(t)$ is

$$\frac{d\hat{\rho}_S(t)}{dt} = \Big[\hat{H}, \hat{\rho}_S(t)\Big]. \tag{2.27}$$

This differential equation can (or not) have a steady state solution for large times. In fact it doesn't have to have just one solution. We therefore assume that it indeed assumes an unique stationary solution $\hat{\rho}_S^{ss}$. Hence, the system described is *stationary*, this means that the current through the system does not vary in time. In terms of quantum observables we have:

$$\Big\langle \hat{I} \Big\rangle_t = Tr\Big\{\hat{\rho}_S(t)\hat{I}\Big\} \to Tr\Big\{\hat{\rho}_S^{ss}\hat{I}\Big\} = \Big\langle \hat{I} \Big\rangle = constant \tag{2.28}$$

where $\hat{I}$ is the current operator defined as $\hat{I} = \int_S d\mathbf{S}.\hat{\mathbf{j}}(\mathbf{r},t)$ and $\hat{\mathbf{j}}(\mathbf{r},t) = \frac{1}{2}\sum_i \{\delta(\mathbf{r}-\hat{\mathbf{r}}_i), \hat{\mathbf{v}}_i\}$.

3. *Boundary Conditions*: In the new description of the system, the two electrodes play now the role of electron reservoirs. We call them *leads* to differenciate from real reservoirs. Their function is to hold/confine the wave-packets that will flow from one side of the system into the other one. This wave-packets are scattered just in the nanojunction and then move into the next lead. These are known as *scattering boundary conditions.*

4. *Mean Field approximation*: here we assume the system Hamiltonian (S) can be separated into two pieces

$$\hat{H}_S = \hat{H}_{mf} + \hat{V} \tag{2.29}$$

where the $\hat{H}_{mf}$ is a Hamiltonian describing independent electrons (in the mean field approximation), in the presence of ions that do not belong to the nanojunction. $\hat{V}$ is the interaction between electrons (beyond mean-field), in the nanojunction, and the interaction of these electrons with the ions of the junction.

We also assume that the left and right electrons are injected from their correspondent reservoirs with a local equilibrium distribution, accordingly to their electrochemical potential $\mu_{L,R}$. This function is given by the Fermi distribution function

$$f_{L,R}(E) = \frac{1}{e^{(E-\mu_{L,R})/k_BT}+1}. \tag{2.30}$$

4.1. Transmission and reflection probabilities

With the all the approximations already described, we are now ready to solve the Schrödinger equation for the junction described by a Hamiltonian of the type 2.29.
We consider a system whose electronic transport is in the $x-$direction and the confinement potential is transverse to it, i.e. $U(y,z)$. In principle the potential can be of any type, for example the parabollic type in Sec. (2) with energies described by Eq. (2.15). Nonentheless, here we will only assume we have solved the Schrödinger equation for the transversal part of the Hamiltonian in the leads so that the spectrum of the full Schrödinger equation of the leads is:

$$E_i(k_i) = \epsilon_i + \frac{\hbar^2 k_i^2}{2m} \tag{2.31}$$

where ϵ_i are the cutoff energies of the transversal solution part of the full Schrödinger equation (see equation 2.6 and the discussion afterwards.)
Now, for the Hamiltonian of the junction we have

$$\hat{H}_S \Psi_{\alpha,k}(\mathbf{r}) = \left[-\frac{\hbar^2}{2m}\hat{\nabla}^2 + \hat{V}(\mathbf{r}) \right] \Psi_{\alpha k}(\mathbf{r}) = E\Psi_{\alpha k}(\mathbf{r}). \tag{2.32}$$

Consider first the states travelling from the left lead into the right lead. Let us imagine an electron with energy E_i that at $x \to -\infty$ was in an initial state ψ_{ik_i}. The energy of this electron is then: $E_i(k_i) = \epsilon_i + \dfrac{\hbar^2 k_i^2}{2m}$. At the right electrode, the eigenstates have to be a linear combination of transmitted waves:

$$\Psi_{ik_i}(\mathbf{r}) \to \sum_{f=1}^{N_c^R} \mathcal{T}_{if} \psi_{fk_f}(\mathbf{r}) \ , \ x \to +\infty, \tag{2.33}$$

In the same fashion, in the left electrode we do not expect that $\Psi_{ik_i}(\mathbf{r})$ to be simply the incoming wave, but a linear combination of the final states which comprehend the incoming electrons and those reflected back to the left lead at the nanojunction

$$\Psi^+_{ik_i} \to \psi_{ik_i}(\mathbf{r}) + \sum_{f=1}^{N_c^L} \mathscr{R}_{if} \psi_{fk_f}(\mathbf{r}) \tag{2.34}$$

The average current carried by the state at energy E_i can be calculated from the expression for the current density operator $\hat{\mathbf{j}}$ and the current operator through a surface $\mathbf{S}$ perpendicular to the direction of the current flow x

$$\hat{I} = \int_S d\mathbf{S}.\hat{\mathbf{j}}(\mathbf{r},t) \tag{2.35}$$

and it is given by (check [9] for the detailed derivation)

$$I_L(E_i) = I_i(E_i) - \sum_{f=1}^{N_c^L} |\mathscr{R}_{if}|^2 |I_f(E_i)|$$
$$= I_i(E_i)\left(1 - \sum_{f=1}^{N_c^L} R_{if}(E_i)\right) \tag{2.36}$$

where the incident current $I_i(E_i)$ is

$$I_i(E_i) = \frac{e\hbar}{2im}\int_{-\infty}^{\infty} dy \int_{\infty}^{\infty} dz \left[\psi^*_{ik_i}(\mathbf{r})\frac{\partial \psi_{ik_i}(\mathbf{r})}{\partial x} - \psi_{ik_i}(\mathbf{r})\frac{\partial \psi^*_{ik_i}(\mathbf{r})}{\partial x}\right] \tag{2.37}$$
$$= \frac{\hbar k_i}{mL_x} = \frac{v_i(k_i)}{L_x} \tag{2.38}$$

and $v_i(k_i)$ are defined as in 2.13. Similarly, for the currents reflected into the left lead we get

$$I_f(E_i) = \frac{\hbar k_f}{mL_x} = \frac{v_f(k_f)}{L_x}. \tag{2.39}$$

In equation 2.36 we have also named the reflection probability as

$$R_{if}(E_i) \equiv |\mathscr{R}_{if}|^2 \frac{|I_f(E_i)|}{|I_i(E_i)|} \tag{2.40}$$

which is the probability that an incident electron on the left lead with energy $\hbar k_i$ is scattered back into the left lead with energy $\hbar k_f$.

Deep in the right lead we have no reflected electrons and thus we have for the current

$$I_R(E_i) \equiv I_i(E_i) \sum_{f=1}^{N_c^R} T_{if}(E_i) \tag{2.41}$$

where

$$T_{if}(E_i) \equiv |\mathscr{T}_{if}|^2 \frac{|I_f(E_i)|}{|I_i(E_i)|}. \tag{2.42}$$

gives the probability that an electron with wavevector k_i propagates to the right lead to a state with wavenumber k_f.

In an ideal steady state (that we had assumed), the two currents $I_L(E_i)$ and $I_R(E_i)$ have to be identical, therefore we get

$$\sum_{f=1}^{N_c^R} T_{if}(E_i) + \sum_{f=1}^{N_c^L} R_{if}(E_i) = 1 \tag{2.43}$$

An electron originating on the right lead, travelling through the junction and going into the left lead follow the same reasoning, hence we have

$$\sum_{f=1}^{N_c^L} T_{if}(E_i) + \sum_{f=1}^{N_c^R} R_{if}(E_i) = 1. \tag{2.44}$$

Equations 2.43 and 2.44 are the statements of the conservation of particle flux.
Now the job is to find the total current due to the left and right travelling electrons. For this purpouse, we have to take into account all the electron channels, this is, all the different bands that contribute to the current at all energies. The density of states, which is nothing more than the total number of channels (bands) per unit energy is calculated in the usual fashion [19]. Considering periodic boundary conditions, the number of filled states in k space per unit length is given by 2.18

$$k_x = \left(\frac{2\pi}{L_x}\right) n_{i,x}. \tag{2.45}$$

The density of states is the derivative of the number of filled states with respect to the energy

$$D_i(E_i) = \frac{dn_{i,x}}{dE_i} = \frac{L_x}{2\pi}\frac{dk_{i,x}}{dE_i} \tag{2.46}$$

Assuming a parabollic type of dispersion relation (Eq. (2.31)) we get

$$\begin{aligned} D_i(E_i) &= \frac{L_x}{2\pi}\frac{d}{dE_i}\left(\sqrt{\frac{2mE_i}{\hbar^2}}\right) \\ &= \frac{L_x}{2\pi\hbar}\sqrt{2m}\frac{1}{2}E_i^{-1/2} \\ &= \frac{mL_x}{2\pi\hbar\sqrt{2mE_i}} \\ &= \frac{L_x}{2\pi\hbar v_i} \end{aligned} \tag{2.47}$$

Therefore, the net current at any point in space in the conductor is given by the net current of the left incoming electrons minus the right incoming electrons of all possible states i and f

$$\begin{aligned} I &= 2e\int_{-\infty}^{\infty} dE\left[\sum_{i=1}^{N_c^L}\sum_{f=1}^{N_c^R} D_i(E_i)I_i(E_i)T_{if}(E_i) - \sum_{i=1}^{N_c^R}\sum_{f=1}^{N_c^L} D_i(E_i)I_i(E_i)T_{if}(E_i)\right] \\ &= 2e\int_{-\infty}^{\infty} dE\left[\sum_{i=1}^{N_c^L}\sum_{f=1}^{N_c^R} \frac{L_x}{2\pi\hbar v_i}\frac{v_i}{L_x}T_{if}(E_i) - \sum_{i=1}^{N_c^R}\sum_{f=1}^{N_c^L} \frac{L_x}{2\pi\hbar v_i}\frac{v_i}{L_x}T_{if}(E_i)\right] \\ &= 0 \end{aligned} \tag{2.48}$$

which is what one would expect to get if the leads would be identical. Nevertheless, we are missing an important point: we have said that the function of the battery in the system (or the bias), is to keep pumping electrons into the junction and to keep a different chemical potential in both leads. We have also said that the electrons populate the energy levels on the leads accordingly to the Fermi distribution function; thus, to get a non-zero net current through the junction, one needs to multiply each of the terms in 2.48 by its corresponding distribution function. Renaming the integrands in 2.48 to (where we use the conservation of the flux property, so that the transmission coefficient from the left to the right is the same as the one from the right to the left)

$$\mathcal{T} = \sum_{i=1}^{N_c^L} \sum_{f=1}^{N_c^R} T_{if}(E_i) = \sum_{i=1}^{N_c^R} \sum_{f=1}^{N_c^L} T_{if}(E_i) \tag{2.49}$$

we can now obtain the famous Landauer formula

$$\boxed{I = \frac{e}{\pi\hbar} \int_{-\infty}^{+\infty} dE[f_L(E) - f_R(E)]\mathcal{T}(E)} \tag{2.50}$$

Another important result that one can get from this formalism is the the value of the quantum conductance. In the limit of zero bias $\mu_L - \mu_R \to 0$ the chemical potentials of both leads differ by a very small amount that we call ΔE. Taking the limit when the temperature goes to zero, then the Fermi energy of the full system lays in the middle between the chemical potential on the left and right leads. Thus we have

$$\mu_L \approx E_f + \Delta E \tag{2.51}$$

and

$$\mu_R \approx E_f - \Delta E. \tag{2.52}$$

In this limit, we can then expand the transmission coefficient in Taylor series

$$\mathcal{T}(E_f \pm \Delta E) \approx \mathcal{T}(E)|_{E_f} \pm \frac{\partial \mathcal{T}(E)}{\partial E}\Big|_{E_f} \Delta E + \mathcal{O}\big(\Delta E^2\big) \tag{2.53}$$

neglecting the first and higher order terms in ΔE we get

$$\mathcal{T}(E_F) \approx \mathcal{T}(\mu_L) \approx \mathcal{T}(\mu_R). \tag{2.54}$$

Applying a similar procedure for the Fermi functions of left/right leads (i.e. Taylor expansions around the chemical potential of the left/right leads) one gets the following result [9]

$$I = \frac{2e}{h} \int_{-\infty}^{+\infty} dE \left[\left(-\frac{\partial f_{L/R}(E)}{\partial E}\Big|_{\mu_{L/R}} (\mp\mu_L \pm \mu_R) \right) \right] \mathcal{T}(E_f) \tag{2.55}$$

which one can integrate and get as a final result

$$I = \frac{2e^2}{h}\mathcal{T}(E_f)V; \quad \text{when} \quad (\mu_L - \mu_R) \to 0, \quad T \to 0 \tag{2.56}$$

(in 2.56, T denotes the temperature).
Taking the definition of the conductance as the reciprocal of the electrical resistance of a system, and substituting the value for the current 2.56 we get

$$G = \frac{I}{V} = \frac{2e^2}{h}\mathcal{T}(E_f). \tag{2.57}$$

Finally, if we consider perfected transmission $\mathcal{T}(E_f) = 1$, we get the now familiar quantum of conductance

$$G_0 = \frac{2e^2}{h} \tag{2.58}$$

which is consistent with our previous result in Eq. (2.24).

5. Green's function Formalism

Landauer approach to the problem of electronic transport in nanosystems gives us a powerful and elegant tool to calculate the current of (at least in principle) any ballistic nano-device. One just have to get the transmission coefficient and properly apply a bias voltage to calculate the value of the current and conductance at any point of the device (under the assumptions previously dicussed). The question now then is: *How can the transmission coefficient be calculated so that one can use the Landauer formula for computing the current through a nano-device?*
A possible answer to this question is given by another powerful tool not only in the transport problem, but in many other fields of physics and mathematics: the Green's functions.

5.1. Lippmann-Schwinger and Dyson equations

Consider the single particle Hamiltonian for a particle embedded on a spatial mean-field type background potential $V(\mathbf{r})$

$$H_S = \underbrace{-\frac{\hbar^2}{2m}\nabla^2}_{\hat{H}_0} + \underbrace{V(\mathbf{r})}_{\hat{V}}. \tag{2.59}$$

The time dependent Schrödinger equation for this system is

$$\hat{H}_S\,|\Psi(t)\rangle = \left(\hat{H}_0 + \hat{V}\right)|\Psi(t)\rangle = i\hbar\frac{\partial}{\partial t}\,|\Psi(t)\rangle \tag{2.60}$$

where $\Psi(t)$ denote a the time dependent wavefunction of the single particle system. The solution at time t depends on the value of the wavefunction at time $t_0 < t$, and it is usually expressed with the time evolution operator $U(t, t_0)$ and the state at time t_0 when the Hamiltonian does not explicitely depends on time

$$\begin{aligned} |\Psi(t)\rangle &= U(t, t_0)\,|\Psi(t_0)\rangle \\ &= e^{-i\hat{H}(t-t_0)/\hbar}\,|\Psi(t_0)\rangle \end{aligned} \tag{2.61}$$

On the other hand, equation (2.60) has the form

$$\hat{L}\psi(t) = f(t). \tag{2.62}$$

where $\hat{L}$ is a linear hermitian differential operator, which in our case is

$$\hat{L} = i\hbar\frac{\partial}{\partial t} - \hat{H}_S \tag{2.63}$$

The solution for this type of inhomogeneous differential equations is given by the Green's function $\hat{G}(t)$; for Eq. (2.60) we get [20, 21]

$$\left(i\hbar\frac{\partial}{\partial t} - \hat{H}_S\right)\hat{G}^{\pm}(t, t_0) = \hat{1}\delta(t, t_0) \tag{2.64}$$

with boundary conditions

$$\begin{aligned} &\hat{G}^{+}(t, t_0) = 0 \quad t < t_0, \quad \text{retarded} \\ &\hat{G}^{-}(t, t_0) = 0 \quad t > t_0, \quad \text{advanced} \quad . \end{aligned} \tag{2.65}$$

A solution to Eq. (2.64) is given by

$$\hat{G}^{+}(t, t_0) = \begin{cases} -\frac{i}{\hbar}e^{-i\hat{H}_S(t-t_0)/\hbar} & t > t_0, \\ 0 & t < 0 \end{cases} \tag{2.66}$$

and for the advanced Green's function

$$\hat{G}^{-}(t, t_0) = \begin{cases} 0 & t > 0 \\ \frac{i}{\hbar}e^{-i\hat{H}_S(t-t_0)/\hbar} & t < t_0. \end{cases} \tag{2.67}$$

These equations are usually also expressed with the help of the step function

$$\begin{aligned} G^{+}(t,t_0) &= -\frac{i}{\hbar}\theta(t-t_0)e^{-i\hat{H}_S(t-t_0)/\hbar} \\ G^{-}(t,t_0) &= \frac{i}{\hbar}\theta(t_0-t)e^{-i\hat{H}_S(t-t_0)/\hbar} \end{aligned} \tag{2.68}$$

We notice then that the Green's function resembles the time evolution operator of Eq. (2.61) and thus, the solution at time t of 2.60 can be written as

$$|\Psi(t)\rangle = i\hbar G^{+}(t-t_0)\,|\Psi(t_0)\rangle \tag{2.69}$$

for $t > t_0$, and

$$|\Psi(t)\rangle = -i\hbar G^{-}(t-t_0)\,|\Psi(t_0)\rangle \tag{2.70}$$

for $t < t_0$.
Both types of Green's functions are related via the following equality

$$\left[G^{+}(t,t_0)\right]^{\dagger} = G^{-}(t,t_0). \tag{2.71}$$

All the previous considerations can be applied for the free particle Hamiltonian $\hat{H}_0$ in 2.60, and its solutions are the so called *non-interacting* Green's functions

$$\left(i\hbar\frac{\partial}{\partial t} - \hat{H}_0\right)\hat{G}_0^{\pm}(t,t_0) = \hat{1}\delta(t,t_0). \tag{2.72}$$

Substituting Eq. (2.72) into Eq. (2.64) lead us to an equation which relates the non interacting Green's function and the full interacting one. This are called the *Lippmann-Schwinger* equations

$$\boxed{\begin{aligned} \hat{G}^{+}(t-t_0) &= \hat{G}_0^{+}(t-t_0) + \int_{t_0}^{t} dt' \hat{G}^{+}\left(t-t'\right)\hat{V}\hat{G}_0^{+}\left(t'-t_0\right) \\ &= \hat{G}_0^{+}(t-t_0) + \int_{t_0}^{t} dt' \hat{G}_0^{+}\left(t-t'\right)\hat{V}\hat{G}^{+}\left(t'-t_0\right) \end{aligned}} \tag{2.73}$$

and for the advanced Green's function

$$\boxed{\begin{aligned} \hat{G}^{-}(t-t_0) &= \hat{G}_0^{-}(t-t_0) + \int_{t_0}^{t} dt' \hat{G}^{-}\left(t-t'\right)\hat{V}\hat{G}_0^{-}\left(t'-t_0\right) \\ &= \hat{G}_0^{-}(t-t_0) + \int_{t_0}^{t} dt' \hat{G}_0^{-}\left(t-t'\right)\hat{V}\hat{G}^{-}\left(t'-t_0\right) \end{aligned}} \tag{2.74}$$

We can also express equations 2.73 and 2.74 in the energy domain using a Fourier transformation

$$\hat{G}^{+}(E) = \int_{0}^{+\infty} dt e^{iEt/\hbar} e^{-\epsilon t/\hbar} \hat{G}^{+}(t) \tag{2.75}$$

$$\hat{G}^{-}(E) = \int_{-\infty}^{0} dt e^{iEt/\hbar} e^{+\epsilon t/\hbar} \hat{G}^{-}(t) \tag{2.76}$$

where the infinitesimal part ϵ has been added to the integrands to assure the convergence of the integrals. The limit $\epsilon \to 0$ is then taken when the integration has been performed.
Similar relations follow for the free particle Green's functions $\hat{G}_0^{\pm}$. We can replace the value of $\hat{G}^{\pm}(t)$ in 2.75 and 2.76 to get

$$\boxed{\hat{G}^{\pm}(E) = \frac{\hat{1}}{E \pm i\epsilon - \hat{H}_S} = \frac{\hat{1}}{z - \hat{H}_S}} \tag{2.77}$$

for the retarded and advanced Green's functions. $z = E \pm i\epsilon$ has been defined for a shorthand notation. It can be noticed that Green's functions have poles at exactly the eigenvalues of their respective Hamiltonian ($\hat{H}_S$ and $\hat{H}_0$). The Lippmann-Schwinger equation in the energy representation can now be expressed in the following way

$$\boxed{\begin{aligned} \hat{G}^{\pm}(E) &= \hat{G}_0^{\pm}(E) + \hat{G}_0^{\pm}(E)\hat{V}\hat{G}^{\pm}(E) \\ &= \hat{G}_0^{\pm}(E) + \hat{G}^{\pm}(E)\hat{V}\hat{G}_0^{\pm}(E). \end{aligned}} \tag{2.78}$$

In equations 2.73 and 2.74 we can obtain an infinite expansion in powers of $\hat{V}$ in as follows: Assume that in a first approximation, we take as an initial guess for the full Green's function in 2.73 the non-interacting case. Then substituying the new value for G^{+} back in 2.73 we get

$$\begin{aligned} \hat{G}^{+}(t - t_0) = \hat{G}_0^{+}(t - t_0) + \int_{t_0}^{t} dt' \hat{G}_0^{+}\big(t - t'\big)\hat{V}\hat{G}^{+}\big(t' - t_0\big) + \\ \int_{t_0}^{t} dt' \int_{t_0}^{t'} dt'' \hat{G}_0^{+}\big(t - t'\big)\hat{V}\hat{G}^{+}\big(t' - t''\big)\hat{V}\hat{G}_0^{+}\big(t'' - t_0\big). \end{aligned} \tag{2.79}$$

Applying this procedure recursively one gets an infinite expansion of the Green's function in powers of the potential V which will account for all the possible scattering events of a particle travelling from a time t_0 to a time t in the prescence of the potential V. If the series converge we can 'compress' all the contributions due to the potential into the so called *Self-energy* $\hat{\Sigma}^{+}$

$$\hat{G}^{+}(t-t_0) = \hat{G}_0^{+}(t-t_0) + \int_{t_0}^{t} dt' \int_{t_0}^{t'} dt'' \hat{G}_0^{+}\big(t-t'\big)\hat{\Sigma}^{+}\big(t'-t''\big)\hat{G}^{+}\big(t''-t_0\big)$$
$$= \hat{G}_0^{+}(t-t_0) + \int_{t_0}^{t} dt' \int_{t_0}^{t'} dt'' \hat{G}^{+}\big(t-t'\big)\hat{\Sigma}^{+}\big(t'-t''\big)\hat{G}_0^{+}\big(t''-t_0\big). \tag{2.80}$$

This equation is known as *the Dyson* equation. It provides an elegant connection between a full interacting Green's function and a non-interacting one by means of an effective quantity which embraces all the possible interactions between a particle and an external potential. Naturally it is defined in an analogous way for the advanced Green's function. Notice that, equation (2.80) contains implicitely the full series expansion in the potential term $\hat{V}$. In the case of single particle, mean field approximation, the self energy reduces itself to $\hat{\Sigma}(t'-t'') = \hat{V}\delta(t'-t'')$; with this, the integral over dt'' in Eq. (2.80) vanishes and we end up with the Lippmann-Schwinger equation (2.73). Fourier transforming the Dyson equation into the energy domain, we get

$$\boxed{\hat{G}(E) = \hat{G}_0(E) + \hat{G}(E)\hat{\Sigma}(E)\hat{G}_0(E).} \tag{2.81}$$

Let's just give a couple more of important relations in connection with Green's functions. The so-called spectral representation is the projection over a complete set of basis functions for, e.g., the Hamiltonian $\hat{H}_S$ which we write as

$$\hat{1} = \sum_{E_i\alpha} |\Psi_{E_i\alpha}\rangle \langle\Psi_{E_i\alpha}| + \sum_{\alpha} \int_0^{\infty} dE\, |\Psi_{E\alpha}\rangle \langle\Psi_{E\alpha}|\,; \tag{2.82}$$

where α stands for any quantum number of the systems' Hamiltonian; Eq. (2.82) contains a discrete part (if any) and a continuous part (if any) of the spectrum.
With this basis we can project equation 2.77

$$\hat{G}(z) = \sum_{E_i\alpha} \frac{|\Psi_{E_i\alpha}\rangle \langle\Psi_{E_i\alpha}|}{z-E_i} + \sum_{\alpha} \int_0^{+\infty} dE \frac{|\Psi_{E\alpha}\rangle \langle\Psi_{E\alpha}|}{z-E}, \tag{2.83}$$

this is called the spectral representation of the Green's function.
The spectral function is defined as

$$A(E) = i\Big[\hat{G}^{+}(E) - \hat{G}^{-}(E)\Big] \tag{2.84}$$

in which we can use relation 2.71 to write the spectral function in terms of one type of Green's function

$$
\begin{aligned}
\hat{A}(E) &= i\Big[\hat{G}^{+}(E) - \hat{G}^{+\dagger}(E)\Big] \\
&= i\left(\frac{1}{E + i\epsilon - \hat{H}} - \frac{1}{E - i\epsilon - \hat{H}}\right) \\
&= i\sum_{E_i\alpha} |\Psi_{E_i\alpha}\rangle \langle\Psi_{E_i\alpha}| \left(\frac{1}{E + i\epsilon - E_i} - \frac{1}{E - i\epsilon - E_i}\right) \\
&= \sum_{E_i\alpha} |\Psi_{E_i\alpha}\rangle \langle\Psi_{E_i\alpha}| \left(\frac{2\epsilon}{(E + i\epsilon - E_i)(E - i\epsilon - E_i)}\right) \\
&= 2\sum_{E_i\alpha} |\Psi_{E_i\alpha}\rangle \langle\Psi_{E_i\alpha}| \left(\frac{\epsilon}{(E - E_i)^2 + \epsilon^2}\right) \\
&= 2\pi\sum_{E_i\alpha} \delta(E - E_i) |\Psi_{E_i\alpha}\rangle \langle\Psi_{E_i\alpha}| \qquad (2.85)
\end{aligned}
$$

where we have used equation 2.83 in the third line and the definition of the delta function $\delta(x) = \frac{1}{\pi}\frac{\epsilon}{x^2 + \epsilon^2}$ in the last line [22]. Equation 2.85 basically counts all the eigenvalues of an arbitrary Hamiltonian $\hat{H}$ and thus, the spectral function is closely related to the density of states

$$
\begin{aligned}
\hat{D}(E) &= i\lim_{\epsilon\to 0} \frac{\hat{G}^{+}(E) - \hat{G}^{-}(E)}{2\pi} \qquad (2.86) \\
&= \frac{1}{2\pi}\hat{A}(E) \qquad (2.87)
\end{aligned}
$$

This density of states operator can be evaluated in any given basis like in the position representation; in that case we get

$$
\begin{aligned}
\Big\langle \mathbf{r}\Big|\hat{D}(E)\Big|\mathbf{r}\Big\rangle &= i\lim_{\epsilon\to 0} \frac{G^{+}(\mathbf{r},\mathbf{r},E) - G^{-}(\mathbf{r},\mathbf{r},E))}{2\pi} \qquad (2.88) \\
&= -\frac{1}{\pi}\mathrm{Im}\big[G^{+}(\mathbf{r},\mathbf{r},E)\big] \qquad (2.89)
\end{aligned}
$$

which defines the *local density of states.*

6. Matrix formulation of the Green's function

In general, a Hamiltonian $\hat{H}$ can be brought to its matrix form considering a set of complete orthogonal basis $\sum_i |i\rangle$ in the Hilbert space of $\hat{H}$

$$\mathbf{H} = \sum_{ij} |i\rangle \, \hat{H} \, \langle j| \, . \tag{2.90}$$

Bold letters now denote matrices. In this scope, the matrix equation of the Green's function is [21]

$$[(E \pm i\epsilon)\mathbf{I} - \mathbf{H}]\mathbf{G}^{\pm} = \mathbf{I} \tag{2.91}$$

$$\mathbf{G}^{\pm} = [(E \pm i\epsilon)\mathbf{I} - \mathbf{H}]^{-1}, \tag{2.92}$$

where $\mathbf{I}$ is the identity matrix.
All the properties we have already discussed in Section (5.1) are valid also for the matrix formulation. Our goal now is to obtain an expression for the transmission coefficient $\mathcal{T}(E)$ that can be used in computation of real systems to calculate the current and conductance by means of the Landauer formula.
Our system consist of two electrodes and a junction that could be, for example a molecule. The full Hamiltonian matrix can be then divided into three main parts:

- Left, right and central region Hamiltonians that we will write as: $\mathbf{H}_L$, $\mathbf{H}_R$ and $\mathbf{H}_C$.

We also consider that the leads are infinite and tight-binding type. There are two different types of interaction terms in this treatment: the interaction between central and left/right leads and the interactions between left and right electrodes. The coupling between the central region and the leads is denoted by $\mathbf{V}_{iC}$ where $i = L/R$. For the second type of interaction, namely the potential between right and left leads, we assume that effects like screening can be neglected and therefore there is no direct coupling between them.
The complete Hamiltonian matrix defining our system looks like

$$\mathbf{H} = \begin{pmatrix} \mathbf{H}_L & \mathbf{V}_{LC} & \mathbf{0} \\ \mathbf{V}_{LC}^{\dagger} & \mathbf{H}_C & \mathbf{V}_{RC}^{\dagger} \\ \mathbf{0} & \mathbf{V}_{RC} & \mathbf{H}_R \end{pmatrix}, \tag{2.93}$$

which substituted into Eq. (2.91) give us the following matrix equation

$$\begin{bmatrix} (E\pm i\epsilon)\mathbf{I}-\mathbf{H}_L & -\mathbf{V}_{LC} & \mathbf{0} \\ -\mathbf{V}_{LC}^\dagger & (E\pm i\epsilon)\mathbf{I}-\mathbf{H}_C & -\mathbf{V}_{RC}^\dagger \\ \mathbf{0} & -\mathbf{V}_{RC} & (E\pm i\epsilon)\mathbf{I}-\mathbf{H}_R \end{bmatrix} \begin{bmatrix} \mathbf{G}_L^\pm & \mathbf{G}_{LC}^\pm & \mathbf{G}_{LR}^\pm \\ \mathbf{G}_{LC}^\pm & \mathbf{G}_C^\pm & \mathbf{G}_{RC}^\pm \\ \mathbf{G}_{RL}^\pm & \mathbf{G}_{RC}^\pm & \mathbf{G}_R^\pm \end{bmatrix} = \begin{bmatrix} \mathbf{1} & \mathbf{0} & \mathbf{0} \\ \mathbf{0} & \mathbf{1} & \mathbf{0} \\ \mathbf{0} & \mathbf{0} & \mathbf{1} \end{bmatrix}. \tag{2.94}$$

Note that the Green's function now is written in terms of each individual Green's function of the electrodes, central region and interactions between them. We realize that by performing the matrix multiplication in Eq. (2.93), one would get different sets of equations for the left lead system, the right lead system and the central part with the coupling to the leads. Since we are interested in obtaining the Green's function of the junction, we can just take the products of the Hamiltonian matrix with the central terms in Eq. (2.93) (we also use a shortlike notation for the term: $(E\pm i\epsilon)\mathbf{I}=\mathbf{E}$)

$$\begin{aligned} (\mathbf{E}-\mathbf{H}_L)\mathbf{G}_{LC}^\pm \quad & -\mathbf{V}_{LC}\mathbf{G}_C^\pm & & = 0 \\ -\mathbf{V}_{LC}^\dagger\mathbf{G}_{LC}^\pm \quad & +(\mathbf{E}-\mathbf{H}_C)\mathbf{G}_C^\pm & -\mathbf{V}_{RC}^\dagger\mathbf{G}_{RC}^\pm \quad & = 1 \\ & -\mathbf{V}_{RC}\mathbf{G}_C^\pm & +(\mathbf{E}-\mathbf{H}_R)\mathbf{G}_{RC}^\pm & = 0 \end{aligned} \tag{2.95}$$

From the first and third equations we get

$$(\mathbf{E}-\mathbf{H}_L)\mathbf{G}_{LC}^\pm = \mathbf{V}_{LC}\mathbf{G}_C^\pm \quad \rightarrow \quad \mathbf{G}_{LC}^\pm = (\mathbf{E}-\mathbf{H}_L)^{-1}\mathbf{V}_{LC}\mathbf{G}_C^\pm \tag{2.96}$$

$$(\mathbf{E}-\mathbf{H}_R)\mathbf{G}_{RC}^\pm = \mathbf{V}_{RC}\mathbf{G}_C^\pm \quad \rightarrow \quad \mathbf{G}_{RC}^\pm = (\mathbf{E}-\mathbf{H}_R)^{-1}\mathbf{V}_{RC}\mathbf{G}_C^\pm \tag{2.97}$$

Next step is to substitute equations (2.96) and (2.97) into the second line of equation (2.95) to get

$$-\underbrace{\mathbf{V}_{LC}^\dagger(\mathbf{E}-\mathbf{H}_L)^{-1}\mathbf{V}_{LC}}_{\boldsymbol{\Sigma}_L^\pm}\mathbf{G}_C^\pm + (\mathbf{E}-\mathbf{H}_C)\mathbf{G}_C^\pm - \underbrace{\mathbf{V}_{RC}^\dagger(\mathbf{E}-\mathbf{H}_R)^{-1}\mathbf{V}_{RC}}_{\boldsymbol{\Sigma}_R^\pm}\mathbf{G}_C^\pm = 1 \tag{2.98}$$

$$\boxed{\left(\mathbf{E}-\mathbf{H}_C-\boldsymbol{\Sigma}_L^\pm-\boldsymbol{\Sigma}_R^\pm\right)^{-1} = \mathbf{G}^u{\pm}_C}. \tag{2.99}$$

Notice that in Eq. (2.97) we have obtained the matrix form of the self-energy dicussed in the previous chapter $\boldsymbol{\Sigma}_i^\pm$, for the left and right leads, but in here, it is clear what they describe: they contain the influence of the leads on the central Green's function. In other words, the self-energies 'correct' the spectra of the bare central Green's function.

We can further define another useful quantity called *level-width function* or also *Broadening matrix*

$$\mathbf{\Gamma}_{L/R}(E) = i\Big(\mathbf{\Sigma}^{+}_{L/R}(E) - \mathbf{\Sigma}^{-}_{L/R}(E)\Big) = -2\mathrm{Im}\Big(\mathbf{\Sigma}^{+}_{L/R}(E)\Big). \tag{2.100}$$

Using the definition of the self-energy in terms of the coupling matrices (Eq. (2.98)) and the spectral function (Eq. (2.86)) one gets (we omit the label of the leads clarity in the calculation)

$$\begin{aligned}
\mathbf{\Gamma}(E) &= i\big(\mathbf{\Sigma}^{+}(E) - \mathbf{\Sigma}^{-}(E)\big) \\
&= i\Big(\mathbf{V}^{\dagger}\mathbf{G}^{+}(E)\mathbf{V} - \Big(\mathbf{V}^{\dagger}\mathbf{G}^{+}(E)\mathbf{V}\Big)^{\dagger}\Big) \\
&= i\Big(\mathbf{V}^{\dagger}\mathbf{G}^{+}(E)\mathbf{V} - \mathbf{V}^{\dagger}\mathbf{G}^{-}(E)\mathbf{V}\Big) \\
&= \mathbf{V}^{\dagger}\underbrace{i\big[\mathbf{G}^{+}(E) - \mathbf{G}^{-}(E)\big]}_{\mathbf{A}}\mathbf{V} \\
&= \mathbf{V}^{\dagger}\mathbf{A}(E)\mathbf{V}
\end{aligned} \tag{2.101}$$

What we have achieved so far, is to give an explicit matrix expression for the full Green's function of the central part coupled to the leads. Nevertheless, there is still missing an expression for the transmission coefficient appearing in Eq. (2.50).
Let us have a look to the Schrödinger equation

$$\begin{pmatrix} \mathbf{H}_L & \mathbf{V}_{LC} & 0 \\ \mathbf{V}^{\dagger}_{LC} & \mathbf{H}_C & \mathbf{V}^{\dagger}_{RC} \\ 0 & \mathbf{V}_{RC} & \mathbf{H}_R \end{pmatrix} \begin{pmatrix} \mathbf{\Psi}_L \\ \mathbf{\Psi}_C \\ \mathbf{\Psi}_R \end{pmatrix} = E \begin{pmatrix} \mathbf{\Psi}_L \\ \mathbf{\Psi}_C \\ \mathbf{\Psi}_R \end{pmatrix} \tag{2.102}$$

for the left and right leads and the central part. Similarly to the scattering theory approach used on the derivation of the Landauer formula, we state that the solution of the left lead has to have the form of $\mathbf{\Psi}_L = \mathbf{\Psi}^0_L + \mathbf{\Psi}^1_L$, where $\mathbf{\Psi}^0_L$ is an eigenstate of the Hamiltonian $\mathbf{H}^0_L$ (or the state of an electron originating in the left lead) and $\mathbf{\Psi}^1_L$ is the state of the reflected wave. $\mathbf{\Psi}_R$ is the transmitted wave into the right lead. The solution to 2.102 is given by

$$\mathbf{\Psi}_L = \Big(1 + \mathbf{G}^{+}_{0L}\mathbf{V}_{LC}\mathbf{G}^{+}_{C}\mathbf{V}^{\dagger}_{LC}\Big)\mathbf{\Psi}^0_L \tag{2.103}$$

$$\mathbf{\Psi}_R = \mathbf{G}^{+}_{0R}\mathbf{V}_{RC}\mathbf{G}^{+}_{C}\mathbf{V}^{\dagger}_{LC}\mathbf{\Psi}^0_L \tag{2.104}$$

$$\mathbf{\Psi}_C = \mathbf{G}^{+}_{C}\mathbf{V}^{\dagger}_{LC}\mathbf{\Psi}^0_L \tag{2.105}$$

with their correspondent adjoint terms written as

$$\boldsymbol{\Psi}_L^\dagger = \boldsymbol{\Psi}_L^0\Big(1 + \mathbf{V}_{LC}\mathbf{G}_C^{+\dagger}\mathbf{V}_{LC}^\dagger\mathbf{G}_{0L}^{+\dagger}\Big) \tag{2.106}$$

$$\boldsymbol{\Psi}_R^\dagger = \boldsymbol{\Psi}_L^{0\dagger}\mathbf{V}_{LC}\mathbf{G}_C^{+\dagger}\mathbf{V}_{RC}^\dagger\mathbf{G}_{0R}^{+\dagger} \tag{2.107}$$

$$\boldsymbol{\Psi}_C^\dagger = \boldsymbol{\Psi}_L^{0\dagger}\mathbf{V}_{LC}\mathbf{G}_C^{+\dagger} \tag{2.108}$$

The electric current (at one energy) is given by the relation [21, 23]

$$i_{j=L/R} = \frac{ie}{\hbar}\Big(\boldsymbol{\Psi}_j^\dagger\mathbf{V}_{jC}\boldsymbol{\Psi}_C - \boldsymbol{\Psi}_C^\dagger\mathbf{H}_{jC}^\dagger\boldsymbol{\Psi}_j\Big) \tag{2.109}$$

where j stands for the leads. For instance, if we want to calculate the current on the device from an incoming electron with energy E originating on the right lead we substitute (2.104) and (2.105) (as well as their complex conjugated forms) into Eq. (2.109) to get

$$\begin{aligned}
i_R &= \frac{ie}{\hbar}\Big(\boldsymbol{\Psi}_R^\dagger\mathbf{V}_{RC}\boldsymbol{\Psi}_C - \boldsymbol{\Psi}_C^\dagger\mathbf{H}_{RC}^\dagger\boldsymbol{\Psi}_R\Big) \\
&= \frac{ie}{\hbar}\left(\boldsymbol{\Psi}_L^{0\dagger}\mathbf{V}_{LC}\mathbf{G}_C^{+\dagger}\underbrace{\mathbf{V}_{RC}^\dagger\mathbf{G}_{0R}^{+\dagger}\mathbf{V}_{RC}}_{\boldsymbol{\Sigma}_R^-}\mathbf{G}_C^+\mathbf{V}_{LC}^\dagger\boldsymbol{\Psi}_L^0 - \boldsymbol{\Psi}_L^{0\dagger}\mathbf{V}_{LC}\mathbf{G}_C^{+\dagger}\underbrace{\mathbf{V}_{RC}^\dagger\mathbf{G}_{0R}^{+}\mathbf{V}_{RC}}_{\boldsymbol{\Sigma}_R^+}\mathbf{G}_C^+\mathbf{V}_{LC}^\dagger\boldsymbol{\Psi}_L^0\right) \\
&= \frac{ie}{\hbar}\Big(\boldsymbol{\Psi}_L^{0\dagger}\mathbf{V}_{LC}\mathbf{G}_C^{+\dagger}\boldsymbol{\Sigma}_R^-\mathbf{G}_C^+\mathbf{V}_{LC}^\dagger\boldsymbol{\Psi}_L^0 - \boldsymbol{\Psi}_L^{0\dagger}\mathbf{V}_{LC}\mathbf{G}_C^{+\dagger}\boldsymbol{\Sigma}_R^+\mathbf{G}_C^+\mathbf{V}_{LC}^\dagger\boldsymbol{\Psi}_L^0\Big) \\
&= \frac{ie}{\hbar}\left(\boldsymbol{\Psi}_L^{0\dagger}\mathbf{V}_{LC}\mathbf{G}_C^{+\dagger}\underbrace{\big(\boldsymbol{\Sigma}_R^- - \boldsymbol{\Sigma}_R^+\big)}_{i\boldsymbol{\Gamma}_R}\mathbf{G}_C^+\mathbf{V}_{LC}^\dagger\boldsymbol{\Psi}_L^0\right) \\
&= -\frac{e}{\hbar}\Big(\boldsymbol{\Psi}_L^{0\dagger}\mathbf{V}_{LC}\mathbf{G}_C^{+\dagger}\boldsymbol{\Gamma}_R\mathbf{G}_C^+\mathbf{V}_{LC}^\dagger\boldsymbol{\Psi}_L^0\Big)
\end{aligned} \tag{2.110}$$

where we have used the hermiticity of the Hamiltonian in 2.92 which gives a condition on the coupling matrices

$$\mathbf{V}_{LC} = \mathbf{V}_{LC}^\dagger \quad \text{and} \quad \mathbf{V}_{RC} = \mathbf{V}_{RC}^\dagger \tag{2.111}$$

and also the non-hermiticity of the self-energies which is expressed as

$$\Big(\boldsymbol{\Sigma}_{j=L/R}^+\Big)^\dagger = \boldsymbol{\Sigma}_{j=L/R}^-. \tag{2.112}$$

For the current from the left lead we have a similar relationship as in 2.110

$$i_L = \frac{e}{\hbar}\Big(\boldsymbol{\Psi}_L^{0\dagger}\mathbf{V}_{LC}\mathbf{G}_C^{+\dagger}\boldsymbol{\Gamma}_L\mathbf{G}_C^+\mathbf{V}_{LC}^\dagger\boldsymbol{\Psi}_L^0\Big). \tag{2.113}$$

The total current is the result of adding up the currents of all possible eigenstates with energies (channels) n

$$\begin{aligned}
I_R &= -\frac{e}{\hbar}\sum_n \delta(E-E_n)\Big(\mathbf{\Psi}^{0\dagger}_{L,n}\mathbf{V}_{LC}\mathbf{G}^{+\dagger}_C\mathbf{\Gamma}_R\mathbf{G}^{+}_C\mathbf{V}^{\dagger}_{LC}\mathbf{\Psi}^{0}_{L,n}\Big)\\
&= -\frac{e}{\hbar}\sum_{n,m} \delta(E-E_n)\Big(\mathbf{\Psi}^{0\dagger}_{L,n}\mathbf{V}_{LC}\mathbf{\Psi}_m\mathbf{\Psi}^{\dagger}_m\mathbf{G}^{+\dagger}_C\mathbf{\Gamma}_R\mathbf{G}^{+}_C\mathbf{V}^{\dagger}_{LC}\mathbf{\Psi}^{0}_{L,n}\Big)\\
&= -\frac{e}{\hbar}\sum_{n,m} \delta(E-E_n)\Big(\mathbf{\Psi}^{\dagger}_m\mathbf{G}^{+\dagger}_C\mathbf{\Gamma}_R\mathbf{G}^{+}_C\mathbf{V}^{\dagger}_{LC}\mathbf{\Psi}^{0}_{L,n}\mathbf{\Psi}^{0\dagger}_{L,n}\mathbf{V}_{LC}\mathbf{\Psi}_m\Big)\\
&= -\frac{e}{\hbar}\sum_m \left(\mathbf{\Psi}^{\dagger}_m\mathbf{G}^{+\dagger}_C\mathbf{\Gamma}_R\mathbf{G}^{+}_C\mathbf{V}^{\dagger}_{LC}\underbrace{\left[\sum_n \delta(E-E_n)\mathbf{\Psi}^{0}_{L,n}\mathbf{\Psi}^{0\dagger}_{L,n}\right]}_{\mathbf{A}/2\pi}\mathbf{V}_{LC}\mathbf{\Psi}_m\right)\\
&= -\frac{e}{2\pi\hbar}\sum_m \left(\mathbf{\Psi}^{\dagger}_m\mathbf{G}^{+\dagger}_C\mathbf{\Gamma}_R\mathbf{G}^{+}_C\underbrace{\mathbf{V}^{\dagger}_{LC}\mathbf{A}\mathbf{V}_{LC}}_{\mathbf{\Gamma}_L}\mathbf{\Psi}_m\right)\\
&= -\frac{e}{2\pi\hbar}\sum_m \Big(\mathbf{\Psi}^{\dagger}_m\mathbf{G}^{+\dagger}_C\mathbf{\Gamma}_R\mathbf{G}^{+}_C\mathbf{\Gamma}_L\mathbf{\Psi}_m\Big).
\end{aligned} \tag{2.114}$$

We realize that the sum over the diagonal terms of the matrix multiplication in equation 2.114 is nothing more than the trace. If we then consider that the right lead is populated accordingly to the Fermi distribution function with chemical potential μ_R, we simply multiply the current I_R times $f(E,\mu_R)$ to get

$$I_R = -\frac{e}{2\pi\hbar}f(E,\mu_R)Tr\big(\mathbf{G}^{-}_C\mathbf{\Gamma}_R\mathbf{G}^{+}_C\mathbf{\Gamma}_L\big). \tag{2.115}$$

The total current through the system can be found by substracting the current of the right lead to the one of the left lead. Since both currents fullfil the same matrix equation, the only difference will be on the Fermi functions; hence we write

$$\boxed{I = \frac{e}{\pi\hbar}\int_{-\infty}^{\infty} dE(f(E,\mu_L)-f(E,\mu_R))Tr\big(\mathbf{\Gamma}_L\mathbf{G}^{-}_C\mathbf{\Gamma}_R\mathbf{G}^{+}_C\big),} \tag{2.116}$$

where we have used the invariance of the trace under cyclic permutations. We can immediately relate Eq. (2.116) to the Landauer equation 2.50 if we identify the transmission function as

$$\boxed{\mathcal{T}(E) = Tr\big(\mathbf{\Gamma}_L\mathbf{G}^{-}_C\mathbf{\Gamma}_R\mathbf{G}^{+}_C\big).} \tag{2.117}$$

which is very useful in practice as we shall see later on this work.

3. Density Functional Theory

Density functional theory (DFT), has proven to be a powerful tool to calculate and predict electronic properties in a wide variety of materials, from small molecules to solids. It will allow us to obtain the Hamiltonian matrices to be used in the Landauer formalism described in the previous chapter. Since all the electronic correlations are embedded in the different parts of a DFT calculation, a complete, yet not by any means exhaustive treatment has to be mentioned in this work.

One can introduce the formalism of DFT with the following question: *In the framework of the Born-Oppenheimer approximation, how can the electronic ground state energy of an atom or a molecule can be calculated?* A possible answer to the question in terms of the electronic density was given by Hohenberg and Kohn in 1964 [27] considering a local spin independent potential. They settle down the so called Hohenberg-Kohn theorem which presents a change of paradigm on the variable of interest in the Schödinger equation. The full theory, together with the equations to solve numerically is what we now know as Restricted Kohn-Sham approach (RKS), which has been extensively studied over the decades. Here we present a concise introduction to the theory, necessary to understand the basic simulation process of molecules and solids using DFT.

We start this section presenting the core theorem of DFT and its correspondent proof (also one can check [24, 25, 26] for excellent discussions.)

1. Hohenberg-Kohn Theorem

The Hamiltonian of the system of N identical interacting particles, in our case electrons, embedded in an external field is described in a general form as

$$\hat{H} = \hat{T}_e + \hat{U}_{ee} + \hat{V}_{ext}, \tag{3.1}$$

where $\hat{T}_e$ is the kinetic energy of the electrons, $\hat{V}_{ext}$ is the interaction potential between electrons and the nuclei and $\hat{U}_{ee}$ is the electron-electron interaction. We assume the system's ground state is described by the many-body wave function Ψ and it is non-degenerate. Consequently, the many-body Schrödinger equation reads:

$$\hat{H} \left|\Psi\right\rangle = E_{GS} \left|\Psi\right\rangle . \tag{3.2}$$

One can then postulate [27] that the external potential V_{ext} is an unique functional of the electron density $\rho(\mathbf{r})$ [1], i.e., $V_{ext}[\rho(\mathbf{r})]$ and this correspondance is one-to-one. Therefore, since $\hat{V}_{ext}$ fixes $\hat{H}$, then the many-body ground state is a functional of the density, i.e., the energy of the system (and all its constituent parts) are functionals of the electron density:

$$E_{GS} \rightarrow E_0[\rho(\mathbf{r})] = T[\rho(\mathbf{r})] + U_{ee}[\rho(\mathbf{r})] + V_{ext}[\rho(\mathbf{r})]. \tag{3.3}$$

To prove this unique correspondence let us assume it exists another potential $V_{ext}^{'}$ with a ground state function Ψ' that produces the same ground state density:

$$\begin{aligned} V_{ext}(\mathbf{r}) &\rightarrow \Psi \rightarrow \rho(\mathbf{r}) \\ V'_{ext}(\mathbf{r}) &\rightarrow \Psi' \rightarrow \rho(\mathbf{r}). \end{aligned} \tag{3.4}$$

If the statements in 3.4 are true, then the energy that Ψ' defines is the true ground state energy, and thus we can use the variational principle to express

$$\begin{aligned} E'_0 < \langle\Psi'\big|\hat{H}\big|\Psi'\rangle &= \langle\Psi'\big|\hat{H}'\big|\Psi'\rangle + \langle\Psi'\big|\hat{H} - \hat{H}'\big|\Psi'\rangle \\ &= E'_0 + \langle\Psi'\big|\hat{T} + \hat{U}_{ee} + \hat{V}_{ext} - \hat{T} - \hat{U}_{ee} - \hat{V}'_{ext}\big|\Psi\rangle \\ &= E'_0 + \langle\Psi'\big|\hat{V}_{ext} - \hat{V}'_{ext}\big|\Psi\rangle \end{aligned} \tag{3.5}$$

The same reasoning can be apply to the unprimed variables and get

$$E_0 < E_0 + \langle\Psi'\big|\hat{V}'_{ext} - \hat{V}_{ext}\big|\Psi\rangle. \tag{3.6}$$

Adding equations 3.5 and 3.6 give a clear contradiction

$$E_0 + E'_0 < E_0 + E'_0, \tag{3.7}$$

therefore, $V(\mathbf{r})$ is unique functional of the density $\rho(\mathbf{r})$ concluding the first part of the theorem. Before proceeding with the second part (the proof that the energy minimum corresponds to a specific density) let us analyse the expression in Eq. (3.3).

We first notice that the magnitude of the kinetic energy and the electron-electron repulsion will only depend on the number of particles on the system, the type of interaction and its mathematical form are always the same though; it does not matter if the system is a crystal,

[1] The electron density then would be: $\rho(\mathbf{r}) = N \int |\Psi|^2 d\mathbf{r}$.

molecule or atom. In this sense, they are usually called *universal* and can be brought together in a quantity called *Hohenberg-Kohn* functional $F_{HK}[\rho(\mathbf{r})]$:

$$F_{HK}[\rho(\mathbf{r})] = \left\langle \Psi[\rho(\mathbf{r})] \middle| \hat{T} + \hat{U}_{ee} \middle| \Psi[\rho(\mathbf{r})] \right\rangle = T[\rho(\mathbf{r})] + U_{ee}[\rho(\mathbf{r})]. \tag{3.8}$$

The quantity in Eq. (3.8) is the core of density functional theory. Trying to get and systematically improve a functional that reproduce the real ground state electronic density has been proven to be a work of decades and is continuously under development.

Now we can prove that the energy which results from a certain density is indeed the ground state energy of a system with fixed number of particles $\int d\mathbf{r}\rho(\mathbf{r}) = N$. We start by writing down the energy functional of a trial function Ψ' associated to a potential $V'(\mathbf{r})$ and density $\rho(\mathbf{r})$

$$E_{v'}[\rho(\mathbf{r})] = \langle \Psi'[\rho(\mathbf{r})] \big| \hat{F}_{HK} \big| \Psi'[\rho(\mathbf{r})] \rangle + \langle \Psi'[\rho(\mathbf{r})] \big| \hat{V}' \big| \Psi'[\rho(\mathbf{r})] \rangle \tag{3.9}$$

Using the Rayleigh-Ritz variational principle we can state that this energy is equal or larger than the real ground state energy

$$E_0[\rho_0(\mathbf{r})] \leq E_{v'}[\rho(\mathbf{r})] \tag{3.10}$$

being the case of the equality whenever $\rho(\mathbf{r}) = \rho_0(\mathbf{r})$. But this also means, that one can in principle minimize the energy $E_{v'}$ with respect to the density $\rho(\mathbf{r})$ to obtain the ground state energy.

$$\frac{\delta}{\delta\rho(\mathbf{r})}\left[E_{v'}[\rho(\mathbf{r})] - \mu \int d^3r' \rho(\mathbf{r}')\right] = 0 \tag{3.11}$$

with μ a Lagrange multiplier whose physical meaning will become apparent later on this work. So, the Hohenberg-Kohn theorem gives a new vision to the wave-function based many-body electronic problem. Even though it does not give a way to find the unique and universal functional, it sets the basic formalism that allows the calculation of the ground state energy of a system. The problems of the basis, functionals and minimization, are topics that will be touch in the next few sections. For the moment we center our attention to study more in detail the density variable as well as the equations that actually allow us to compute E_0.

2. Restricted Kohn-Sham Scheme (RKS)

We now want to answer the question: *how can one actually calculate the density $\rho(\mathbf{r})$ for a system with some potential V_0?* Indeed, Hohenberg-Kohn theorem gives proof of the existence of a one-to-one relationship between densities, potentials and wavefunctions and guarantee that the energy functional obtained via certain density is the ground state but it does not tell us how

to build the orbitals, or which functional one should use. The Kohn-Sham equations provide a systematic way of calculating the electron density and find the minimum of the energy for a system with potential v_0. To obtain such equations, let us first consider a non-interacting electron system, such that the term U_{ee} in equation (3.3) is zero. Thus we get:

$$\begin{aligned} E_s[\rho(\mathbf{r})] &= T_s[\rho(\mathbf{r})] - V_s[\rho(\mathbf{r})] \\ &= \frac{\hbar^2}{2m_e}\sum_{i=1}^{N}\left\langle\varphi_i|\hat{\nabla}^2_{i,s}|\varphi_i\right\rangle - \int d^3r\rho(\mathbf{r})v_s[\rho(\mathbf{r})] \end{aligned} \tag{3.12}$$

where the sub-index 's' stands for single particle and and v_s is the single particle external potential that corresponds to a specific density ρ_{v_s} by means of the Hohenberg-Kohn theorem; φ_i are the single particle orbitals that satisfy the Schrödinger equation

$$\left(-\frac{\hbar^2}{2m_e}\nabla^2_{i,s} + v_s\right)\varphi_i(\mathbf{r}) = \epsilon_i\varphi_i(\mathbf{r}). \tag{3.13}$$

It is now important to notice that, in the present case when $U_{ee} = 0$, the system corresponds to the many-body noninteracting problem which has as a solution the Slater determinant constituted from the states (3.13)

$$\Psi_N(\mathbf{x}_1, \mathbf{x}_2, \ldots, \mathbf{x}_N) = \begin{vmatrix} \varphi_1(\mathbf{r}_1) & \varphi_1(\mathbf{r}_2) & \cdots & \varphi_1(\mathbf{r}_N) \\ \varphi_2(\mathbf{r}_1) & \varphi_2(\mathbf{r}_2) & \cdots & \varphi_2(\mathbf{r}_N) \\ \vdots & \vdots & \ddots & \vdots \\ \varphi_N(\mathbf{r}_N) & \varphi_N(\mathbf{r}_2) & \cdots & \varphi_N(\mathbf{r}_N) \end{vmatrix}, \tag{3.14}$$

where $\mathbf{x}_j$ correspond to the mixed variable of particle label i and space coordinates $\mathbf{r}_i$. We then can obtain the ground state electron density of such a system by considering the N lowest single particle states

$$\rho_s(\mathbf{r}) = \sum_{i=1}^{N}|\varphi_i(\mathbf{r})|^2 \tag{3.15}$$

Next, we compare Eqs.(3.9) and (3.12); we realize that for this system, the universal functional is given by simply the noninteracting electron kinetic energy

$$F_{KS}[\rho(\mathbf{r})] = T_s[\rho(\mathbf{r})] \tag{3.16}$$

where we have labelled this special functional as Kohn-Sham (KS) in accordance with the literature. In this fictitious system the ground state energy (E_{0s}) and density (ρ_{0s}) can be found

by minimizing the energy with respect to the density (Eq. (3.11)) by the method of the Lagrange multipliers using the constraint that the total number of electrons $N = \int d^3r'\rho(\mathbf{r}')$ is kept constant; then, the Euler-Lagrange equation can be written as:

$$\frac{\delta E_s[\rho(\mathbf{r})]}{\delta\rho(\mathbf{r})} - \mu N = \frac{\delta T_s[\rho(\mathbf{r})]}{\delta\rho(\mathbf{r})} - v_s[\rho(\mathbf{r})] - \mu N = 0 \tag{3.17}$$

Now, coming back to the interacting problem, the real energy functional E_{v_0} will differ from the Kohn-Sham even on the kinetic energy term. Nonetheless, one can rewrite the full energy functional in a tricky way:

$$\begin{aligned} E_{v_0}[\rho(\mathbf{r})] &= T[\rho(\mathbf{r})] + U_{ee}[\rho(\mathbf{r})] + V_0 \\ &= T[\rho(\mathbf{r})] + T_s[\rho(\mathbf{r})] - T_s[\rho(\mathbf{r})] + \int d\mathbf{r}\rho(\mathbf{r})v_0(\mathbf{r}) \\ &\quad + U_{ee}[\rho(\mathbf{r})] + \frac{1}{2}\int d\mathbf{r}\int d\mathbf{r}'\frac{\rho(\mathbf{r})\rho(\mathbf{r}')}{|\mathbf{r}-\mathbf{r}'|} - \frac{1}{2}\int d\mathbf{r}\int d\mathbf{r}'\frac{\rho(\mathbf{r})\rho(\mathbf{r}')}{|\mathbf{r}-\mathbf{r}'|}. \end{aligned} \tag{3.18}$$

In equation (3.18) we have simply add two zeros to the original energy functional: the first is a noninteracting kinectic term and the second a Hartree energy term which we label E_H. Furthermore, one can regroup some of the terms in (3.18) into a new variable called the exchange-correlation energy:

$$E_{xc}[\rho(\mathbf{r})] = T[\rho(\mathbf{r})] - T_s[\rho(\mathbf{r})] + U_{ee}[\rho(\mathbf{r})] - \frac{1}{2}\int d\mathbf{r}\int d\mathbf{r}'\int \frac{\rho(\mathbf{r})\rho(\mathbf{r})}{|\mathbf{r}-\mathbf{r}'|} \tag{3.19}$$

which replacing it into (3.18) we get

$$E_{v_0}[\rho(\mathbf{r})] = T_s[\rho(\mathbf{r})] + \int d\mathbf{r}\rho(\mathbf{r})v_0(\mathbf{r}) + E_H[\rho(\mathbf{r})] + E_{xc}[\rho(\mathbf{r})]. \tag{3.20}$$

At first glance it seems that one has basically just rewrite Eq. (3.3) in a more fancy way but by looking at expression (3.20) we observe that in the whole energy functional for the interacting system, the only unknown variable is E_{xc} which contains not only the exchange and correlation effects but also the remaining (and not known) kinetic energy of the real system. Once again, minimizing the energy with respect to the density we get the Euler-Lagrange equation for the interacting system

$$\begin{aligned} \frac{\delta E_{v_0}[\rho(\mathbf{r})]}{\delta\rho(\mathbf{r})} - \mu N = \frac{\delta T_s[\rho(\mathbf{r})]}{\delta\rho(\mathbf{r})} + \frac{\delta}{\delta\rho(\mathbf{r})}\int d\mathbf{r}\rho(\mathbf{r})v_0(\mathbf{r}) + \frac{\delta E_H[\rho(\mathbf{r})]}{\delta\rho(\mathbf{r})} + \frac{\delta E_{xc}[\rho(\mathbf{r})]}{\delta\rho(\mathbf{r})} - \mu N = 0 \\ \frac{\delta T_s[\rho(\mathbf{r})]}{\delta\rho(\mathbf{r})} + v_0(\mathbf{r}) + \int d^3r'\frac{\rho(\mathbf{r}')}{|\mathbf{r}-\mathbf{r}'|} + \frac{\delta E_{xc}[\rho(\mathbf{r})]}{\delta\rho(\mathbf{r})} - \mu N = 0. \end{aligned} \tag{3.21}$$

Comparing equations (3.17) and (3.21) we see that the functional derivative of the Kohn-Sham reference system is the same in both cases, thus, we get

$$v_s[\rho(\mathbf{r})] = v_0(\mathbf{r}) + \int d^3r' \frac{\rho(\mathbf{r}')}{|\mathbf{r} - \mathbf{r}'|} + v_{xc}[\rho(\mathbf{r})] \tag{3.22}$$

where we have defined the exchange-correlation potential as

$$v_{xc}[\rho(\mathbf{r})] = \frac{\delta E_{xc}[\rho(\mathbf{r})]}{\delta \rho(\mathbf{r})}. \tag{3.23}$$

And now one can see the real gain on re-writing the full interacting Hamiltonian as in (3.20), because then, the ground state density of the full interacting system can be found by solving the single particle Schrödinger equation (3.13) for the auxiliary Kohn-Sham potential v_s

$$\left(-\frac{\hbar^2}{2m_e}\nabla^2_{i,s} + v_0(\mathbf{r}) + v_H[\rho(\mathbf{r})] + v_{xc}[\rho(\mathbf{r})]\right)\varphi_i(\mathbf{r}) = \epsilon_i \varphi_i(\mathbf{r}). \tag{3.24}$$

that shows, in a clear way, that the full interacting ground state energy could be calculated if one would know the form of the XC potential. Unfortunately, this is unknown and many approximations exist that try to reproduce the experimental data.

3. Unrestricted Kohn-Sham Scheme (UKS)

In the description of molecules and complexes which contain a net spin different from zero and thus the magnetic properties are important quantities to be computed with a resonable accuracy, density functional theory provides a good approach. The purpose of this section is to present an non-exhaustive overview of the non-relativistic theory of the Unrestricted DFT (also called Unrestricted Kohn-Sham Scheme (UKS)). For a more complete and good review check [28]. UKS is a natural extension of the concepts in the previous section for spin dependent orbitals; in this case, the many-body fermionic wave function is a function not only the space coordinates, but the spin variable σ where σ can be either α or β (or spin up or down, respectively)

$$\Psi_N(\mathbf{r}_1, \sigma_1, \mathbf{r}_2, \sigma_2, \ldots, \mathbf{r}_N, \sigma_N) \rightarrow \Psi_N(\mathbf{x}_1, \mathbf{x}_2, \ldots, \mathbf{x}_N) \tag{3.25}$$

where the variable $\mathbf{x}_i = (\mathbf{r}_i, s_i)$ now includes the spin of each particle i.
In this case, the total spin density is therefore a sum of the spin alpha and beta densities

$$\boxed{\rho(\mathbf{r}) = \rho_\alpha(\mathbf{r}) + \rho_\beta(\mathbf{r}) = \sum_{\sigma=\alpha,\beta}\sum_{i=1}^{N_\sigma} |\varphi_{i,\sigma}(\mathbf{r})|^2} \tag{3.26}$$

where the spin orbitals fulfill the spin polarized non-interacting Schrödinger equation

$$\left(-\frac{\hbar^2}{2m}\nabla^2_{i,s} + v_{s,\sigma}(\mathbf{r})\right)\varphi_{i,\sigma}(\mathbf{r}) = \epsilon_{i,\sigma}\varphi_{i,\sigma}(\mathbf{r}). \tag{3.27}$$

Since the choice of the auxiliary Kohn-Sham system potential is not by any means unique, one then can propose a spin dependent Kohn-Sham Hamiltonian which has two different external potentials $v_{s,\alpha}$, $v_{s,\beta}$ and thus we can write the unrestricted-KS Hamiltonian as

$$\hat{H}^{uks}_s = \hat{T}_s + \hat{V}_{s,\alpha} + \hat{V}_{s,\beta} = \sum_i^N \frac{\hbar^2}{2m_e}\nabla^2_{i,s} + \sum_{i=1}^N [v_{s,\alpha}(\mathbf{r}_i)\alpha(s_i) + v_{s,\beta}(\mathbf{r}_i)\beta(s_i)]. \tag{3.28}$$

The functions $\alpha(s_i)$ and $\beta(s_i)$ are defined from the non-relativistic single particle Hamiltonians' wavefunctions (also called *spinors*). A spinor is a 2 component wave function for half-spin particles, and its general form is given by

$$\chi(\mathbf{r},\sigma) = \begin{pmatrix}1\\0\end{pmatrix}\psi_\alpha(\mathbf{r}) + \begin{pmatrix}0\\1\end{pmatrix}\psi_\beta(\mathbf{r}) \tag{3.29}$$

which can also be written as

$$\chi(\mathbf{r},s) = \alpha(s)\psi_\alpha(\mathbf{r}) + \beta(s)\psi_\beta(\mathbf{r}) \tag{3.30}$$

using the following definition:

$$\alpha\left(\frac{1}{2}\right) = 1 \quad \alpha\left(-\frac{1}{2}\right) = 0 \tag{3.31}$$

$$\beta\left(\frac{1}{2}\right) = 0 \quad \beta\left(-\frac{1}{2}\right) = 1. \tag{3.32}$$

In order to obtain the one-electron KS-orbitals, it is then now necessary to separate (3.27) into two equations for each set of orbitals

$$\left[-\frac{\hbar^2}{2m_e}\nabla^2 + v_{s,\alpha}(\mathbf{r})\right]\varphi_{i,\alpha}(\mathbf{r}) = \epsilon_{i,\alpha}\varphi_{i,\alpha}(\mathbf{r}) \tag{3.33}$$

$$\left[-\frac{\hbar^2}{2m_e}\nabla^2 + v_{s,\beta}(\mathbf{r})\right]\varphi_{i,\beta}(\mathbf{r}) = \epsilon_{i,\beta}\varphi_{i,\beta}(\mathbf{r}) \tag{3.34}$$

with the basis fulfilling the orthogonality condition

$$\langle\varphi_{i,\sigma}|\varphi_{j,\sigma}\rangle = \delta_{ij}\delta_{\sigma,\sigma'}. \tag{3.35}$$

Another important quantity in the UKS formalism is the *spin density* which is simply the difference between the α and β densities

$$\boxed{Q(\mathbf{r}) = \sum_{i=1}^{N_\alpha} |\varphi_{i,\alpha}(\mathbf{r})|^2 - \sum_{i=1}^{N_\beta} |\varphi_{i,\beta}(\mathbf{r})|^2.} \tag{3.36}$$

So far, what we have done is simply separate the single particle Hamiltonian, the orbitals and therefore the electron density into two parts. It is then natural to make then the total energy of the reference system 3.12 a functional of the alpha and beta densities

$$E_s^{uks}[\rho_\alpha(\mathbf{r}), \rho_\beta(\mathbf{r})] = T_s^{uks}[\rho_\alpha(\mathbf{r}), \rho_\beta(\mathbf{r})] + \int d^3r \rho_\alpha(\mathbf{r}) v_{s,\alpha} + \int d^3r \rho_\beta(\mathbf{r}) v_{s,\beta} \tag{3.37}$$

which can be then minimized with respect to the spin resolved densities and now the constraint is such that the total number of alpha and beta electrons ($N_\sigma = \int d^3r' \rho_\sigma(\mathbf{r}')$) is conserved. Then the Euler-Lagrange equations read

$$\frac{\delta E_s^{uks}[\rho_\alpha(\mathbf{r}), \rho_\beta(\mathbf{r})]}{\delta \rho_\alpha(\mathbf{r})} - \mu_\alpha N_\alpha = \frac{\delta T_s^{uks}[\rho_\alpha(\mathbf{r}), \rho_\beta(\mathbf{r})]}{\delta \rho_\alpha(\mathbf{r})} + v_{s,\alpha}[\rho_\alpha(\mathbf{r}), \rho_\beta(\mathbf{r})] - \mu_\alpha N_\alpha = 0 \tag{3.38}$$

$$\frac{\delta E_s^{uks}[\rho_\beta(\mathbf{r}), \rho_\beta(\mathbf{r})]}{\delta \rho_\beta(\mathbf{r})} - \mu_\beta N_\beta = \frac{\delta T_s^{uks}[\rho_\alpha(\mathbf{r}), \rho_\beta(\mathbf{r})]}{\delta \rho_\beta(\mathbf{r})} + v_{s,\beta}[\rho_\alpha(\mathbf{r}), \rho_\beta(\mathbf{r})] - \mu_\beta N_\beta = 0 \tag{3.39}$$

and as in the restrcited KS part, the full interacting case can be rewritten in terms of an exchange-correlation functional but now spin dependent: $v_{\sigma,xc}[\rho_\alpha(\mathbf{r}), \rho_\beta(\mathbf{r})]$, and thus, the minimization of the total energy reads

$$\frac{\delta T_s^{uks}[\rho_\alpha(\mathbf{r}), \rho_\beta(\mathbf{r})]}{\delta \rho_\alpha(\mathbf{r})} + v_0(\mathbf{r}) + v_H[\rho(\mathbf{r})] + v_{\alpha,xc}[\rho_\alpha(\mathbf{r}), \rho_\beta(\mathbf{r})] - \mu_\alpha N_\alpha = 0 \tag{3.40}$$

$$\frac{\delta T_s^{uks}[\rho_\alpha(\mathbf{r}), \rho_\beta(\mathbf{r})]}{\delta \rho_\beta(\mathbf{r})} + v_0(\mathbf{r}) + v_H[\rho(\mathbf{r})] + v_{\beta,xc}[\rho_\alpha(\mathbf{r}), \rho_\beta(\mathbf{r})] - \mu_\beta N_\beta = 0. \tag{3.41}$$

Comparing Eqs.(3.38, 3.40) and Eqs.(3.39, 3.41) the Kohn-Sham effective potentials read:

$$v_{s,\alpha}[\rho_\alpha, \rho_\beta] = v_0(\mathbf{r}) + v_H[\rho(\mathbf{r})] + v_{\alpha,xc}[\rho_\alpha(\mathbf{r}), \rho_\beta(\mathbf{r})] \tag{3.42}$$

$$v_{s,\beta}[\rho_\alpha, \rho_\beta] = v_0(\mathbf{r}) + v_H[\rho(\mathbf{r})] + v_{\beta,xc}[\rho_\alpha(\mathbf{r}), \rho_\beta(\mathbf{r})] \tag{3.43}$$

where the spin resolved exchange-correlation potentials are defined as

$$v_{\alpha,xc}[\rho_\alpha(\mathbf{r}),\rho_\beta(\mathbf{r})] = \frac{\delta E_{xc}^{uks}[\rho_\alpha(\mathbf{r}),\rho_\beta(\mathbf{r})]}{\delta\rho_\alpha(\mathbf{r})} \tag{3.44}$$

$$v_{\beta,xc}[\rho_\alpha(\mathbf{r}),\rho_\beta(\mathbf{r})] = \frac{\delta E_{xc}^{uks}[\rho_\alpha(\mathbf{r}),\rho_\beta(\mathbf{r})]}{\delta\rho_\beta(\mathbf{r})}. \tag{3.45}$$

All these results can then be used to set the single particle spin resolved Kohn-Sham equations

$$\left[-\frac{\hbar^2}{2m_e}\nabla_{i,s}^2 + v_0(\mathbf{r}) + v_H[\rho(\mathbf{r})] + v_{\alpha,xc}[\rho_\alpha(\mathbf{r}),\rho_\beta(\mathbf{r})]\right]\varphi_{\alpha,i}(\mathbf{r}) = \epsilon_{\alpha,i}\varphi_{\alpha,i}(\mathbf{r}) \tag{3.46}$$

$$\left[-\frac{\hbar^2}{2m_e}\nabla_{i,s}^2 + v_0(\mathbf{r}) + v_H[\rho(\mathbf{r})] + v_{\beta,xc}[\rho_\alpha(\mathbf{r}),\rho_\beta(\mathbf{r})]\right]\varphi_{\beta,i}(\mathbf{r}) = \epsilon_{\beta,i}\varphi_{\beta,i}(\mathbf{r}). \tag{3.47}$$

Equations (3.47) and (3.46) define then a full set of spin dependent orbitals and eigenvalues (and thus, Kohn-Sham matrices) which will describe, at least in principle, the full interacting electronic system embedded in an external potential $v_0(\mathbf{r})$.

4. Constrained Density Functional Theory (CDFT)

The restricted and unrestricted Kohn-Sham schemes, represent the standard procedures to calculate electronic and spin properties of a wide variety of compounds. For systems with a low number of electrons, the results can be even quantitatively accurate; nevertheless, this is not the case, for instance, of highly correlated molecules which often present a challenge even in the self-consistent procedure. Many of the mathematical tools and reasoning from the previous sections can also be applied to constrained DFT; this is no coincidence since one can actually regard CDFT as a particular case of the more general DFT formalism. The method [29] consist on constraining the electronic state of a system by the means of Lagrange multipliers λ_c where we have used the label c to distinguish it from the usual Lagrange multiplier from DFT discussed on the previous sections. Consider a N-particle system within a volume V, and suppose we know the DFT energy functional $E[\rho(\mathbf{r})]$. The aim of CDFT is then to obtain the system's electronic state with lowest energy whenever it is subject to a electron density constraint. Depending on how the constraint on $\rho(\mathbf{r})$ is performed, one can talk about a *charge* or a *magnetization* type of constraint.

The general structure of a spin dependent constraint term is expressed mathematically as

$$\sum_\sigma \int_V d\mathbf{r} w_c^\sigma(\mathbf{r})\rho_\sigma(\mathbf{r}) - N = 0 \tag{3.48}$$

with the usual spin label σ (α or β) and w^σ a weight function which explicitly defines the type and form of a constraint [30]; the integration is performed over an specific volume V which

contains a fixed number of electrons N. For example, if one would like to constrain the number of particles only, then $w_c^\alpha(\mathbf{r}) = w_c^\beta(\mathbf{r}) = w_c(\mathbf{r})$ and equation (3.48) would turn into

$$\int d\mathbf{r} w_c(\mathbf{r})(\rho_\alpha(\mathbf{r}) + \rho_\beta(\mathbf{r})) - N = 0. \tag{3.49}$$

In the case when a magnetization is desired ($m(\mathbf{r}) = \rho_\alpha(\mathbf{r}) - \rho_\beta(\mathbf{r})$), the weight functions are $w_c^\alpha(\mathbf{r}) = -w_c^\beta(\mathbf{r})$ defining a net electron density difference resulting on a net magnetization

$$\int d\mathbf{r}\Big(w_c^\alpha \rho_\alpha(\mathbf{r}) - w_c^\beta \rho_\beta(\mathbf{r})\Big) - M = 0. \tag{3.50}$$

with $M = \int d^3r(\rho_\alpha(\mathbf{r}) - \rho_\beta(\mathbf{r}))$.
Using the general form of the constraint (3.48), the Kohn-Sham energy functional has now an extra term

$$E^c[\rho(\mathbf{r}), \lambda_c] = E[\rho(\mathbf{r})] + \lambda_c\left(\sum_\sigma \int d\mathbf{r} w_c^\sigma \rho_\sigma(\mathbf{r}) - N\right) \tag{3.51}$$

where the index c denotes CDFT variables. Thus, using equations (3.46) and (3.47) one can write the Constrained Kohn-Sham equations

$$\left[-\frac{\hbar^2}{2m_e}\nabla_{i,s}^2 + v_0(\mathbf{r}) + v_H[\rho(\mathbf{r})] + v_{\alpha,xc}[\rho_\alpha(\mathbf{r}), \rho_\beta(\mathbf{r})] + \lambda_c w_c^\alpha(\mathbf{r})\right]\varphi_{\alpha,i}(\mathbf{r}) = \epsilon_{\alpha,i}\varphi_{\alpha,i}(\mathbf{r}) \tag{3.52}$$

$$\left[-\frac{\hbar^2}{2m_e}\nabla_{i,s}^2 + v_0(\mathbf{r}) + v_H[\rho(\mathbf{r})] + v_{\beta,xc}[\rho_\alpha(\mathbf{r}), \rho_\beta(\mathbf{r})] + \lambda_c w_c^\beta(\mathbf{r})\right]\varphi_{\beta,i}(\mathbf{r}) = \epsilon_{\beta,i}\varphi_{\beta,i}(\mathbf{r}). \tag{3.53}$$

which are nothing more than the regular UKS equations with an extra potential term $w_c^\sigma(\mathbf{r})$.

4. Results

In this chapter we present all the results obtained for the different systems considered through this work: ab-initio calculations of molecular magnets in gas as well as in crystall phase, stand-alone carbon nanotubes and finally the composed system. We first start by introducing our implementation of a carbon nanotube based FET. We present the concept of the gate voltage and how this affects the single particle Hamiltonian. We also explain how the source-drain voltage is applied in our transport simulations. We conclude this section by deriving the explicit mathematical expression which we used for the practical computation of the current through such a system. In *building the system* section, we first present some of the experimental realizations of the objects being studied in this work. This will serve as a guide for the next sections in which we describe how and why we used our approach and why the code was built in such a way. The *method* section links the three first chapters of this thesis (the theory) with the practical implementation of the relevant equations. The section *basis set dependence* presents a very important concept in quantum chemistry software, the atomic basis sets, and how it affects the results in our methodology. The next sections are dedicated to the study of the simulations on real systems. We present results for (C)DFT calculations of SMMs in different magnetic states as well as in different spatial configurations (gas phase and crystal). Afterwards, DFT + NEGF calculations on bare CNTs are shown and how their spectra changes with the choise of the basis set. Finally, the full system consisting of carbon nanotubes decorated with one and two single molecule magnets is investigates through Landauer formalism. The spin-valve mechanism is explained using the real system but also with an empirical model based on a tight-binding Hamiltonian. A comparison between both type of systems is done in the framework of NEGF formalism.

1. Molecular electronics

1.1. Field Effect Transistors (FET)

A field effect transistor (FET) is the physical realization of what we have discussed in previous sections. A FET consists on a *source*, *drain* and *gate* electodes sandwiching a central region called *channel*. The central region corresponds to the nanosystem which we want to study. A schematic representation of such a device is depicted in figure 4.1. In general, the source and the drain electrodes control the current through the system and in equilibrium, they define a

electrochemical (which from now on we will simply call it chemical potential) potential of the whole system: μ; the gate electrode controls the electron density of the channel.

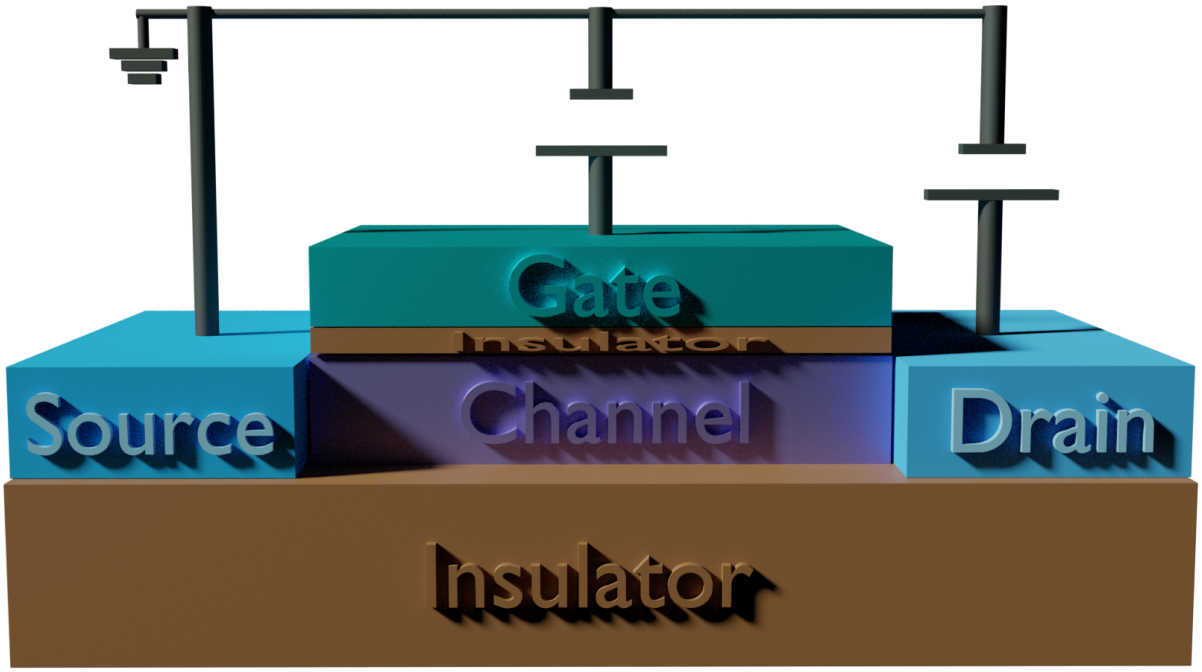

Figure 4.1.: General geometry of a field effect transistor. It consist of three terminal electrodes: source, drain and gate. The channel is the nanosystem which is to be examined. Between the gate and the channel there is an insulating layer which has to be thick enough to no let any current leaking to the gate, but thin enough so that the gate electrode efficiently modifies the electron density on the channel.

There exist two types of FET:

1. *n-type:* a positive voltage $V_g > 0$ is applied to the gate electrode. As a result, the electrons feel attracted to the potential causing their energy to raise (in absolute value) which means that the energy levels in the channel get lowered. This voltage doesn't affect the band structure on the source and drain electrodes and, therefore, the chemical potential μ remains unaffected. The energy levels in the gate, move with respect to μ, letting μ be in the empty band. Mathematically this can be regarded as:

$$H_s = \epsilon_s + U - V_g. \tag{4.1}$$

   In 4.1, H_s is the Hamiltonian of the single particle of the channel, ϵ_s are the energies, U an external potential interaction and V_g is the gate voltage applied to it.

   a) The channel then becomes more conductive.

   b) The threshold gate voltage V_t is the voltage needed to turn the transistor ON. It is determined by the difference between the equilibrium chemical potential μ and the lowest available empty state.

2. *p-type:* A negative gate voltage is applied $V_g < 0$. The chemical potential is driven inside of the filled band and the current raises due to the availability of states.

Notice that **what makes a FET to become more conductive is the availability of states close to the chemical potential $E = \mu$, it doesn't matter if they are empty or filled.** Imagine now that a potential is applied between the source and drain terminals V_{sd}. The effect of this potential is to raise (lower) the energy levels of the source and drain electrodes. The difference of the source and drain chemical potentials is the total bias applied to the system

$$|\mu_s - \mu_d| = q|V_{sd}| \tag{4.2}$$

The probability that an electronic state with energy E at temperature T is occupied by an electron is given by the Fermi statistics

$$f_s(E) = \frac{1}{1 + e^{\frac{(E-\mu_s)}{k_B T}}} \tag{4.3}$$

$$f_d(E) = \frac{1}{1 + e^{\frac{(E-\mu_d)}{k_B T}}}. \tag{4.4}$$

1.2. Practical computation of the current

As we already stated, in equilibrium, the chemical potentials of the source and drain electrodes are the same and correspond to the chemical potential of the whole system:

$$\mu_s = \mu_d = \mu \tag{4.5}$$

If one applies a symmetric bias voltage, then the change on the chemical potentials will be also symmetrical

$$\mu_s = \mu + \frac{eV_{sd}}{2}$$

$$\mu_d = \mu - \frac{eV_{sd}}{2}$$

Therefore, the Fermi distribution functions for each of the electrodes (Eq. (4.3) and Eq. (4.4)) are:

$$f_s(E, V_{sd}) = \frac{1}{1 + e^{\frac{\left(E - \left(\mu + \frac{eV_{sd}}{2}\right)\right)}{k_B T}}} \tag{4.6}$$

$$f_d(E, V_{sd}) = \frac{1}{1 + e^{\frac{\left(E - \left(\mu - \frac{eV_{sd}}{2}\right)\right)}{k_B T}}}. \tag{4.7}$$

Landauer formula (Eq. (2.50)) then depends not only on the energy, but also of the source-drain voltage:

$$I(V_{sd}) = \frac{e}{\pi\hbar} \int_{-\infty}^{\infty} dE\, \mathcal{T}(E) \Big[f_s(E, V_{sd}) - f_d(E, V_{sd}) \Big] \tag{4.8}$$

Since the conductance is the change of the current with respect to the applied bias (V_{sd}), we take the derivative of 4.8 to obtain $G(V_{sd})$[1]:

$$\begin{aligned}
G(V_{sd}) &= \frac{dI(E, V_{sd})}{dV_{sd}}\bigg|_{V_g} \\
&= \frac{q}{\pi\hbar} \int_{-\infty}^{\infty} dE\, \mathcal{T}(E) \left[\frac{df_s(E, \mu_s)}{dV_{sd}} - \frac{df_d(E, \mu_d)}{dV_{sd}} \right] \\
&= \frac{q}{\pi\hbar} \int_{-\infty}^{\infty} dE\, \mathcal{T}(E) \left[\frac{d}{dV_{sd}} \left(\frac{1}{1 + e^{(E - (\mu_S + qV_{sd}/2))/k_B T}} \right) \right. \\
&\qquad \left. - \frac{d}{dV_{sd}} \left(\frac{1}{1 + e^{(E - (\mu_d - qV_{sd}/2))/k_B T}} \right) \right] \\
&= \frac{q}{\pi\hbar} \int_{-\infty}^{\infty} dE\, \mathcal{T}(E) \left[\frac{d}{dV_{sd}} \left(1 + e^{(E - (\mu_s + qV_{sd}/2))/k_B T}\right)^{-1} \right. \\
&\qquad \left. - \frac{d}{dV_{sd}} \left(1 + e^{(E - (\mu_d - qV_{sd}/2))/k_B T}\right)^{-1} \right] \\
&= \frac{q}{\pi\hbar} \int_{-\infty}^{\infty} dE\, \mathcal{T}(E) \left[(-1)\left(1 + e^{(E - (\mu_s + qV_{sd}/2))/k_B T}\right)^{-2} \frac{1}{2k_B T} (-q) e^{(E - (\mu_s + eV_{sd}/2))/k_B T} \right. \\
&\qquad \left. - (-1)\left(1 + e^{(E - (\mu_d - qV_{sd}/2))/k_B T}\right)^{-2} \frac{q}{2k_B T} \left(e^{E - (\mu_d - qV_{sd}/2)/k_B T}\right) \right] \\
&= \frac{q^2}{2\pi\hbar k_B T} \int_{-\infty}^{\infty} dE \mathcal{T}(E) \left[\frac{e^{(E - (\mu_s + qV_{sd}/2))/k_B T}}{\left(1 + e^{(E - (\mu_s + qV_{sd}/2))/k_B T}\right)^2} + \frac{e^{(E - (\mu_d - qV_{sd}/2))/k_B T}}{\left(1 + e^{(E - (\mu_d - qV_{sd}/2))/k_B T}\right)^2} \right]
\end{aligned}$$

$$G(V_{sd}) = \frac{1}{2k_B T} G_0 \int_{-\infty}^{\infty} dE \mathcal{T}(E) \left[\frac{e^{(E - (\mu_s + eV_{sd}/2))/k_B T}}{\left(1 + e^{(E - (\mu_s + eV_{sd}/2))/k_B T}\right)^2} + \frac{e^{(E - (\mu_d - eV_{sd}/2))/k_B T}}{\left(1 + e^{(E - (\mu_d - eV_{sd}/2))/k_B T}\right)^2} \right] \tag{4.9}$$

[1] In the derivation we made the temporary change of variable $e \to q$ to denote the fundamental charge symbol to avoid confusion with the exponential function e.

1.3. Discussion of equation 4.9

One thing to notice about equation 4.9 when implementing it into a computer code is that its analytical form is computationally not the easiest to work with; more precisely, in the limit when $T \to 0$, which is indeed the limit fixed (in our case) by the experimental realization, the integration of such functions are computationally not treactable (due to the machine precision and integration convergence). One walk-around to this problem is to express Eq. (4.9) in terms of a different function that shows better integration convergence for small argument values. Starting from equation 4.9 and changing the argument to

$$[E - (\mu_i \pm eV_i/2)]/k_BT = \alpha_\pm \tag{4.10}$$

one can use the following relation

$$\frac{e^{\alpha_\pm}}{[1+e^{\alpha_\pm}]} = \frac{1}{2} \cdot \frac{1}{1+cosh(\alpha_\pm)} \tag{4.11}$$

and thus, we rewrite the expression in 4.9 as (using the original variables):

$$\boxed{G(V_{sd}) = \frac{1}{2k_BT}\frac{1}{2}G_0 \int_{-\infty}^{\infty} dE\mathcal{T}(E)\left[\frac{1}{1+cosh([E-(\mu_s+V_{sd}/2)]/k_BT)} + \frac{1}{1+cosh([E-(\mu_d-V_{sd}/2)]/k_BT)}\right]} \tag{4.12}$$

which has singularities only at $[E - \left(\mu_{s/d} \pm V_{sd}/2\right)]/k_BT = 0$.

2. Building the system

Carbon nanotube field effect transistors (CNTFETs) were first synthetized by Sander, Alwin and Cees [31]. It consisted on a three terminal device with a source and drain metallic contacts (platinum) and a back-gate made of silicon. The metallic electrodes were connected through a single-walled carbon nanotube (SWCNT or simply CNT); it was shown the dependence of the I-V_{bias} on the gate voltage in the ohmic and non-linear regimes. The length of such devices range from 100 nm [32] to 50000 nm [33]. Since CNTs are the building block of the main system under study in the present work, an introduction to the geometry and properties of CNTs has to be provided.

Carbon nanotubes can be regarded as graphene sheets which are rolled up to form a cylinder [14]; this cylinder can be fully characterized by the so called chiral vector $\mathbf{C}_h$ which is a vector

connecting the centers of two hexagons in a graphene sheet; thus, $\mathbf{C}_h$ can be expressed in terms of the graphene latice basis vectors $\mathbf{a}_1 = \left(\frac{\sqrt{3}}{2}, \frac{1}{2}\right)a$ and $\mathbf{a}_2 = \left(\frac{\sqrt{3}}{2}, -\frac{1}{2}\right)a$:

$$\mathbf{C}_h = n\mathbf{a}_1 + m\mathbf{a}_2 \tag{4.13}$$

with $(n, m) \in \mathbb{Z}$. All the electronic and geometrical properties can be determined by the chiral vector, or in other words by the values of n and m. The diameter of the tube is given by

$$d = \frac{\|\mathbf{C}_h\|}{\pi} = \frac{a}{\pi}\sqrt{n^2 + nm + m^2} \tag{4.14}$$

with $a = \sqrt{3}a_{cc}$ being the honeycomb lattice constant and $a_{cc} = 1.42$ Å the carbon-carbon bond length. Based on the values for n and m, CNTs are classified as follows:

1. $n \neq 0$ and $m = 0$: the CNT is called *zig-zag*,
2. $n = m$: are *armchair* nanotubes,
3. $n \neq m \neq 0$ are refered as *chiral* tubes.

The original experimental set-up of the supramolecular spin-valve device used SWCNTs with a diameter of $d \sim 1.2$ nm (12 Å) and a contact spacing of ~ 300 nm (3×10^3 Å) [34]. Even thought determining experimentally the chirality of the tube is a major challenge, and for our system is experimentally unknown, there is evidence that the tubes exhibit a small band-gap at the Fermi energy; in this sense, the CNTs on the experimental realization are semi-metallic.

3. Method

In this section we present our workflow of the (C)DFT+NEGF method so that the next sections are easier for the reader to understand. The first step in the calculations consist in DFT geometry optimizations and single point simulations. The code of choice was the CP2K package [35] due to its excellent parallelization across cores and nodes which allow us to simulate relatively large systems but also periodic systems as in the case of graphene or carbon nanotubes.
The geometry optimization using DFT has to be performed for all molecules. This ensures a close-to-ground-state geometry which gives more reliable SCF convergence (and almost always faster too) in the next step. Single point calculations are then computed on an UKS level which give, to name just a few of the quantities, the electronic population, electron and spin densties, molecular orbitals, and most importantly in our case: the DFT matrices which compend the overlap matrix ($\mathbf{S}$), the spin polarized Kohn-Sham matrices ($\mathbf{H}^{\alpha}_{KS}$, $\mathbf{H}^{\beta}_{KS}$) and finally one can also print the spin polarized density matrices ($\mathbf{P}^{\alpha}$, $\mathbf{P}^{\beta}$). Depending on the system under study, one then can perform one of two extra steps which improve the quality of the results specially

for magnetic systems: the CDFT calculations and wavefunction mixing method. Both of these approaches require a well converged DFT wavefunction for a fast and reliable convergence.
Once the all the relevant matrices have been computed one way or another, they are separated into data belonging to the different regions of the FET; in terms of the previous chapters, one would have the left/right electrodes' matrices and the central region matrix (of course also the coupling matrices). Special attention has to be put here on the basis of the Hamiltonian. Since the basis sets in which the calculations are perfomed are non-orthogonal, the identity matrix now becomes

$$\mathbf{I} \rightarrow \mathbf{S} \tag{4.15}$$

thus, all diagonal matrices have to be multiplied with their correspondent overlap matrices. The surface Green's functions, which are nothing more that the GF of semi-infinite leads, for the left and right electrodes are first calculated using the decimation technique of Sancho et al. [36]. Related quantities as the self energies and broadening matrices are also calculated in this step using Eqs. 2.98 and 2.100. All these matrices are then used to obtain the central region Green's function which provides information about the DOS and transmission.
In the case of the current and differential conductance, one then has to calculate the transmission coefficient for different gate voltages. Knowing the single particle Hamiltonian, which in our case are the Kohn-Sham matrices, the gate voltage is then applied following the equation 4.1 (note that the external potential U is already taken into account by the DFT formalism) and thus we have

$$\mathbf{H}^{\sigma}_{C,KS} \rightarrow \mathbf{H}^{\sigma}_{C,KS} - \mathbf{S}_C \mathbf{V}_g. \tag{4.16}$$

The surface Green's functions of the leads are left unchanged as we assumed the gate voltage potential only affects the central region. Once all the relevant terms are calculated, one can use equations 4.8 and 4.12 to obtain the current and differential conductance respectively.
It is worth mention that the calculations of the NEGF part, was performed entirely with an in-house implementation of the theory.

4. Basis set dependence

Modelling correctly the atomic wave function (AO) is a big challenge due to the increasing number of electrons and orbitals as the atoms get filled with orbital shells. The task gets even more complicated when not only isolated atoms are to be described but rather molecules. An accurate but also a computationally achievable wavefunction is one of the ultimate goals in

quantum chemistry software development. In the following section we present a detailed study of the basis sets and their influence on our systems which will serve as a building block for more complicated complexes.

4.1. Basis sets

Let us consider an $1s$ orbital to explain the concept of a basis set in quantum chemistry softwares. Two types of basis functions have proved to work correctly in many cases:

- The *Slater type* function: $\phi_{1s}^{SF}(\zeta, \mathbf{r} - \mathbf{R}_A) = \left(\zeta^3/\pi\right)^{1/2} e^{-\zeta|\mathbf{r}-\mathbf{R}_A|}$
- The *Gaussian type* function: $\phi_{1s}^{GF}(\alpha, \mathbf{r} - \mathbf{R}_A) = (2\alpha/\pi)^{3/4} e^{-\alpha|\mathbf{r}-\mathbf{R}_A|^2}$ where α is the *Gaussian orbital exponent.*

The orbital exponents (positive numbers), determine the diffuseness or size of the basis functions; a *large* exponent implies a small dense function meanwhile a *small* exponent implies a large diffuse function.
The major differences between the the two types of sets is given at $r = 0$ and $r \to \infty$; at $r = 0$, the Slater function has a finite slope while the Gaussian function has a zero slope

$$\left[\frac{d}{dr}\left(e^{-\zeta r}\right)\right]_{r=0} \neq 0$$
$$\left[\frac{d}{dr}\left(e^{-\alpha r^2}\right)\right]_{r=0} = 0.$$

For large values of r, the Gaussian basis functions also decay more rapidly than the Slater type of orbitals.
An example of how the different parameters affect the basis sets is depicted in figure 4.2.
It can be shown that the molecular orbitals at large distances decay as $\phi_i \sim e^{-a_i r}$, which is better described by the Slater's type of functions. Nevertheless, Gaussian functions are more widely used, the reason being that in a SCF calculation, one must calculate of the order of $K^4/8$ two electron integrals which have the form:

$$\langle \mu_A \nu_B | \lambda_C \sigma_D \rangle = \int d\mathbf{r}_1 d\mathbf{r}_2 \phi_\mu^{A*}(\mathbf{r}_1) \phi_\nu^{B*}(\mathbf{r}_1) r_{12}^{-1} \phi_\lambda^{C*}(\mathbf{r}_2) \phi_\lambda^{D*}(\mathbf{r}_2) \tag{4.17}$$

where ϕ_μ^X is a basis function on nucleus X, i.e., centered at $\mathbf{R}_X$ with $X = A/B$; therefore, the integral involves a product of four-center functions that is very difficult with a Slater-type basis. Gaussian functions on the other hand, can be convoluted which means that the sum and product

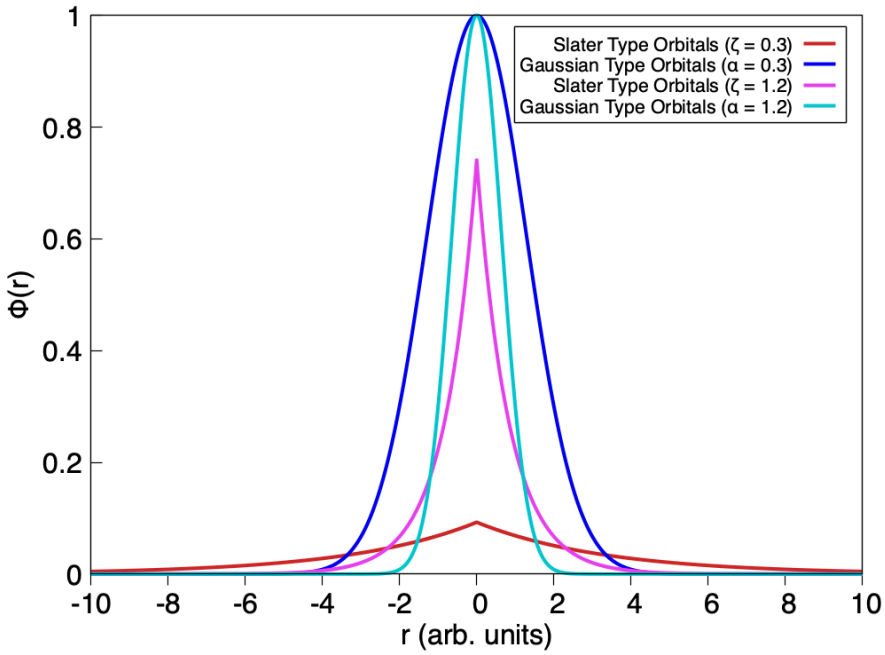

Figure 4.2.: Comparison between Slater and Gaussian basis sets. Both functions are centered around $R_A = 0$. The negative values of r are just for illustration purposes, they have no physical meaning.

of two Gaussian functions is again a Gaussian [37]; this analytical property allows a faster and cheaper computational treatment of atomic functions.

A well known problem with Gaussian-type orbitals (GTOs) is that they have functional behaviour different from that of molecular orbitals. To solve this problem one usually defines a basis as linear combinations of primitive Gaussian functions ϕ_p^{GF}. These linear combinations are called *contractions* and thus the basis functions used on several quantum packages are called *contracted Gaussian functions* (CGF),

$$\phi_\mu^{CGF}(\mathbf{r} - \mathbf{R}_A) = \sum_{p=1}^{L} d_{p\mu}\phi_p^{GTO}(\alpha_{p\mu}, \mathbf{r} - \mathbf{R}_A) \tag{4.18}$$

where L is the length of the contraction and $d_{p\mu}$ is the contraction coefficient. Since the Gaussian type of orbitals differ from the real Slater type, one usually uses more than one CGF to describe an orbital of an atom. The number of basis functions used to describe an AO give the quality of a basis set; in this sense, if an AO consist of one GTO then the basis set is said to have a **single-zeta** quality. With two GTO's per AO we then have a **double-zeta** basis set and so on.

4.2. Long vs short range MOLOPT-basis sets

From basic quantum mechanics we know that an atomic wave function with principal, angular and magnetic quantum numbers i, l_i and m_i respectively, has the form:

$$\phi_i(\mathbf{r}) = R_i(r) \cdot Y_{l_i,m_i}(\theta, \phi) \tag{4.19}$$

where $R_i(r)$ denotes the radial part and $Y_{lm}(\theta, \phi)$ are spherical harmonics for the angular part. The radial part is the function that can be described as a sum of CGFs of the form

$$R_i(r) = r^{l_i} \sum_{j=1}^{N} c_{ij} \cdot e^{\left(-\alpha_j \cdot r^2\right)}. \tag{4.20}$$

Let us consider two types of CGFs as defined on the quantum software CP2K, they are called short ranged and long ranged basis sets; the term short/long refers to the diffuseness of the CGF's; a larger number of CGFs used for the AO's in Eq. (4.18) produces a longe range basis (thus more diffuse) while a smaller number of CGFs produces a short range basis (less diffuse). We take as an example the hydrogen atom. The following set is defined in the so called Single-Zeta-Valence (SZV) molecular optimized basis (MOLOPT) or *SZV-MOLOPT-GTH* for short:

```
1  H  SZV-MOLOPT-GTH SZV-MOLOPT-GTH-q1
2  1
3  2 0 0 7 1
4      11.478000339908   0.024916243200
5       3.700758562763   0.079825490000
6       1.446884268432   0.128862675300
7       0.716814589696   0.379448894600
8       0.247918564176   0.324552432600
9       0.066918004004   0.037148121400
10      0.021708243634  -0.001125195500
```

And for the short ranged

```
1  H  SZV-MOLOPT-SR-GTH SZV-MOLOPT-SR-GTH-q1
2  1
3  2 0 0 5 1
4      10.068468228533  -0.033917444900
5       2.680222868089  -0.122202212100
6       0.791501539122  -0.443818861200
7       0.239116150487  -0.453182186600
8       0.082193184441  -0.131612861500
```

The several numbers appearing on the basis sets contain information about the quantum numbers of the atom as well as the different parameters of the CGFs:

1. The units of the exponents are in $Bohr^{-2}$.

2. The first number in line number 3 stands for the principal quantum number, in this case 2.

3. The second number in line 3 is the minimum value of the angular quantum number l in this set: $l = 0 = s_{orbital}$.

4. The third number stands for the maximum value of the angular quantum number. In this case $l = 0 = s_{orbital}$.

5. The fourth number corresponds to the number of exponents in (4.20).

6. The fifth value is how many sets of contraction values (c_{ij} in (4.20)) this set has for the $s_{orbitals}$.

7. If there would be more numbers, they would account for the number of contraction coefficients for the next angular momentum value: $l = \{1, 2, 3, \ldots\} = \{p, d, f, \ldots\}$ orbitals.

We then write explicitly the Gaussian function defined by the two sets:

$$\begin{aligned}\rho_{LR,1}(\mathbf{r}) = Y_{0,0}\Big[&0.0249e^{-11.478} + 0.0798e^{-3.7007} + 0.1288e^{-1.4468} + 0.37944e^{-0.7168} \\ &+ 0.3245e^{-0.2479} + 0.0371e^{-0.0669} - 0.0011e^{-0.0217}\Big]\end{aligned} \tag{4.21}$$

and for the short ranged

$$\begin{aligned}\rho_{SR,1}(\mathbf{r}) = Y_{0,0}\Big[&- 0.0339e^{-10.0684} - 0.1222e^{-2.6802} - 0.4438e^{-0.7915} - 0.4531e^{-0.2391} \\ &- 0.1316e^{-0.0821}\Big]\end{aligned} \tag{4.22}$$

We can now plot the radial part of the basis set (which are multiplied times a constant factor in the angular coordinates) for both sets to compare them. Figure 4.3 shows both 2s orbitals for the hydrogen atom using the basis sets in 4.21 and 4.22 (not normalized).

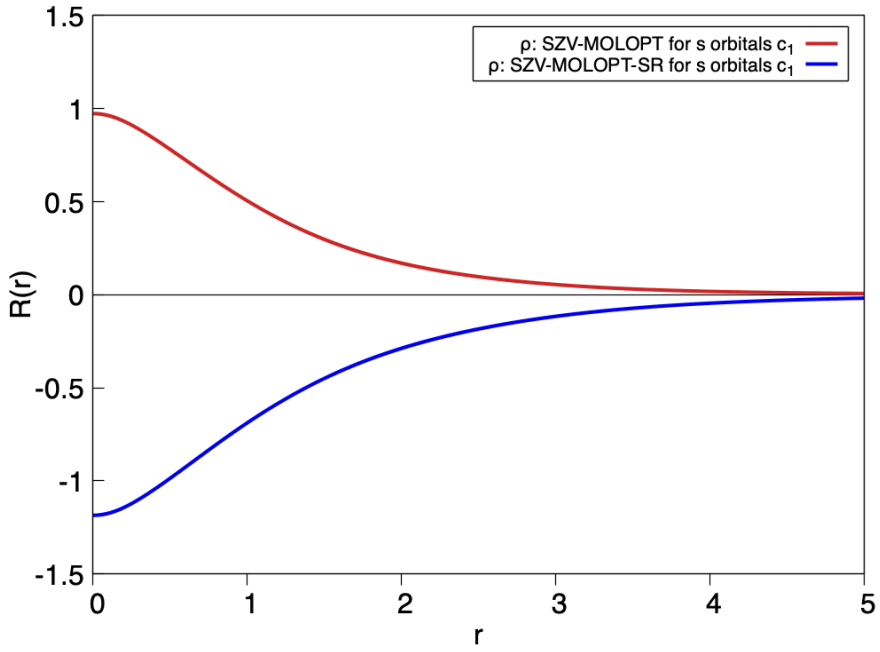

Figure 4.3.: 2s radial wave function for an hydrogen atom as it is defined in CP2K documentation.

One can observe that the resulting Gaussian function depicts almost the same behaviour for both sets but in the case of the short ranged, there are two less contraction coefficients which for large sized systems reduces the computational time and resources without any loss of physical information of the system.
A less trivial example is the case of carbon atom basis functions. Figure 4.4 depicts a comparison for short and long range basis (normalized) but in a higher quality basis set: *DZVP-MOLOPT* and *DZVP-MOLOPT-SR*.

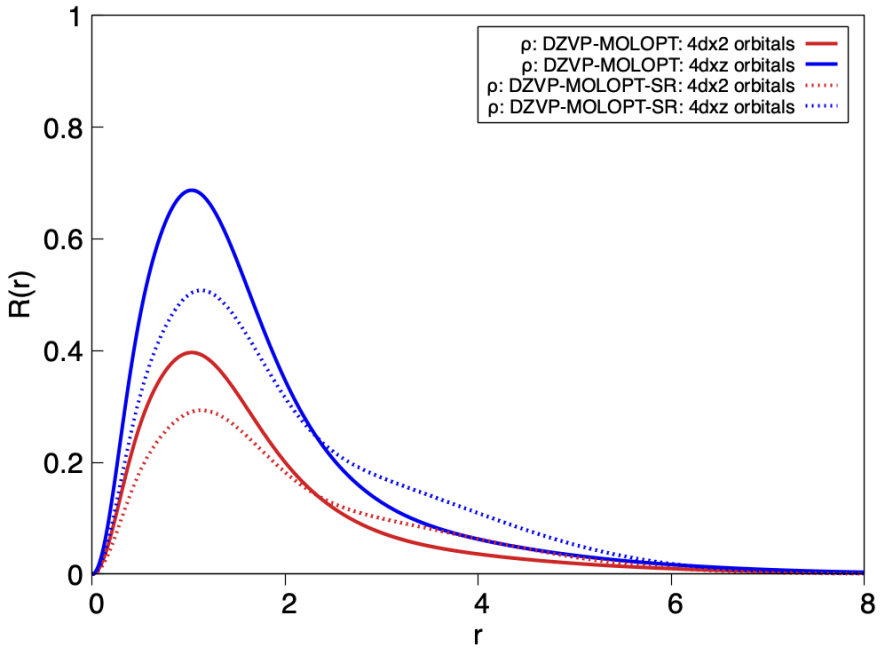

Figure 4.4.: d orbitals for carbon in a DZVP quality basis set. As in the case of hydrogen 2s orbitasl, the differences occur mostly at the peak of the Gaussian shape. As we shall see in later sections, this has an impact on the density of states of our systems.

4.3. Effect of the basis sets on the density of states: carbon nanotubes.

Now we have all the ingredients to perform DFT+NEGF calculations. As it has been pointed out several times, the two main quantities to study are the density of states and the transmission coefficient. Here we present the simulations of different types of carbon nanotubes with several chiralities which will give a better insight of the simulations of more complicated systems.

Due to the number of atoms that an armchair CNT contains per unit cell, the computation of large systems using such types of chiralities is not very efficient. On the other hand, zig-zag CNTs contain, per supercell, $4 \cdot n$ atoms, where n is the first chiral number. This makes the simulation by means of DFT more tractable and thus, we use those CNTs for the theoretical simulations.

Figure 4.5 shows the evolution of the density of states of carbon nanotubes with different diameters as the size of the basis functions increases. The unrestricted DFT calculations were performed using PBE functional with GTH effective potential for the core electrons. The simulation box size was set to $[25.00 \times 12.78 \times 25.00]$Å with the axis tube along the y-direction. As for the NEGF calculations, one per spin channel was always carried, this means that for each of the Kohn-Sham matrices obtained by UKS a set of DOS/T was calculated. All the figures show the sum of the states/channels for the alpha and beta spins.

(n,m)	Diameter (Å)	Atoms per supercell	DFT+NEGF Δ_g (eV)
(9,0)	7.0459	36	0.14
(10,0)	7.8288	40	0.91
(12,0)	9.3946	48	0.12
(13,0)	10.1775	52	0.71

Table 4.1.: Different CNTs studied in this work and their simulated bandgaps (Δ_g). The number of CNT supercells for each of the regions of the CNTFET was 1, thus the system consisted on 3 periods of the corresponding CNT. All the values in our work were taken with the short ranged basis set.

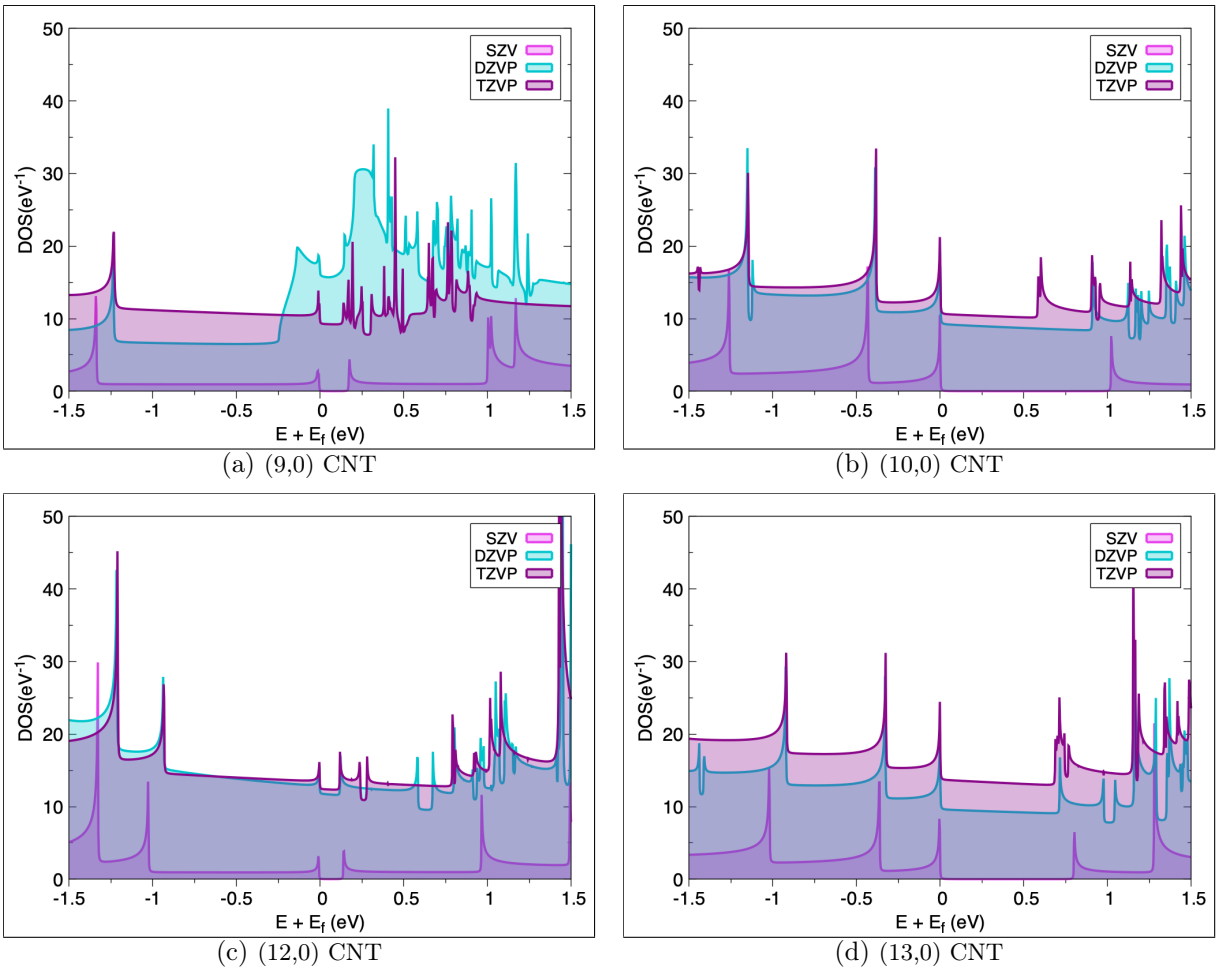

(a) (9,0) CNT (b) (10,0) CNT

(c) (12,0) CNT (d) (13,0) CNT

Figure 4.5.: Density of states of different chiralities CNT's. It is easily observed that as the size of the basis increases, spurious states appear on the band gap region of the tubes, and in some cases, even the region of valence electrons is completely altered (see e.g. (a))

Figure 4.6 presents the same systems as in Fig. (4.5) but simulated using short range basis sets. Such pictures exemplify the improvement on the spectra of the CNT's using the SR basis set. The extra energy levels on the DOS spectra appearing across the whole energy range are swiped out using the short ranged basis. To illustrate the full method of DFT+NEGF, figure 4.7 finally

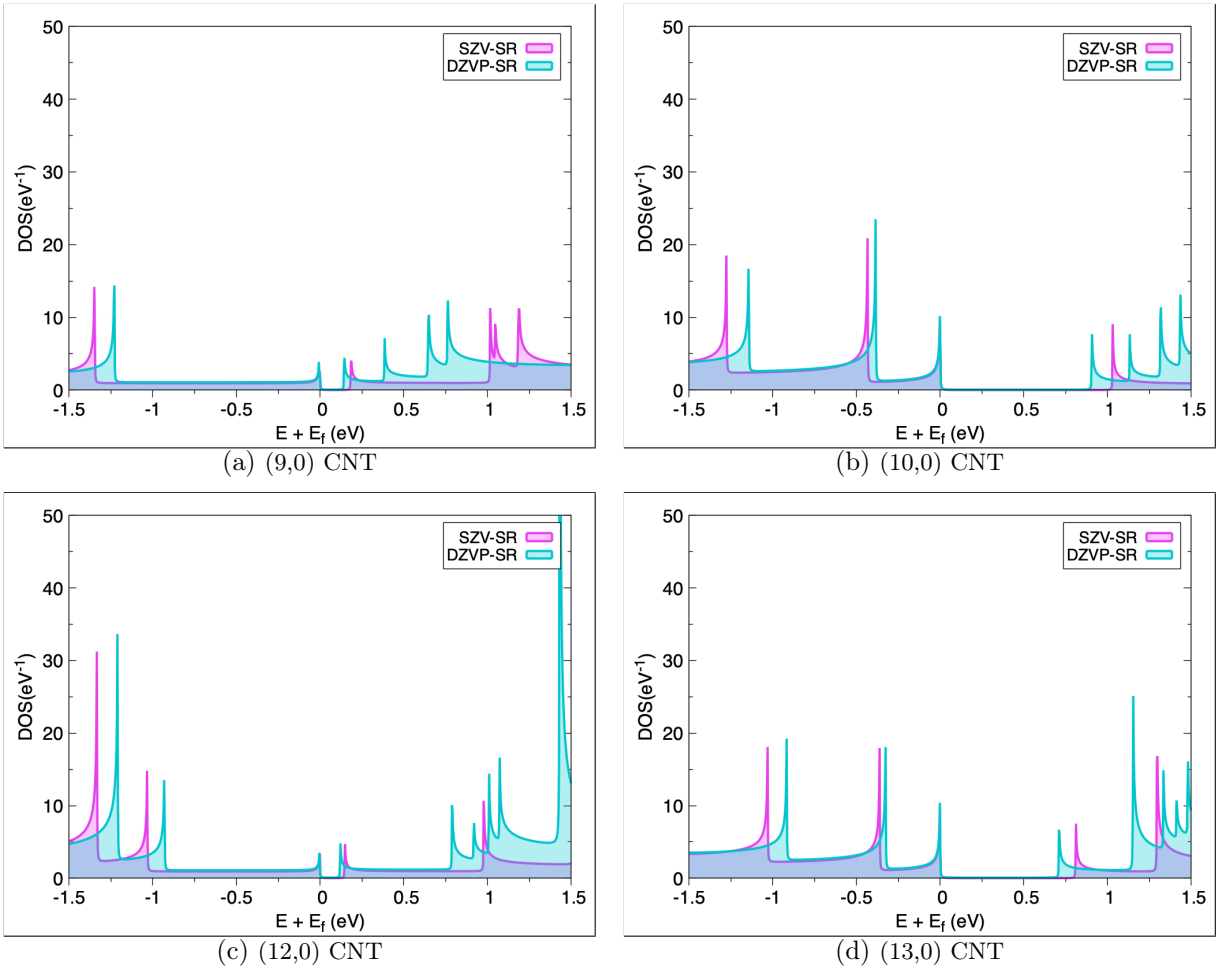

(a) (9,0) CNT (b) (10,0) CNT

(c) (12,0) CNT (d) (13,0) CNT

Figure 4.6.: Density of states for the same systems in 4.5 but simulated with the short range basis sets. It is quite clear how the density gets corrected across the whole energy region. A short ranged TZVP basis set was not available at the moment of the test.

depicts the transmission coefficient for all systems. From figures 4.5 and 4.6 not only the spurious density of states on the CNT spectra dissapears, but the electronic bandgap gets reduced for all our models.

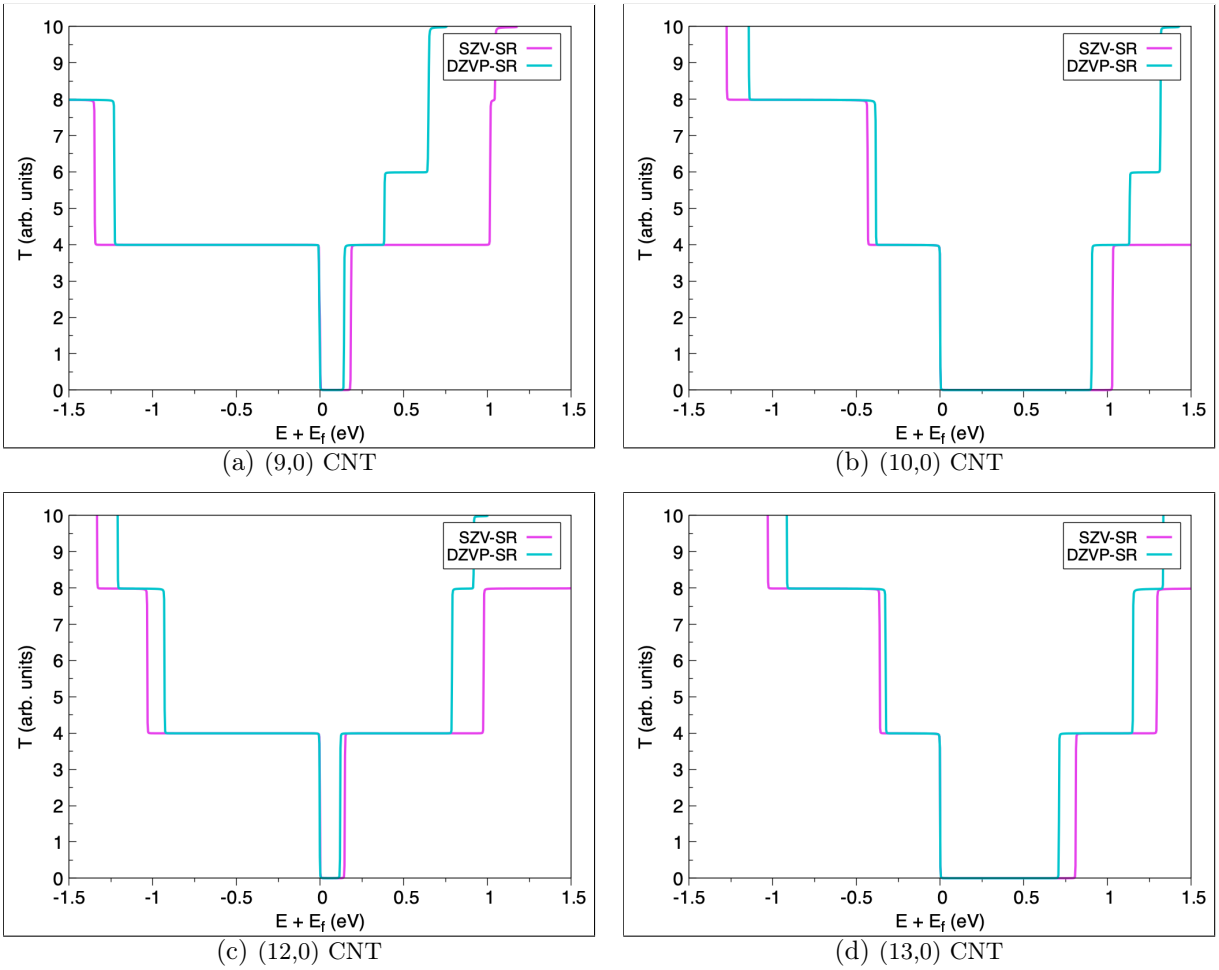

(a) (9,0) CNT (b) (10,0) CNT

(c) (12,0) CNT (d) (13,0) CNT

Figure 4.7.: Transmission coefficient of the systems in table 4.1.

This concludes the first part of the results that contain the simulation of bare CNTs using DFT. Now we present the results for the modelling of single molecule magnets at the DFT level.

5. First principles modelling of lanthanide based single molecular magnets

This section is dedicated to the study / simulation of the $LnPc_2$ systems. As an introduction we start with relatively simpler systems in which the lanthanide atom has been replaced with a closed shell transition metal, namely yttrium. Appart from being a 'lighter' system (to simulate) it provides useful insights on the spin distribution in such molecules.

5.1. Molecular Magnetism

As molecular magnetism we understand the field which studies the synthesis, characterisation and modelling of systems composed of one or more magnetic molecules. The molecules can be found in several forms ranging from uni-centered molecules, chains of magnetic molecules or crystallized

single-molecule magnets [38, 39, 40, 41]. In this work we focus on the type of molecular systems called single-molecule magnets (SMMs). Geometrically, SMMs are characterized for having at least a metal ion center which in turn is usually sandwiched between ligands which shield the metallic center(s) from the outside [42]. They usually possess high values for the spin moment arising from their metal centers [42] and exhibit interesting phenomena like quantum tunneling of the magnetization, slow magnetic relaxation times and a stepwise hysteresis loops [43, 44, 45, 46]. They possess a so called 'easy axis' which is nothing more than the prefered direction of the molecules' magnetic moment [45].

Some of the potential applications to SMMs are for example, molecule spintronics [47], magnetic high-density storage devices [48] or potential building blocks for quantum computers [49, 50].

A SMM is usually characterized by three parameters: the magnetic blocking temperature (T_B), the coercive magnetic field (H_C) and the effective energy barrier U_{eff}. To understand these three parameters, let us consider an imaginary sample containing SMMs which have a total spin of $S = 5$ arising from a random metal center. An axial zero-field splitting (ZFS) (which is the consequence of having more than one unpaired electron), will split the state into $2S + 1$ levels (with quantum numbers m_s) ranging from $-S$ to S in integer steps with a Hamiltonian given by

$$H = D\left[S_z^2 - \frac{1}{3}S(S+1)\right]. \tag{4.23}$$

where D is a constant called zero-field splitting parameter which can take positive of negative values. (In general, D is a symmetric traceless tensor, but in this particular case, we assume that D and g (the g-factor) are isotropic and thus, have the same principal axis. For a better description check [51]).

The energy levels can be depicted as in figure 4.8 in the case of $D < 0$, from where one can see that the degenerate spin states are separated by an energy barrier U_{eff}.

In order to go from one spin state to the other, one can refer to three mechanisms. The first is due to the thermal energy. If the termal energy is larger than the energy barrier U_{eff} then the system will oscillate between both spin orientations. If the temperature gets lowered, the system will 'freeze' into a spin state, thus lowering the probability of spin flip. At low temperatures though, one could apply an external magnetic field H to the sample causing the orientation of the spin to be along H; the magnetization $M(t)$ will reach a saturation value and will stay that way as far as the magnetic field is on. Once H is switched off, the magnetization of the system will relax to thermal equilibrium which can be expressed as [45, 46] (figure 4.8)

$$M(t) = M(t_0)exp(-t/\tau) \tag{4.24}$$

where t_0 is the time at which the magnetization was maximum and τ is the relaxation time. This process will define a hysteresis type of plot which will give insights into the system. In this

sense, the magnetic blocking temperature T_B, is defined as the highest temperature at which an SMM displays hysteresis in its magnetization plots [52]. The coercive magnetic field H_c is the magnetic field needed to bring the SMMs' magnetization to zero.

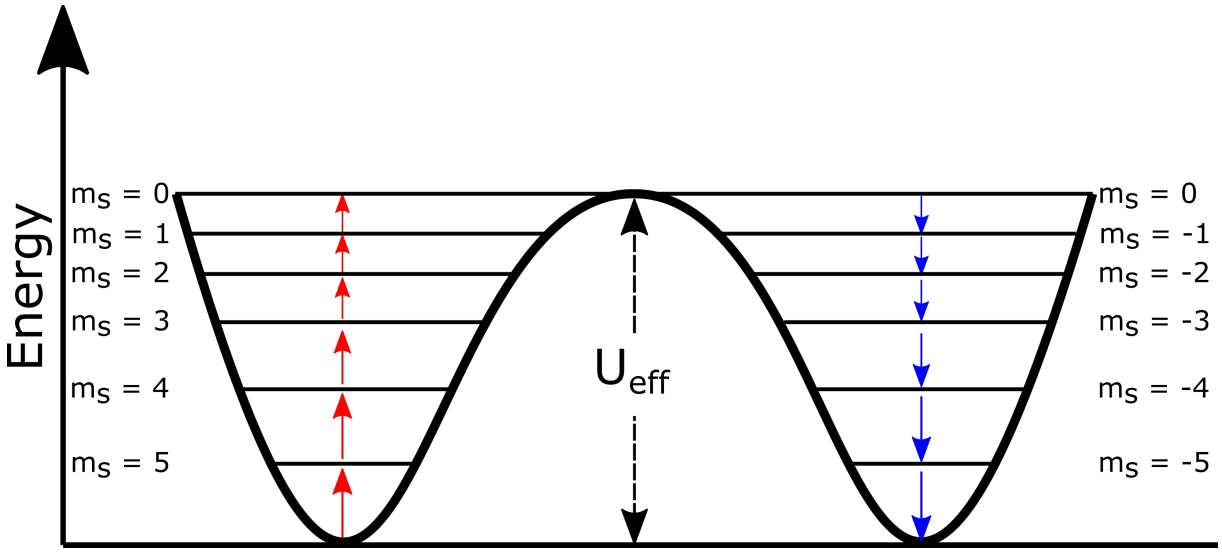

Figure 4.8.: Pictorical representation of an SMM energy multiplets. The number of energy levels is given by $2S + 1$. In the abscence of a magnetic field, $+m_s$ and $-m_s$ states are degenerate.

The last mechanism to effectively change the spin of our fictitious system is known as the Quantum Tunneling of the Magnetization (QTM) which was discovered by Chudnovsky and Gunther in 1988 [53]. This phenomena happens at low temperature, and it is the quantum mechanical tunneling of the magnetization of a molecule. This means, that a spin up state would overcome the barrier U_{eff} with a tunnel effect to become a spin down state.
The problem characterizing a molecule with T_B or H_c is that they depend on the measuring technique and/or the temperature [49]. Thus, the most widely used characterization parameter is the effective energy barrier U_{eff}.
Therefore, one can say that, regardless of the SMM type, two parameters have to be adjusted so that the magnet is regarded as a good candidate for practical purposes: the blocking temperature and the effective potential barrier. The barrier has to be large enough so that the SMM can retain information for longer periods of time without spin relaxation (almost none QTM) and the blocking temperature has to be raised so that the SMM can be used in practical systems.

5.2. Lanthanide based single molecular magnets

SMMs are usually synthetized using transition-metal ions, nonentheless, it can also be replaced by lanthanide ions as shown by Ishikawa et al. [42]. In the present work, a special kind of lanthanide-based SMMs is examined, namely LnX SMMs; they consist on a lanthanide (Ln) center sandwiched between two ligands (X) which can be for instance phthalocyanines (Pc) or

phorphorines (Pho) rings [54]. The first type of them, $LnPc_2$, has been studied extensively [55, 56, 57]. They present a large magnetic anisotropy which is given by the ligand field where the lanthanide atom is placed [58] in contrast to the regular 3d metal-cluster SMMs where the anisotropy is a consequence of magnetic interactions between 3d metal ions [58, 59]. The three most common ionic states $[LnPc_2]^X$ with $X = -1, 0, +1$ have been synthesized and their electronic as well as their magnetic properties have been studied by several groups [57, 58, 60]. Theoretically, the electronic structure of such systems has been treated by Rousseau et al. [61] using a extended Hückel Hamiltonian. The geometry of such molecules can be characterized by several parameters which include the distance between the plane defined by the pyrrole nitrogens on the ligands (in the case of phthalocyanines), the relative angle between the Pc's and the distortion of the ligands from planarity. An oxidation process can undergo in the ligands causing the neutral state of $[LnPc_2]^{-1}$; this leaves a system with an unpaired electron delocalized on the ligands which then contributes with and spin $\frac{1}{2}$ to the whole system.
There are several reasons why lanthanide based SMMs are so attractive for further development: first, the magnetic relaxation occurs at larger temperatures with respect to the usual 3d metal complexes SMMs; second, in contrast to the 3d SMMs where the magnetic properties are due to the several metal ions, the single ion lanthanide based SMMs display their magnetic properties due to maximum two magnetic molecules (the lanthanide ion itself and the ligands which can present an unpaired electron). Finally, they present high energy barriers U_{eff} (some Dy(III) molecular magnets have shown an astonishing effective barrier of 1000 K [62]) which as we have seen, it is fundamental to have stable magnets at higher temperatures. Even though these characteristics are the most relevant to date, there is still a lot to discover in the upcoming years to make the Ln-based SMMs truly useful for practical purposes.

5.3. Yttrium Phthalocyanine

The electronic structure of yttrium reads $[Kr]4d^15s^2$. The diamagnetic oxidation state of yttrium (Y^{3+}) lacks of localized f-electrons; thus, the magnetic properties of the molecule $[Y^{3+}Pc_2]^0$ (YPc_2 from now on) are exclusively due to the ligands. Appart from existing in gas phase, YPc_2 crystallizes in different forms, for example in the space group $P2_12_12_1$ also called $\gamma-$phase [63] which has four YPc_2 molecules per unit cell or in a solvated form $[YPc_2]\cdot CH_2Cl_2$ [64].
Let us start with the most simple form, namely the gas phase. Geometry optimizations were performed for all molecules followed by single point calculations to obtain the electronic as well as the spin properties of each of the compounds. The level of DFT theory used for the yttrium systems was unrestricted DFT. Figure 4.9 presents the spin density ($\rho_\alpha - \rho_\beta$) of YPc_2. As it can be appreciated, the extra electron is completely delocalized in the tetrapyrrole inner carbon atoms of the ligands. This feature can be also visualized by plotting the density of states displayed in

panel b) of the same figure which shows the unpaired (spin-up) electron on the highest occupied molecular orbital energy level.

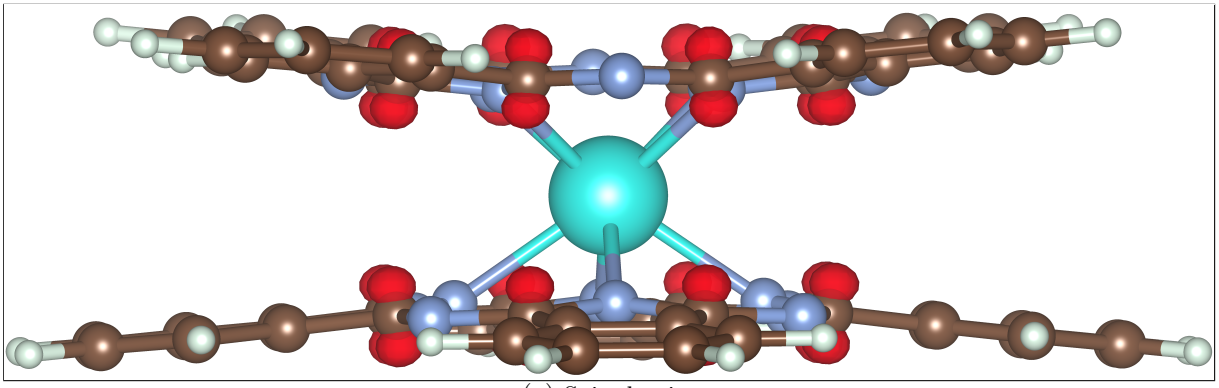

(a) Spin density

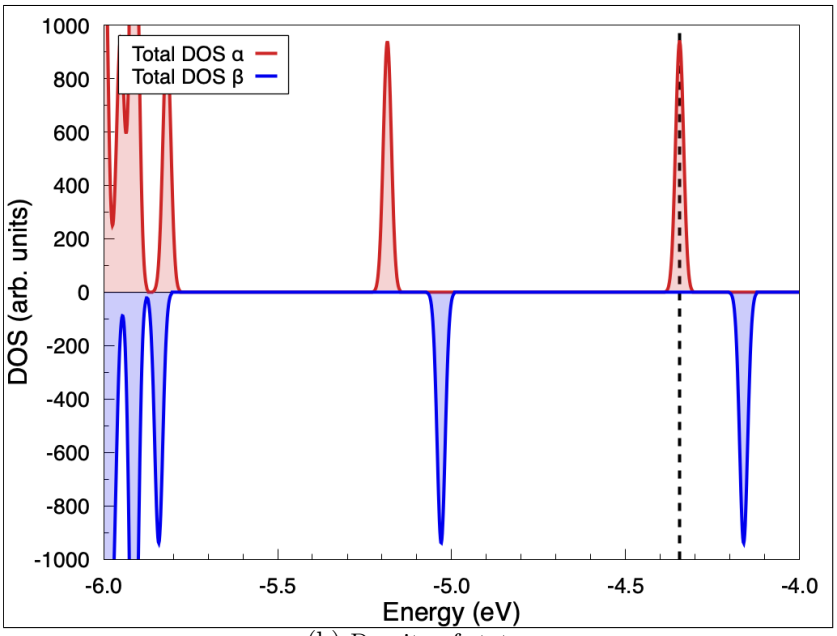

(b) Density of states

Figure 4.9.: YPc_2 UKS simulation. The inner carbon atoms in both ligands contain the extra electron (red lobes) which corresponds to the HOMO level on panel b) marked with a black dashed line.

In a lattice, the extra electron remains still on the ligands but, depending on the stacking type as well as if the sample presents defects (i.e. not a perfect lattice), its orientation with respect to each other, varies. This means that, for instance, in the solvated compound $[YPc_2]\cdot CH_2Cl_2$, the interactions between the stacked chain of molecules, present ferromagnetic interactions contrary to the unsolvated $\gamma-$phase whose interactions are antiferromagnetic [65]. DFT calculations can predict the ground state of each of the compounds with relatively good accuracy. As an example, let us take the crystal structure shown in figure 4.10. They show two types of periodic simulations: the first one (panel a and c) represent periodic simulations (in spatial directions) where a perfect lattice is assumed. The simulation box (black boxes around the molecules in panels c and d)

was repeated on the $x-, y-, z-$ directions without any empty space between images. Contrary to the 'gas' phase (or a lattice with defects) where empty space is left between images (panel d). Panels a and b show the relative energies between DFT ground state simulations with different multiplicities (i.e. different alignement of the unpaired spins of the $[YPc_2]\cdot CH_2Cl_2$ molecules).

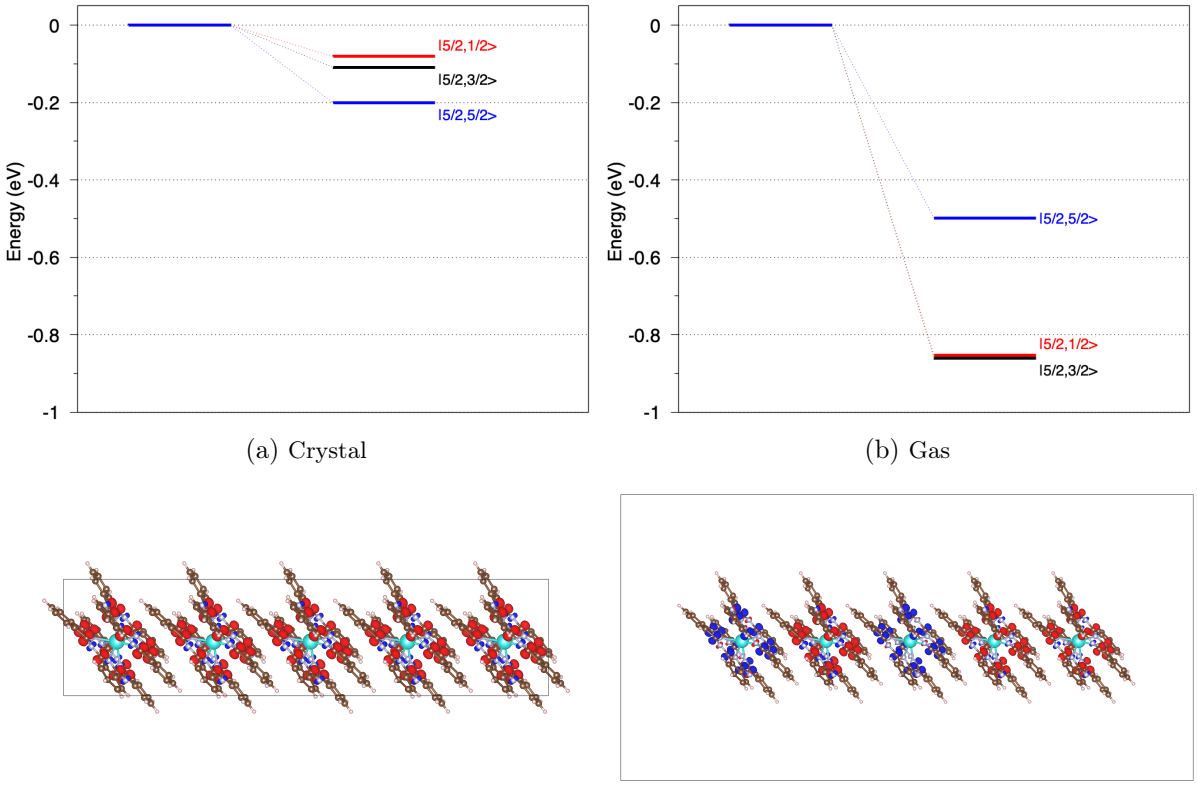

(a) Crystal

(b) Gas

(c) Crystal. $m_s = 6$.

(d) Gas. $m_s = 2$.

Figure 4.10.: DFT ground state energies of the $[YPc_2]\cdot CH_2Cl_2$ crystal structures for different multiplicities as well as the spin density of the lowest energy states. In the case of the 'gas' phase, the spin density shows the multiplet $m_s = 2$ and not the $m_s = 4$ since the former shows a very well spin localization. In any case, in the gas phase, both multiplicities DFT energies are very close to each other.

Thus, regardless of the multiplicity, periodicty or stacking, the ligans' spins retain their spatial position in the molecule. This supports the observations and settings of the following simulations of the gas phase molecules as well as the compound systems of carbon nanotubes plus single molecule magnets.

5.4. Terbium bi-phthalocyanine

The novel bi-radical system $[Tb^{3+}Pc_2]^0$ (or simply: $TbPc_2$, from now on) has been intensively studied over almost two decades [42] and consists of a terbium center in its ionization state 3+ (electronic configuration $[Xe]4f^8$) and Pc-rings conforming the chemical structure: $(C_8H_4N_2)_4$.

Since Tb^{3+} is an open shell system, it possess contributions to the total electronic angular momentum (J) from the orbital angular momentum (L) and the spin angular momentum (S). To get the total angular momentum we simply apply Hund's rules to the $4f^8$ system. The angular momentum takes values from $l = 0 \cdots n - 1 = 3$ (s, p, d, f), thus the electrons are organized as follows:

- The term with **maximum multiplicity** has lower energy. In this case the maximum multiplicity with 8 electrons in 7 energy levels (f orbitals) is 6 (multiplicity: $2S + 1$).
- For a given multiplicity, the level with **maximum orbital angular momentum** is lower in energy. In our case: $L = 3$. This can also be obtained by the following formula:

$$\mathbf{L} = \sum_{i=-3,\ldots,3} l_i = 3 + 3 + 2 + 1 + 0 - 1 - 2 - 3 = 3 \tag{4.25}$$

  where l_i runs over the occupied orbitals.
- Finally, our system has more than half of the shell filled, therefore the highest value of the total angular momentum is given by the relation $J = |L + S|$ and therefore in our system, $J = 6$.

Due to the ligand's field of the Pc's, the second energy state $|m_J = \pm 5\rangle$ is well separated from the degenerate ground state $|m_J = \pm 6\rangle$. This separation has a value of 400 cm^{-1} or 0.04959368 eV [55].
Electronic paramagnetic resonance (EPR) measurements at zero magnetic field have shown that the unpaired electron of the ligands and the ground state $|m_J = \pm 6\rangle$ of the terbium atom are coupled and this interaction is a ferromagnetic type [66], i.e., the spin ground state of the molecule reads $|m_J = 6, m_S = \pm 1/2\rangle$.
We now present our DFT calculations on the $TbPc_2$, which help us to corroborate (at least qualitatively) the experimental as well as some previous knowledge of this particular SMM. The geometries were optimized using the parameters on table 4.2.

[2]Basis set for atoms H, C, N contained a Polarization function. Tb atom did not. For Terbium a double set quality was the only available for the pseudopotential used [67].

CP2K parameter	Value(s)
MAX_DR	1.0^{-3}
MAX_FORCE	1.0^{-3}
RMS_DR	1.0^{-3}
RMS_FORCE	1.0^{-3}
OPTIMIZER	BFGS
Basis set quality	T(D)ZV(P) [2]
CHARGE	0
MULTIPLICITY	8
MINIMIZER	DIIS
PRECONDITIONER	FULL_ALL
ENERGY_GAP	0.1
XC_FUNCTIONAL	TPSS
VDW_POTENTIAL	DFTD3
Cell Dimensions	$[40.0, 20.0, 40.0]$

Table 4.2.: DFT parameters used for relaxing the molecule $TbPc_2$.

The relaxed molecule (Fig. (4.11)) presents some relevant interatomic distances also found by other works [61] like the deviation of the ligands from planarity, coordination number of 4 as well as the C-N distances within the ligands' rings. We depict all the relevant interatomic distances on figure 4.11.

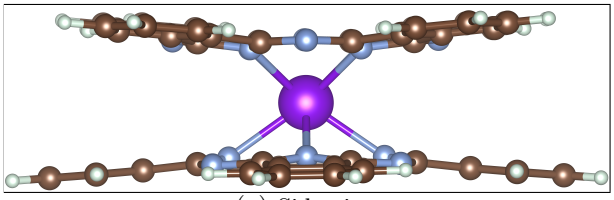

(a) Side view

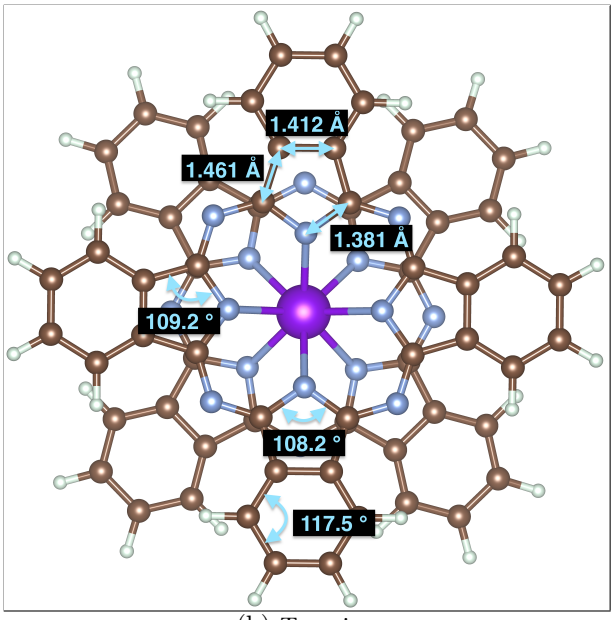

(b) Top view

Figure 4.11.: DFT optimized $TbPc_2$ molecule. Brown, blue, white and purple correspond to carbon, nitrogen, hydrogen and terbium atoms respectively. In b some of the bond distances are marked as well as the angle between carbon nitrogen carbon of the ligands' rings.

Our main interest are of course, the electronic properties of the simulated molecules; for this purpose, we carried on different procedures to study the distribution of the energy levels, the electron and spin densities and charge analysis. In order to justify the usage of a non-standard method like CDFT, we depict a direct comparison of UKS and CDFT results and provide an explanation of each of the figures / tables. The basis set used in our simulations were the MOLOPT-UCL for the N, C and H atoms, while for the Tb atom the basis set MOLOPT-LnPP1 [67]. In terms of the pseudopotential used to take into account the core electrons of each of the atoms, we used the GTH pseudopotential for the organic atoms and the LnPP1 pseudopotential for the metal center.

For the case of the CDFT calculations, we applied 3 different constraints:

1. A charge constraint to the terbium atom. The value of the constraint was set to 26 so that it would give a net charge of +3 (The charge in CDFT in the CP2K package is obtained by substracting the constraint value to the number of electrons of the pseudopotential. In

our case, the LnPP1 pseudopotential has 29 core electrons, thus the charge of the system is $29 - 26 = +3$).

2. A magnetization constraint to the terbium atom, so that the electronic configuration consists of 6 unpaired up electrons. Hence, the value of this constraint was set to 6.

3. A magnetization constraint to both of the ligands to assure that there was no charge transfer from the ligands to the metal center.

The results of the constraints after the SCF convergence are displayed in table 4.3.

	Tb	**C-atoms**
Charge	26.012/26	–
Magnetization	6.095/6	1.047/1

Table 4.3.: Final values of the constraints applied to $TbPc_2$. As can be seen, in terms of charge and magnetization, the molecule is quite close to the expected values: the terbium atom having six alpha spin electrons and an extra delocalized alpha electron on the ligands. The target values are also written. In the carbon atoms, only a magnetization constraint was applied.

Figure 4.11 shows a comparison of the spin density of $TbPc_2$ with the two different approaches: UKS and CDFT. The difference is quite obvious in the sense of how the spin density is well localized on the inner carbon atoms of the ligands in the case of the CDFT simulation. This is in accordance with the results in [68] where the gas phase of the $TbPc_2$ molecule was also calculated.

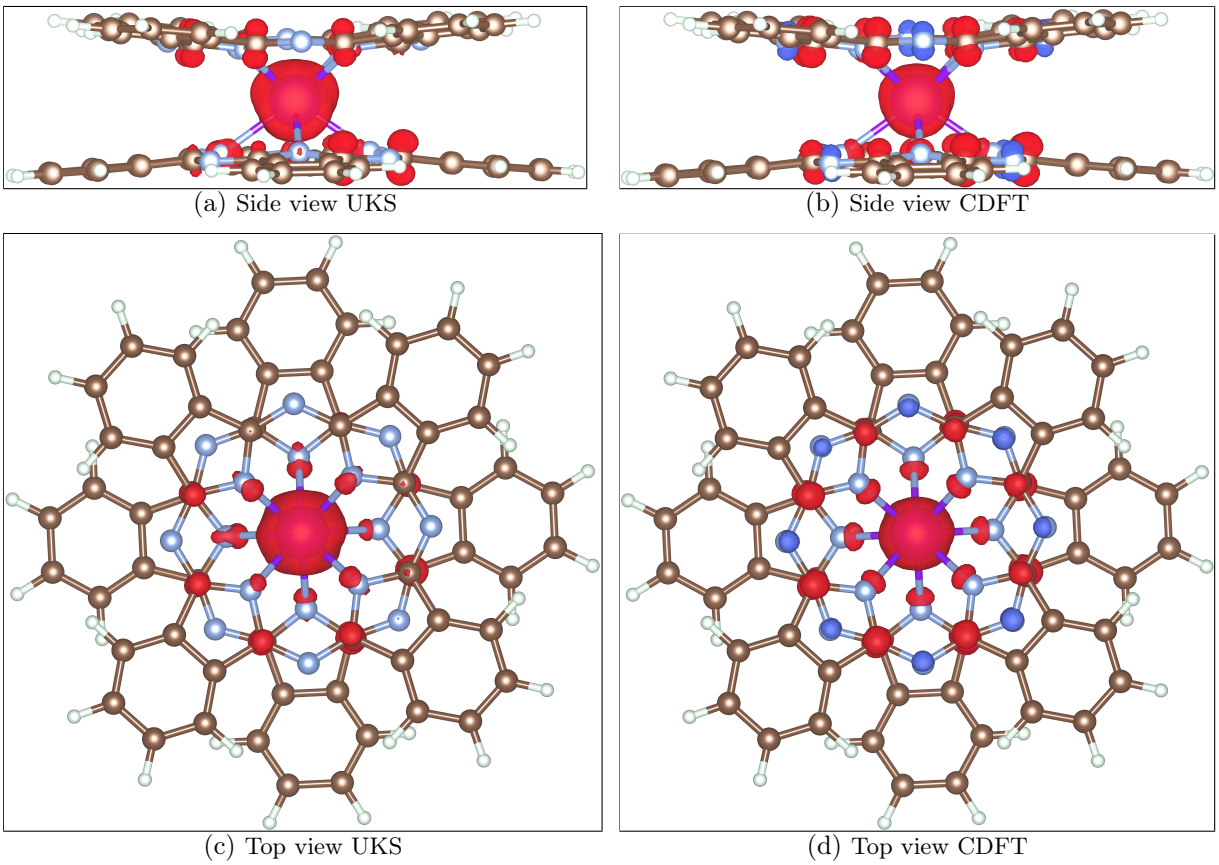

(a) Side view UKS (b) Side view CDFT

(c) Top view UKS (d) Top view CDFT

Figure 4.12.: Comparison between the spin density of $TbPc_2$ for the UKS and CDFT simulations. Red/blue colors represent alpha/beta spin density respectively. In the case of the UKS simulation, some of the alpha spin density in the ligans has been transfered to the terbium atom which is undersirable for our main system where not only the SMM are to be simulated, but a substrate to which electron leaking can occur. This behaviour is corrected using CDFT.

In terms of the energy levels, both type of simulations are similar. In figure 4.3 the HOMO levels per spin are shown. One can see how the alpha levels are lowered in the CDFT simulation compared to the UKS, while the HOMO and HOMO+1 are higher in energy in the CDFT case. For practical purposes though, this energy differences are unimportant in the case of more complex systems (as we shall see on the next section).

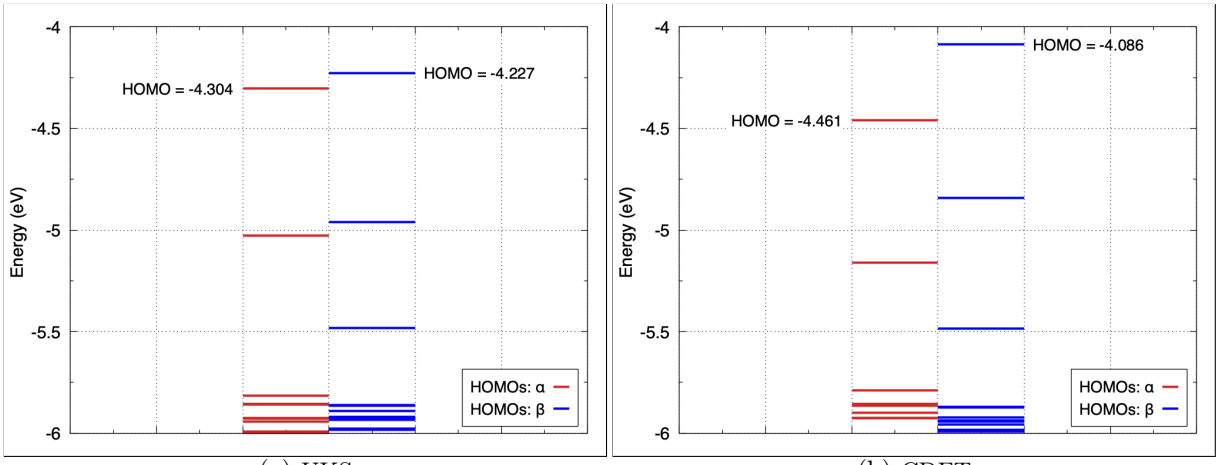

(a) UKS (b) CDFT

Figure 4.13.: Comparison between the HOMO levels of $TbPc_2$ simulations using UKS and CDFT.

We conclude, that the constrained calulations not only converged to (almost) the exact electronic and spin state of the system (with tiny spin contamination), but the energy levels retain qualitatively the same behaviour as the free-of-constrains simulations. The tremendous advantage of using CDFT is that even if the molecule is embedded or, as we shall see in further sections, deposited on top of another molecule, the magnetization and charge of the selected atom(s) will remain the same (i.e. no spurious spin contamination or charge leaking). It is also remarkable that without the usage of computationally more expensive approaches, such as using hybrid functinals, the level of accuracy predicting electronic properties of these types of SMMs is decent.

6. Transmission through real systems

After examining the molecules which are thought to be responsable of novel effects in the electronic transport in nanosystems, we move on to the full compounds in the measurements of the current. The main system under consideration consists on carbon nanotubes in top of which single molecule magnets are experimentally deposited to alter the electrical current of the CNT-FET [34]. In this work we tried to come as close as possible to this experimental realization by using carbon nanotubes with similar bandgap and the same type of element on the SMMs'. By observing the spectra on figures 4.5 and 4.6, the (9, 0) and (12, 0) remain as good candidates for being used as the building blocks of our simulations. Nonetheless, since the (12, 0) CNT has 12 more atoms per supercell than the (9, 0) and memory-wise the simulation of large systems is a bottleneck of DFT as well as diagonalization methods, we used the smaller CNT to build our system.

6.1. SMM + CNT

This geometry will serve as a guide for the more complicated, hence closer to reality system consisting on more magnets. It will also show how the extra molecule alters the density of states and therefore the transmission of the bare carbon nanotube previously discussed.

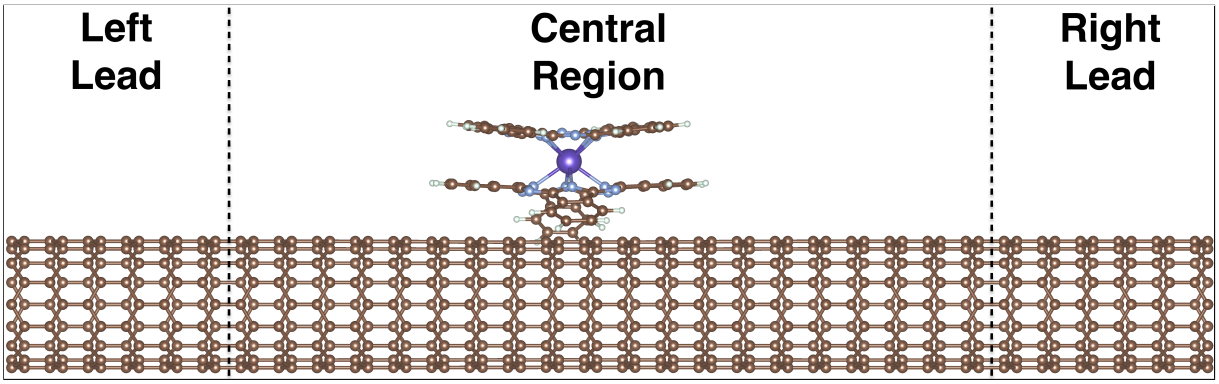

Figure 4.14.: Optimized geometry with one $TbPc_2$ molecule sitting on top of the carbon nanotube. Three periods of (9, 0) CNT were used for each of the leads and ten periods in the central region. The SMM lower ligand surrounds the CNT so that along the CNT axis, the ligand is planar while it is distorted along the CNT diameter.

The optimized geometry of the system is depicted on figure 4.14 which consists on 16 periods of tube, three of which acted as the left lead and another three as the right lead. This left us with a total of ten carbon nanotube supercells as the central system. In the central region, the single molecule magnet was deposited (without any optimization). The geometry then was relaxed using the parameters in table 4.4.

CP2K parameter	Value(s)
MAX_DR	1.0^{-3}
MAX_FORCE	1.0^{-3}
RMS_DR	1.0^{-3}
RMS_FORCE	1.0^{-3}
OPTIMIZER	BFGS
Basis set quality	DZV(P)
MINIMIZER	DIIS
PRECONDITIONER	FULL_ALL
ENERGY_GAP	0.1
XC_FUNCTIONAL	TPSS
VDW_POTENTIAL	DFTD3
Cell Dimensions	$[30.0, 68.16, 42.0]$

Table 4.4.: The most relevant parameters used on the relaxation of the first system containing one SMM.

After the geometry optimization, UKS and CDFT calculations were perfomed in the same geometry to compare the final spin state using both approaches. The CDFT constraints were set similar to the gas phase molecule $TbPc_2$ and so, a charge constraint of +26 and a magnetization of +6; in the case of the ligands a magnetization of +1. Their final values are shown in table 4.5

	Tb	**Ligands**
Charge	26.03350/26	–
Magnetization	5.96582/6	1.01446/1

Table 4.5.: Final values of the CDFT calculations for the system CNT+SMM. The extra electron on the ligands was constrained to be spin up electron.

The spin density (Fig. (4.15)) shows the substantial difference between both methods. In panel a, the spin density of the extra electron is localized in the 18 inner carbon atoms of the ligands as in the case of the gas phase calculation, nevertheless, the magnetization of the terbium atom is missing which tells us that the alpha and beta spin densities have the same values (same occupation for alpha and beta MOs). This is of course in disagreement with the intrinsic properties of the $TbPc_2$ and its electronic configuration. In the case of the CDFT calculation, not only the spin density of the whole molecule resembles the correct electronic configuration and localization of the spin, but bader analysis [69, 70, 71] reports a total charge in the terbium atom of 26.494 in the CDFT compared to the 27.074 of the spin polarized DFT. This is in good agreement with the charge of the experimental values of the terbiums' charge.

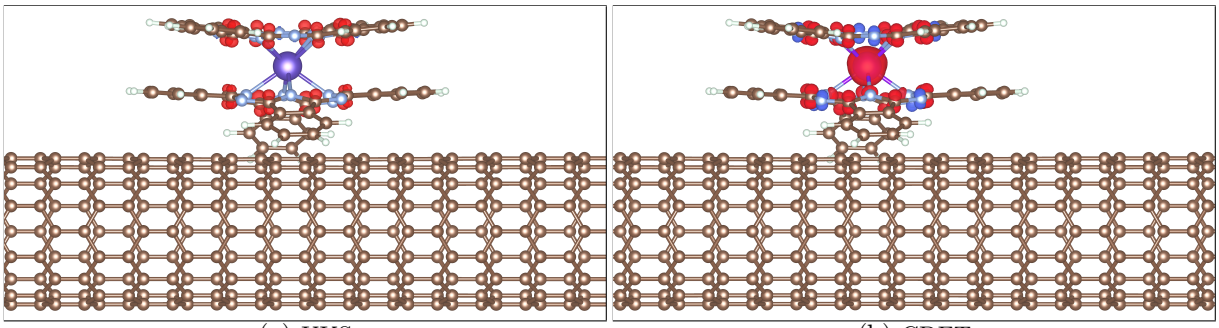

(a) UKS (b) CDFT

Figure 4.15.: Spin density for a $TbPc_2$ molecule on top of 16 periods of $(9, 0)$ carbon nanotube. Red color is an alpha excess spin density. Panel (a) shows a regular UKS calculation. In (b) magnetization and charge constraints were applied to the system.

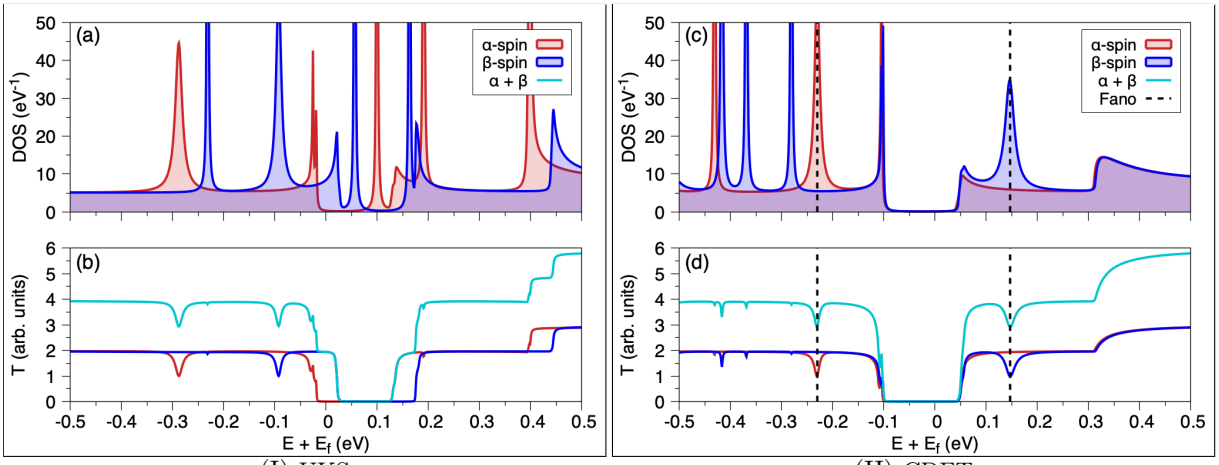

(I) UKS (II) CDFT

Figure 4.16.: DOS and transmission for a $TbPc_2$ molecule on top of 16 periods of (9, 0) carbon nanotube using two different methods: UKS and CDFT. The total transmission is plotted with a cyan line. Observe how the total transmission in the UKS shows artificial jumps in the total transmission which arise from an incorrect convergence on the DFT energy levels. Their effect is to schrink the value of the band gap of the bare (9, 0) CNT. These artificial features are corrected with the constraints applied to the system.

Figure 4.16 displays a comparison between UKS and CDFT methods for the DOS and transmission. It can be appreciated how in the UKS, the transmission for the alpha and beta channels are shifted with respect to each other creating artificial phenomena like the schrinking of the CNT band gap which leads to extra steps in the transmission. Using CDFT fixes this problems and places the Fermi levels of both spin channels in similar position so that the band gap of the CNT remains unaffected in tems of magnitude to that of the bare CNT. The total transmission ($\alpha + \beta$ transmission spectra) is also depicted.

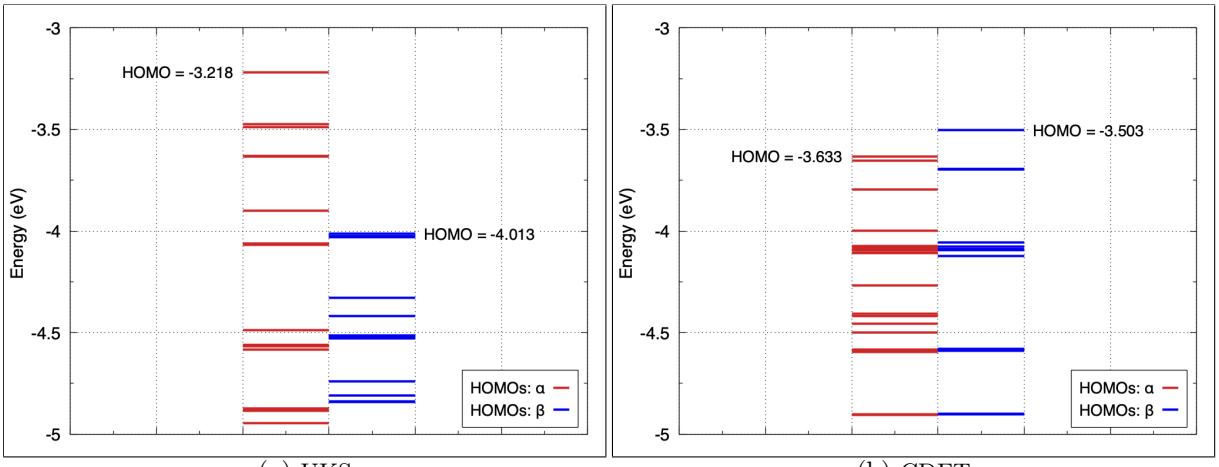

(a) UKS (b) CDFT

Figure 4.17.: DFT energy levels for a $TbPc_2$ molecule on top of 16 periods of (9, 0) carbon nanotube using two different methods: UKS and CDFT.

The huge difference between the transmission spectra on both methods can be more easily seen in figure 4.17 where the DFT energy levels are depicted for alpha and beta channels. The Fermi levels (which in this case are nothing more than the HOMO levels for alpha and beta MOs) in the UKS case are almost one electronvolt apart, causing that the average value E_f to shift the spectra of the alpha channel with respect to the beta channel. From now on we focus entirely on the CDFT simulations. The transmission presents two main depletions in the spectra at -0.23 eV and 0.147 eV marked with black dashed lines (panels c and d); these perturbations to the carbon nanotube are due to the hybridization of the molecular orbital of the SMM and the CNT. These depletions have been termed as 'Fano' type of resonances [72, 73] which make the electrons travelling through the CNT to jump into the SMM, then return to the CNT with a dephase in their wavefunction causing destructive interference with the electrons travelling through the CNT without seeing the SMM resulting in a decrease in the transmission values. This resonance will be studied in more detail in the following chapters.

6.2. 2 SMM + CNT

We now present the minimal example for which magnetoresistance (which is defined as the difference between the conductance in a system whenever a magnetic filed is applied minus the same system at vanishing magnetic field) has been observed in experimental realizations [34, 74]. This system comprises the (9, 0) CNT this time decorated with two $TbPc_2$ magnets on top. As we have seen in the previous sections, each of them will have a delocalized electron in the ligands which, experimentally, can be flipped by the introduction of an external magnetic field. In our simulations, the relative orientation of the unpaired electrons is set by the multiplicity of the whole system; thus, assuming all the unpaired electrons in the system are up electrons, we have a net spin per SMM of $S = 7/2$, which gives a total spin moment of $S_t = 14/2$; using the formula for the multiplicity $Mul = 2S_t + 1$ we have a total multiplicity of $Mul = 15$ to which we refer as *parallel* (or also *FE-FE* sometimes). Since it has been termed that the reason for the observation of the giant magnetoresistance on such a system is the alignment of the extra spin in the ligands, we have another spin configuration in which each of the SMMs' ligands spins are *antiparallel* (or *FE-AF*). Therefore, the total multiplicity of the system in this case is set to $Mul = 13$.

We optimize the structure using similar parameters as in table 4.4. After the geometry optimization, the distance between the SMMs and the CNT was $d_{SMMs-CNT} \sim 3.37$ Å and between the two terbium atoms was: $d_{Tb-Tb} \sim 20.51$ Å; thus, between the SMMs they were around 2 CNT unit cells. The optimized geometry is displayed in Fig. (4.18).

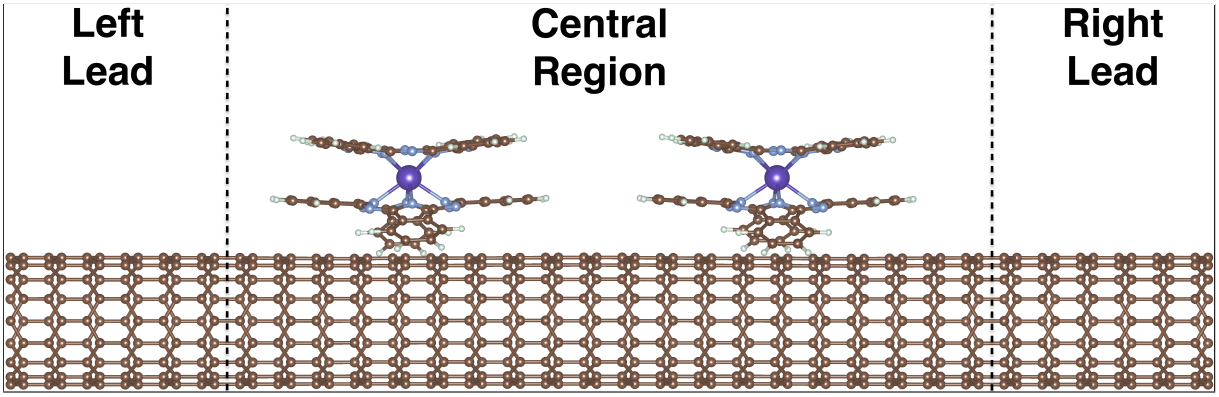

Figure 4.18.: Optimized geometry when two $TbPc_2$ molecules are sitting on top of the carbon nanotube.

In this case, the regular UKS procedure proved to be unreliable with respect to the electronic configuration of the system causing charge transfer between the SMMs and the CNT and some of the other problems already discussed on the system with one SMM. For these reasons, we only present the results of the CDFT method.

Constrained DFT simulations

The results of the single point CDFT simulations are displayed in figure 4.6 for the antiparallel case and in figure 4.7 for the parallel one. The simulations were carried out with a DZVP-MOLOPT-SR-GTH basis set for hydrogen, carbon and nitrogen atoms, while a DZV-MOLOPT-SR-GTH basis set was used for the terbium atoms. The two usual types of constraints were applied to both SMMs: charge and magnetization. The reasoning was similar to that on the gas phase simulations of $TbPc_2$. The magnetization of the ligands in the first SMM was set to $+1$ while in the ligands of the second SMM the magnetization depends on the alignment between the SMMs we wanted to achieve: for an antiparallel alignment the magnetization was set to -1 meanwhile for a parallel arrangement was set to $+1$. Finally again the charge and magnetization of the terbium atoms were set to $+26$ and $+6$ respetively. Tables 4.6 and 4.7 show the final values of the converged CDFT calculation in the FE-AF as well as in the FE-FE configurations.

	Tb (1st SMM)	**Tb (2nd SMM)**	**Ligands (1st SMM)**	**Ligands (2nd SMM)**
Charge	26.001612793/26	26.001603622/26	-	-
Magnetization	6.000432265/6	6.000033074/6	0.989457019/1	$-0.947458380/-1$

Table 4.6.: Final values of the constraints of the CDFT simulation of the FE-AF state.

	Tb (1st SMM)	Tb (2nd SMM)	Ligands (1st SMM)	Ligands (2nd SMM)
Charge	26.000041925/26	26.000951888/26	-	-
Magnetization	6.004073202/6	6.000348080/6	0.979597587/1	0.980006987/1

Table 4.7.: Final values of the constraints of the CDFT simulation of the FE-FE state.

Figure 4.19 contains the spin densities of both states from which one can see how the spin of the second SMMs' ligands is opposite on the FE-AF with respect to the FE-FE case. The majority of the alpha spin density is localized on the terbium atoms.

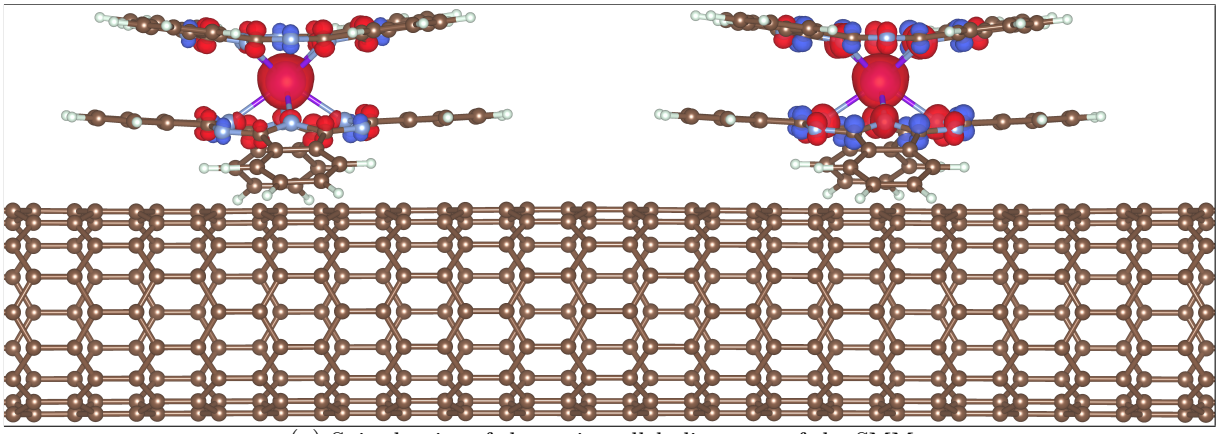

(a) Spin density of the antiparallel alignment of the SMMs.

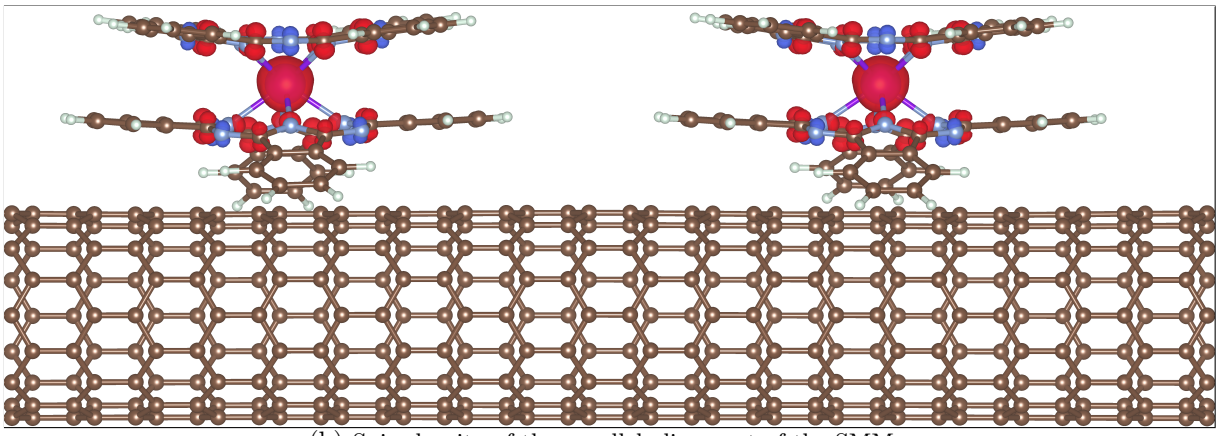

(b) Spin density of the parallel alignment of the SMMs.

Figure 4.19.: Zoom-in of the spin density of the two spin states. Red is a spin up (or alpha spin) and blue is for spin down (or beta).

We present the DOS and transmission spectra in figure 4.20. The transmission retains the overall shape of the bare (9, 0) CNT (displayed in color purple) but with depletions in both the valence as well as the conductance bands. They are the result of the interaction of the CNT with the energy levels of the SMMs and occur at different energies for the FE-AF as for the FE-FE case since the energy levels of the SMMs reorganize differently as a consequence of the occupation of the molecular orbitals for both spin configurations.

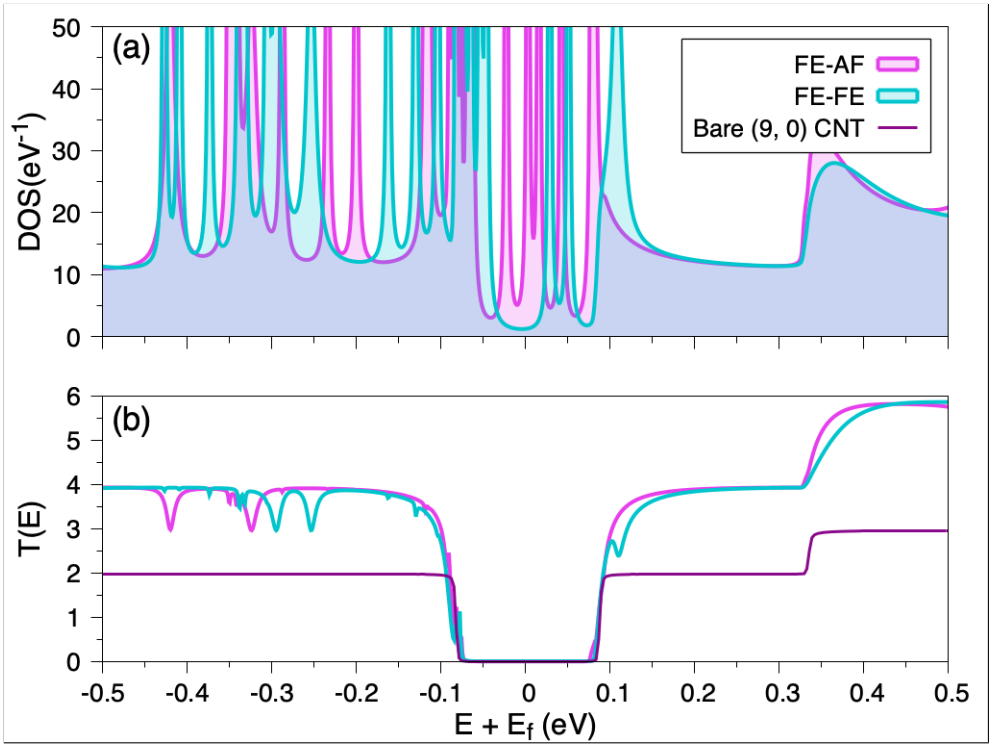

Figure 4.20.: Density of states and transmission coefficient for the FE-AF as well as the FE-FE simulations of the (9,0) CNT+2TbPc$_2$. In the transmission, the spectra of the bare (9,0) CNT is overimposed for comparison. As it can be observed, the bandgap has the same magnitude for both type of simulations.

In order to proof that the resonances appearing on the electronic bands are indeed caused by the energy levels of the SMMs, one can plot the projected density of states (PDOS) per molecule per spin. These results are shown in Fig. (4.21).

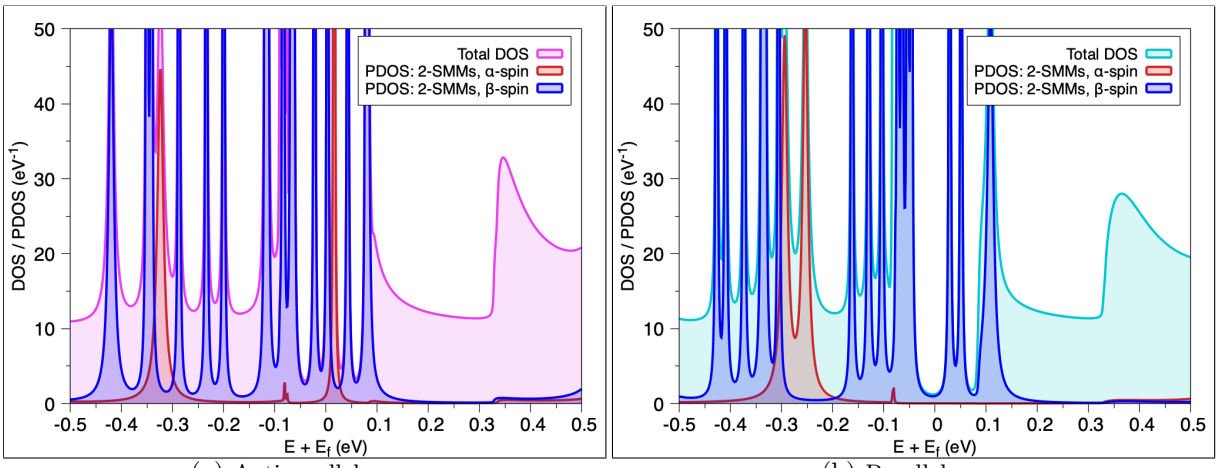

(a) Antiparallel case.

(b) Parallel case.

Figure 4.21.: (Projected-)Density of states for both spin configations. The PDOS is the sum of the states for both SMMs.

There are a couple of things one can learn from figure 4.21. Firstly we can distinguish two regions where the discrete levels of the magnets appear and affect the bare spectra of the tube. These regions correspond to the valence / conduction bands and the bandgap. In the case of levels from the SMMs which fall into the conduction bands, one can observe that not all of them hybridize the same way with the continuous spectra of the CNT. There are some very sharp peaks and others broad. Comparing the DOS/PDOS and T from figures 4.20 and 4.21 it is obvious that the larger the hybridization of the SMMs with the CNT, the broadener the peak and thus the more pronounced the depletion in the transmission coefficient. The sharper the peak, the less probably the electrons travelling with that energy through the CNT will jump into the SMMs and thus, the transmission gets less distorted.

6.3. Differential conductance plots

The quantities one can compare directly to experiments are the *current* ($I(V_{sd})$) and the *differential conductance* ($G(V_{sd})$); their expressions are given by the relations 4.8 and 4.9.
The different parameters affecting both quantities can be splitted into those modifying just the transmission coefficient, the ones modifying only the Fermi distribution function and those affecting both quantities. Their effect is summarized in the following paragraphs.

1. Parameters modifying the transmission coefficient only:

   a) Gate voltage (V_g): The impact of the gate voltage relies in its effect in the energy levels of the region to which the gate voltage is applied. The effect is to change the local density of states of the region by adding an extra constant energy term to the matrix elements of the Hamiltonian which describes the region of interest. This is taken into account direclty in the central system Hamiltonian and expressed by 4.16. With this consideration, the transmission coefficient is now a function of the gate voltage and consequently, the Landauer formula is now a function of three variables:

$$I(V_{sd}, V_g) = \frac{e}{\pi\hbar} \int_{-\infty}^{\infty} dE\, \mathcal{T}(E, V_g) \Big[f_s(E, V_{sd}) - f_d(E, V_{sd}) \Big]. \tag{4.26}$$

   And similarly for the conductance $G(V_{sd}, V_g)$.

2. Parameters modifying the Fermi distribution function only:

   a) Temperature (T): the temperature will set the number of electrons that will participate in the transmission process. It widens the shape (high temperatures) or narrows down (low temperatures) the shape of the Fermi function.

   b) Electrochemical potential (μ): this quantity represents the highest occupied energy level of the whole system into consideration. At zero bias, the electrochemical potentials of the leads and the electrochemical potential of the central region are located at the same level. If the temperature is 0, then this quantity is known as the Fermi level.

3. Parameters modifying the transmission coefficient and the Fermi function:

   a) Source-drain voltage (V_{sd}): this quantity is the responsible for making the electrons to flow from one reservoir (e.g. left) to the other one (e.g. right) or vice-versa. It defines a region where the electrons in the central region can conduct; this region is usually called *Fermi window* or *transport window*. Mathematically is given by the difference between the Fermi distribution functions of the source and the drain contacts.

In the integration of equation 4.9 the Fermi window effectively defines the current through the system through the Fermi functions. For low temperatures and low bias voltages, the energy range where the values of $f_s(E, V_{sd}) - f_d(E, V_{sd})$ are different from zero are reduced to a small energy range in the order of 1×10^{-2} V. As a consequence of this, the current flowing through a nanosystem will be completely determined by the values of the transmission in a quite reduced range. Figure 4.22 shows graphically the order of magnitudes of the Fermi window for several temperatures and bias voltages.

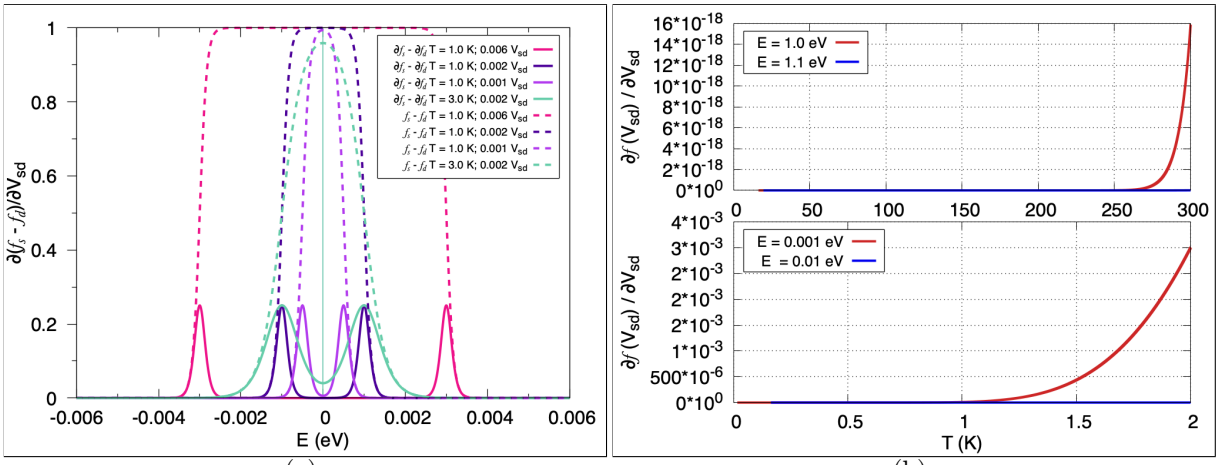

(a) (b)

Figure 4.22.: $\partial f_d(E, V_{sd})/\partial V_{sd}$ for different temperatures and source-drain voltages. In a) the Fermi window is the area under the dashed curves; only in this region the current is different from zero. In b) the derivative of the Fermi function is plotted as a function of the temperature. One can observe how low the values of $f(E, V_{sd})$ are for low temperatures which numerically is a challange.

In our simulations, the temperature was always set to 1 K in order to come as close as possible to the experiments where the giant magnetoresistance was observed at temperatures in the range of $[0.6, 0.04]$ Kelvin [34]. In figure 4.23 the *stability diagrams* for the simulations of the (9, 0) CNT+2SMM are shown. The plots show the differential conductance of the system as a function of the bias and gate voltages.

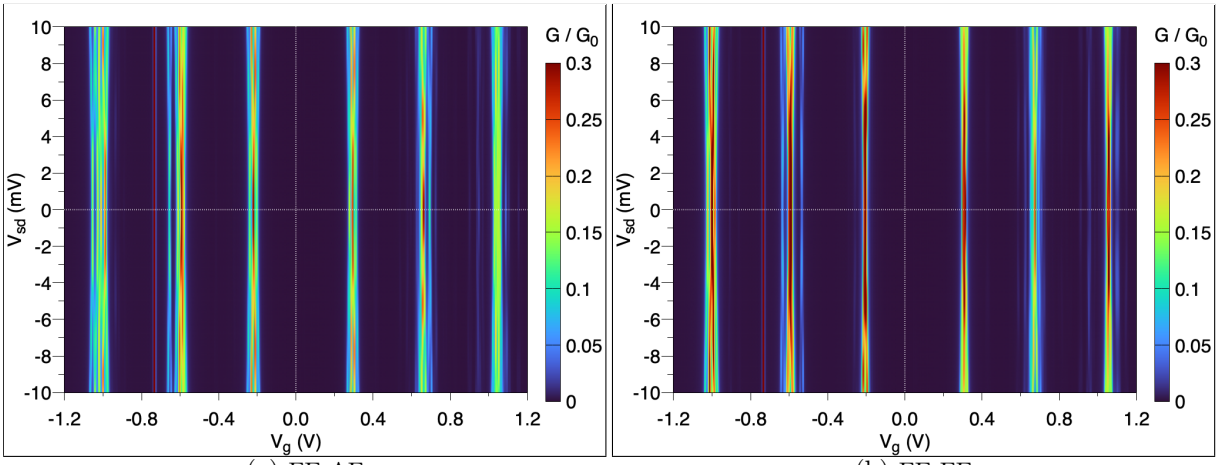

(a) FE-AF (b) FE-FE

Figure 4.23.: Differential conductance stability maps for the 16 periods of (9, 0) CNT decorated with two SMMs on the central region. a) Shows the antiparallel alignment of the SMMs extra spin on the ligands with respect to each other. b) The parallel configuration.

As it can be seen, the differential conductance is different from zero for both spin configurations at $V_g \sim [-1.0, -0.6, -0.2, 0.31, 0.67, 1.05]$ V. The regions where this occurs resemble the well known Coulomb diamonds in quantum dots [75, 76, 77]. In the parallel case, these diamonds present higher conductance values for most of the gate voltages. Take as an example the diamond at $V_g = 0.206$V and make a constant gate voltage plot to directly compare the conductance for both spin systems. Figure 4.24 shows this comparison.

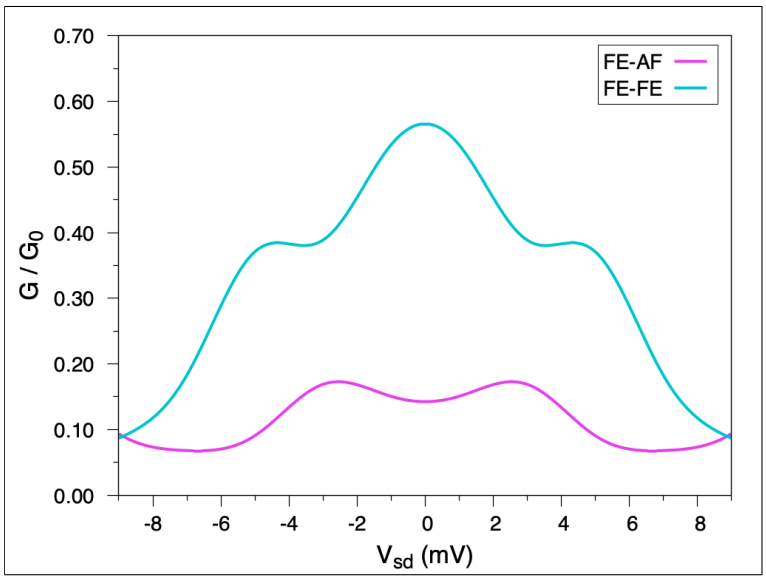

Figure 4.24.: Comparison between the conductance between the antiparallel and parallel configurations at constant gate voltage ($V_g = -0.206$ V). It is clear how the conductance for the parallel case is much larger exactly at the degeneracy point ($V_{sd} = 0$).

6.4. Magnetoresistance of the CNT + SMM system

Magnetoresistance is the change on the resistance of a material whenever an external magnetic field is applied. Mathematically is expressed via the following formula [78, 79]

$$MR = \frac{G(B \neq 0) - G(B = 0)}{G(B = 0)} \times 100\% \tag{4.27}$$

where G is the differential conductance and depends whether it is measured on a zero ($B = 0$) or finite magnetic field ($B \neq 0$). As already mentioned in this work, in the case of the CDFT simulations, the conductance at zero field would be substituted by the conductance in the FE-AF case; of course, the case when $B \neq 0$ would correspond to the FE-FE state, thus equation 4.27 would be written as

$$MR = \frac{G_{FE-FE} - G_{FE-AF}}{G_{FE-AF}} \times 100\%. \tag{4.28}$$

By taking the same degeneracy point as in 4.24 and substituting the values for G in 4.28 we get

$$MR = \frac{0.5657 - 0.1425}{0.1425} \times 100\% = 296.80\%, \tag{4.29}$$

which is in excellent agreement with the original paper of the SMMs supra-molecular spin-valves [34] in which a giant magnetoresistance of 300% was measured. The MR could be even increased in the case of our simulations if more than two SMMs were added to the CNT. This would lead us to several spin sub-states each of them corresponding to a specific experimental setup. In principle, using CDFT, the correct spin state would be properly set not only for terbium based magnets, or even the same type of SMMs, but it can be extended to any SMM containing any type of atom(s).

These results are just showing the reliability of the CDFT+NEGF as well as the relatively cheap computational cost (compared to wavefunction or many-body methods) and accuracy to predict spin-dependent transport in systems containing highly correlated materials where regular DFT theory is not enough to fully capture the electronic properties of such systems. In the following chapter we shall study more in detail the physical mechanism which gives raise to curious behaviour of the transport in the CNT+SMM FET.

7. Empirical model of the spin-valve mechanism

The last sections have shown how, by means of first-principles calculations (CDFT), one can model the desired electron and spin density in a magnetic system; mathematically, this contraint will affect two quantities on the KS-formalism: the spin polarized density matrices and the spin polarized Kohn-Sham matrices. In other words, the energy levels (intrinsically given by the KS-matrices) for each of the spin channels will be reorganized due to the occupation (intrinsically given by the density matrices) and therefore, the overall density of states. This information will then be passed to the Green's function through the KS-matrices, from which in top of the DOS, the transmission will be calculated. In this section an empirical tight-binding Hamiltonian is develop in order not only to give a clearer look, but also to validate the mechanism behind the spin-valve observed on the experimental as well as in our theoretical calculations.
The first object to model is the carbon nanotube-like spectra with the minimal set of atoms per unit cell and orbitals per site. There are several works dedicated exclusively to the study of such systems for example the PhD. theses by Nemec [80] or Zilly [81]. There are two main differences between those works and this one: the spin polarization of the linear chain of atoms and the addition of the impurities which mimic the SMMs. To this end, the minimal quantum dot in our empirical spin-valve system will consist on a linear chain of 6 atoms; each of the parts on the NEGF method consists on two atoms. To simulate the single molecule magnets, two extra sites were added in the central region. The diagram of our model is present in figure 4.25.

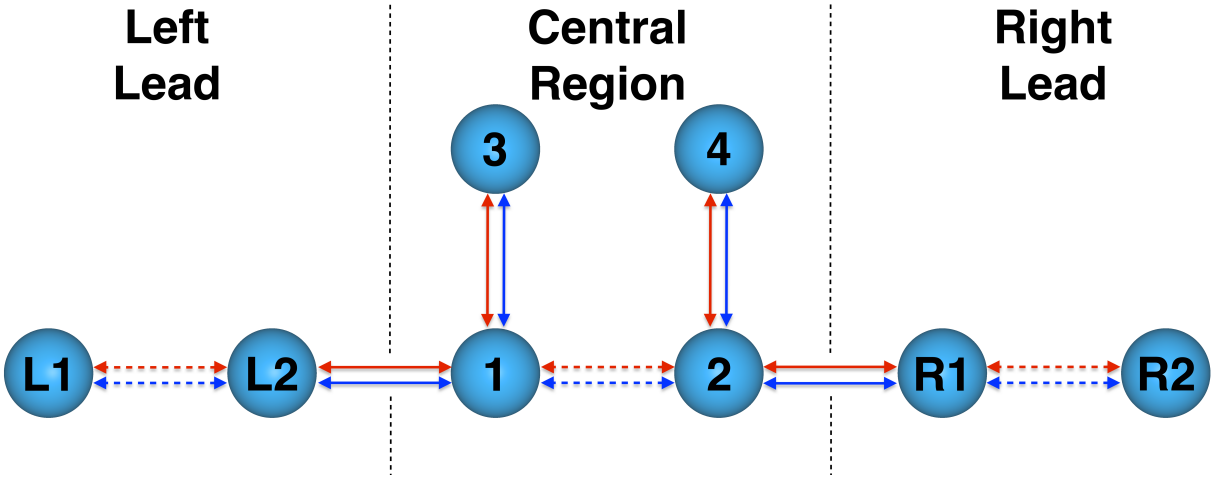

Figure 4.25.: General scheme of the empirical model. Arrows represent the interaction between sites; red/blue color means there is an interaction between alpha/beta energy levels of the atoms respectively. The black dotted lines denote the boundary limits between the different regions of the quantum dot.

From band structure theory, we know that a bandgap can be opened in a system by the introduction of two or more energy levels per atom. With this in mind, to mimic the bandgap structure of the carbon nanotubes used in this work, we set two orbitals per atom. The total number of orbitals counting spin is therefore four. In the following we denote the following variables:

k, k' label the orbitals, i, j the atom numbers and $\sigma = \alpha, \beta$ the spin. We can then write the Hamiltonians of the different parts of figure 4.25:

$$\begin{aligned}\hat{H}_C = &\sum_{\sigma}\sum_{i=3}^{4}\sum_{k=1}^{2}\epsilon^{i}_{\sigma,k}\big|\phi^{i}_{\sigma,k}\big\rangle\big\langle\phi^{i}_{\sigma,k}\big| + \sum_{\sigma}\sum_{i=1}^{2}\sum_{k=1}^{2}E^{i}_{\sigma,k}\big|\phi^{i}_{\sigma,k}\big\rangle\big\langle\phi^{i}_{\sigma,k}\big| + \\ &\sum_{\sigma}\sum_{i=1}^{2}\sum_{k=1}^{2}t^{i,i+2}_{\sigma,k}\Big[\big|\phi^{i}_{\sigma,k}\big\rangle\big\langle\phi^{i+2}_{\sigma,k}\big| + H.c.\Big] + \sum_{\sigma}\sum_{\substack{i,j=1\\ i\neq j}}^{2}\sum_{k=1}^{2}\tau^{ij}_{\sigma,k}\big|\phi^{i}_{\sigma,k}\big\rangle\big\langle\phi^{j}_{\sigma,k}\big|\end{aligned} \tag{4.30}$$

For the leads we have

$$\hat{H}_{L/R} = \sum_{\sigma}\sum_{i=1}^{2}\sum_{k=1}^{2}E^{i}_{\sigma,k}\big|\phi^{i}_{\sigma,k}\big\rangle\big\langle\phi^{i}_{\sigma,k}\big| + \sum_{\sigma}\sum_{\substack{i,j=1\\ i\neq j}}^{2}\sum_{k=1}^{2}\tau^{ij}_{\sigma,k}\big|\phi^{i}_{\sigma,k}\big\rangle\big\langle\phi^{j}_{\sigma,k}\big| \tag{4.31}$$

The basis fulfills:

$$\big\langle\phi^{i}_{\sigma,k}\big|\phi^{j}_{\sigma',k'}\big\rangle = \delta_{\sigma,\sigma'}\delta_{i,j}\delta_{k,k'}\big\langle\phi^{i}_{\sigma,k}\big|\phi^{j}_{\sigma',k'}\big\rangle. \tag{4.32}$$

The interpretation of the different terms in 4.30 and 4.31 is quite straight-forward: E and ϵ represent the on-site energies of the atoms belonging to the chain and defects respectively; the terms denoted by the Greek letter τ correspond to the interaction within elements in the chain, which in figure 4.25 correspond to interaction between atoms: $L1 - L2$, $1 - 2$ and $R1 - R2$. Interaction terms between atoms $1 - 3$ and $2 - 4$ are disclosed in the variable t.

The matrices missing in this model are those matrices that make the connection between the different parts of the transistor (leads and center); they are given by expressions A.7 and A.8 of the appendices.

To better understand the different terms in our model, figure 4.26 presents an energetic type of diagram that, together with 4.26 give a whole picture of how the system was modelled.

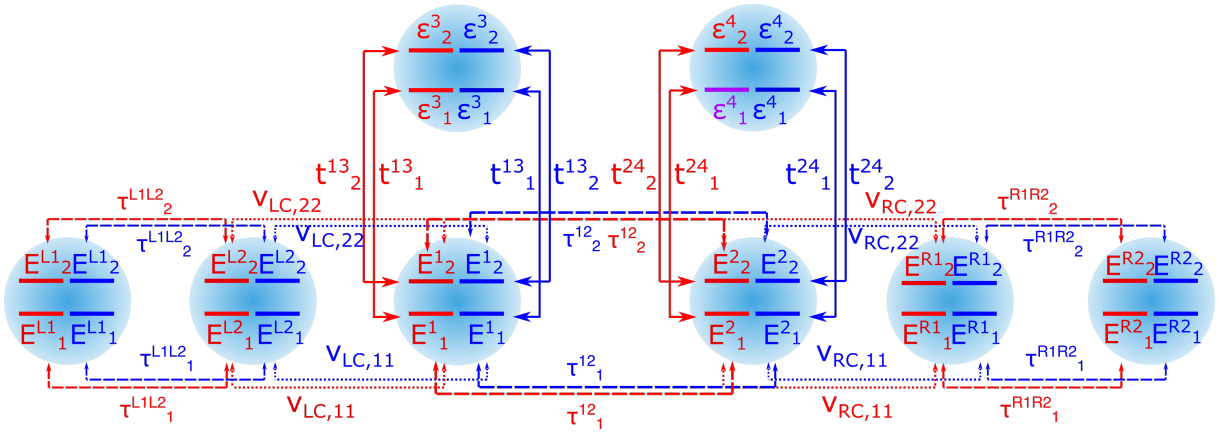

Figure 4.26.: Energy type of diagram of the empirical model. The interactions between the different discrete levels are also shown with full, dashed and stripped lines. Red/blue stands for alpha/beta spins respectively. The energy level responsible for the differences in the DOS and transmission spectra is depicted in purpule.

Appendix A depicts all the matrices from equations 4.30 and 4.31. The way the two different spin states corresponding to the antiparallel or parallel alignment of the defects is regulated, is through the values of the on-site energy levels in atoms 3, 4; this choice has not been done randomly and corresponds to the hypothesis from the original paper [34]; the logic is that, when an external magnetic field is applied to the system, so that both magnets are magnetized in the same way, they share similar electronic structure, or in terms of eigenvalues, they have energetically similar energy levels. Therefore, to model a FE-FE state, we simply set equal values of the atoms 3 and 4: $\epsilon^3_{\sigma,k} = \epsilon^4_{\sigma,k}$. On the other hand, for the state FE-AF there is no magnetic field applied and the energy levels of both defects are in principle at different positions in energy. One can then move the on-site energies of the respective spin channel in either atoms 3 or 4 which, in order to be consistent with our previous nomenclature, we chose to modify atoms' energy levels in 4. In order to come as close as possible to the real system, the bandgap on the empirical model has been chosen to have the same magnitude as (9, 0) CNT.

7.1. Numerical approach to the empirical Hamiltonian

Figure 4.27 shows the spectra of the empirical system which in this case lacked of interaction between the chain and the defects (i.e. $t = 0$), thus the spectra resembles that of a simple linear chain. The size of the bandgap is $\Delta = 0.14$ eV.

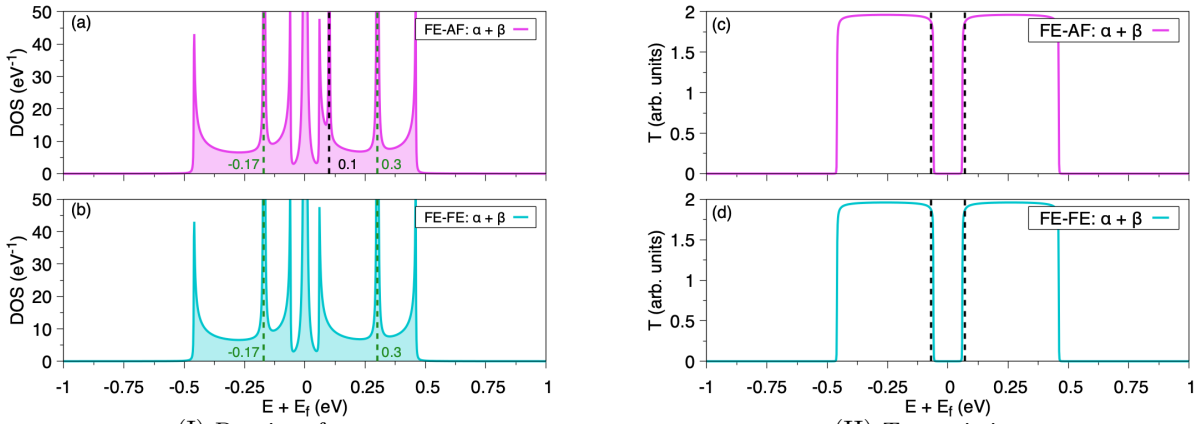

Figure 4.27.: The antiferromagnetic (FE-AF) and ferromagnetic (FE-FE) spectra for the toy model. In the DOS of the FE-AF case, a dashed line indicates the extra van Hove singularity due to the different value of the on-site energy $\epsilon^4_{\sigma,k}$ with respect to the FE-FE case. In the case of the transmission, two dashed black lines depict the bandgap's borders of the (9, 0) CNT, which, as it is clearly seen, it is comparable to the empirical chain.

The full set of parameters chosen to reproduce Fig. (4.27) are written in tables B.1 and B.2 in appendix B. There are some general observations that can be made on the spectra 4.27: the DOS presents several van Hove singularities across the energy range which do not have an effect on the transmission. Such singularities are observed for the FE-AF case at: $\sim [-0.17, 0.00, 0.10, 0.30]$ eV, while for FE-FE $\sim [-0.17, 0.00, 0.30]$ eV. The extra singularity for the FE-AF case (at $E = 0.1$ eV) comes from the discrepancy of the on-site energy $\epsilon^4_{\alpha,1}$ between both states. Also, even though the DOS presents extra van Hove singularities, where in principle electrons could sit, since the coupling between the chain and the defects is 0, the transmission shows an almost regular tight binding linear chain spectra (appart from the bandgap, obviously).

Now let us switch on the coupling to the defects of the central region. To observe the effect on the parameter t in the DOS / T, we first turn on the α coupling between atoms 1 and 3. The value was $t^{13}_{\alpha,1} = t^{31}_{\alpha,1} = 0.1$ eV. Figure 4.28 depicts the quantities of importance. In this case, the total transmission as well as the transmission per spin channel have been plotted to observe the effect of $t^{ij}_{\sigma,k}$.

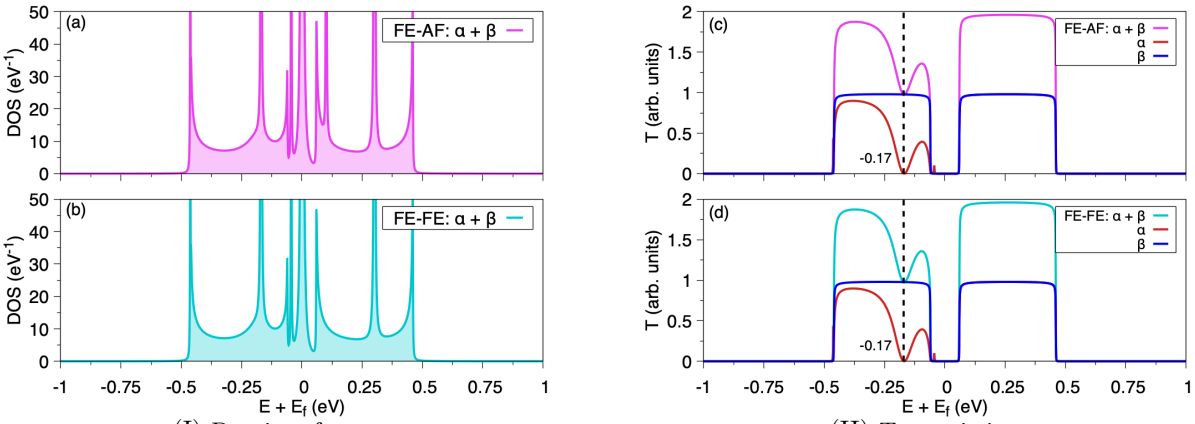

(I) Density of states (II) Transmission

Figure 4.28.: Density of states and transmission of the empirical model with the interaction between atom 1 and 3 is switched on for the alpha channel of the lowest energy orbital.

As it can be seen, the density of states around the valence band got distorted and its value increased with respect to the regular isolated chain. But an increase on the DOS was not the only feature when the system interacts with a defect, since now a particle traveling through the chain can also jump into the first defect and then when it goes back to the chain, it interacts destructively with the wavefunction of a particle travelling through the chain without jumping to the defect, thus reducing the transmission. This can be observed in the spectra for T in 4.28. This type of valley is the same as the valleys found in the CNT+SMMs system. They are termed as Fano resonances [72, 82]. The strenght of the coupling to the defects will regulate the width of the resonance; the evolution of the valley for different values of t can be observed in figure 4.29. Intuitively, what happens is that the larger the coupling, the higher the probability an electron will jump into the defect.

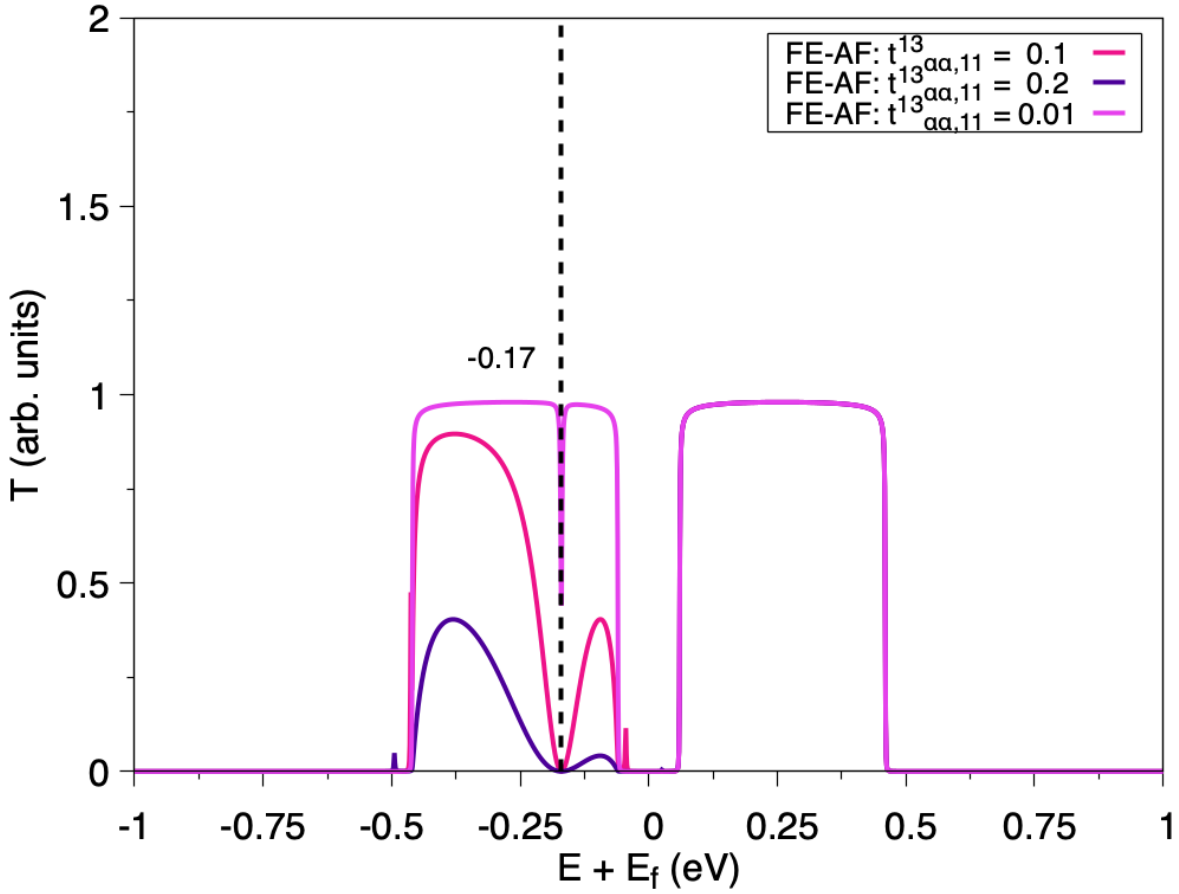

Figure 4.29.: Transmission coefficient for different values of $t^{13}_{\alpha\alpha,11}$. In the picture, only the alpha channel is depicted. The value of the resonance coincides to that of the on site energy value for the defect, in this case $\epsilon^3_{\alpha,1} = -0.17$ (black dashed line).

The results are consistent with the so-called Fano-Anderson model which consist of a tight-binding linear chain side-coupled to a defect. In a very simple picture, the Hamiltonian of such a system can be written as [82, 83, 84]:

$$H = C\sum_n \left(\psi_n \psi^*_{n-1} + c.c.\right) + E_F|\phi|^2 + V_F(\phi^*\psi_0 + c.c.). \tag{4.33}$$

In equation 4.33, ψ corresponds to the wavefunction of the linear chain, ϕ is the wavefunction of the Fano-Anderson defect and E_F its on-site energy. Finally, the chain-defect coupling strength is given by the constant V_F.

The general expression of the transmission coefficient for the case of a continous of energies interacting with a descrete level (Fano-Anderson model) can be calculated using the transfer matrix approach [85] which gives the result [82, 86]

$$T = \frac{\alpha_k^2}{\alpha_k^2 + 1}. \tag{4.34}$$

where the parameter α_k is a function of the coupling between the chain and the defect

$$\alpha_k = \frac{c_k(E_F - \epsilon_k)}{V_F^2} \tag{4.35}$$

here $c_k = 2Csin(k)$. One can see that in the limit when $\alpha \to 0$ the transmission also goest to zero. This happens at the Fano energy E_F and it can clearly be seen in figures 4.28 and 4.29 where the black dashed lines denote the value of the defects' energy. The broadening of the Fano resonance is written as

$$\Gamma = \frac{V_F^2}{Csin(k_F)} \tag{4.36}$$

thus, the strongest the coupling to the defect, the broadened the fano resonance. This is also observed in our simulations (Fig. (4.29)) where the Fano level has gained a large broadening allowing electrons within a larger energy range to jump into the defect and thus, cause destructive interference in this range.

Therefore, our results are in agreement (at least qualitatively) with previous observations in related systems. Nonetheless, our system presents one very different and interesting feature namely the emergence of a finite transmission peak outside of the valence and conduction bands which we will discuss later in this work. This feature will have a tremendous impact on the current.

It is also important to notice, that if the value of the energy level in the defect is considerably larger than that one of the linear chain, the density of states will show a peak close to the on-site energy of the defect (though not exactly at the same energy), but no Fano resonance will be observed in the transmission coefficient as in figure 4.30; on the other hand, the extra peak outside of the valence/conductance bands also is not longer noticeable both in the DOS and transmission.

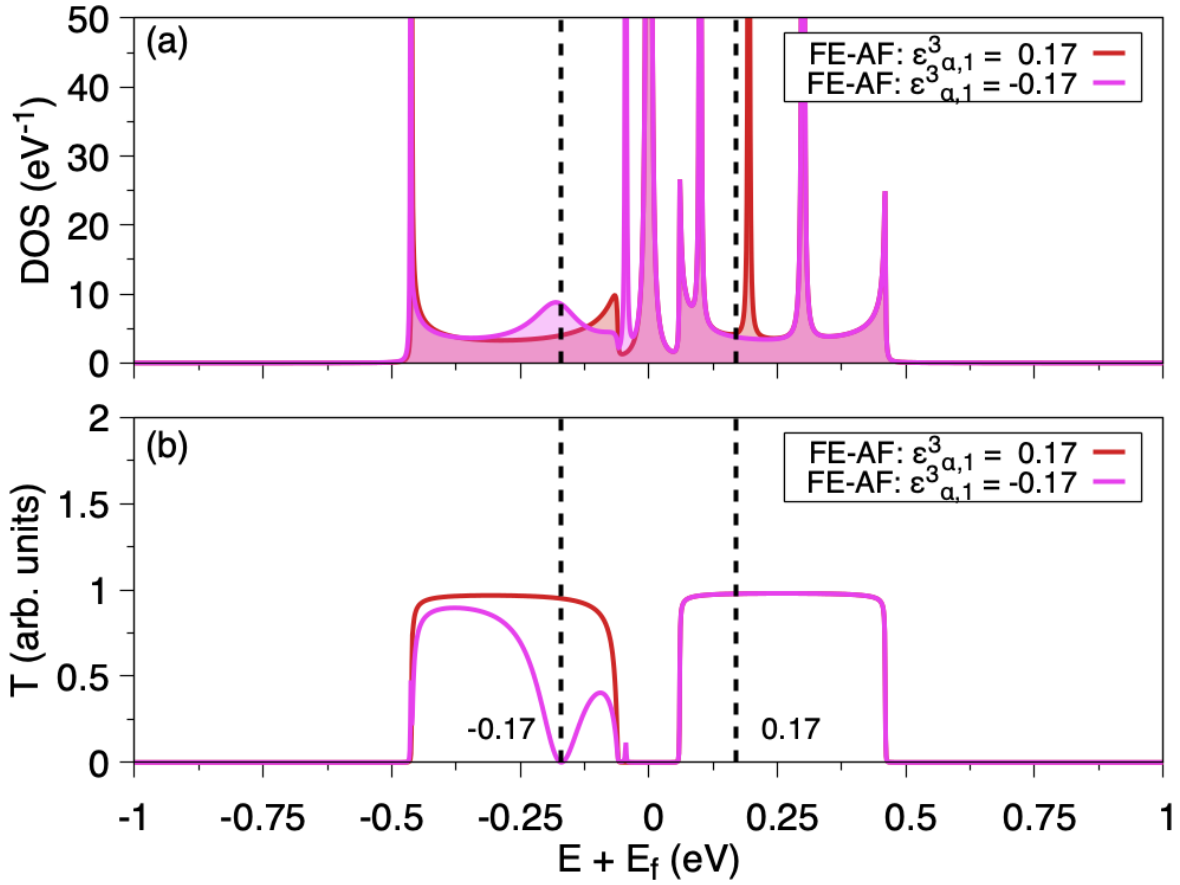

Figure 4.30.: Density of states and transmission for two different values of the on-site energy $\epsilon^3_{\alpha,1}$ (black dashed lines) and $t^{13}_{\alpha\alpha,11} = 0.1$. Again, only the alpha channel is shown. Here, $E^1_{\alpha,2} = 0.26$.

Having observed the effect of several parameters of the toy model, we can now switch the interaction of the second defect (in the CNT+2TbPc$_2$ system it would correspond to the second SMM). For this purpose we set the coupling between atoms 2 and 4 to $t^{24}_{\alpha,1} = t^{42}_{\alpha,1} = 0.1$; the full set of values are written on tables B.1 and B.3.

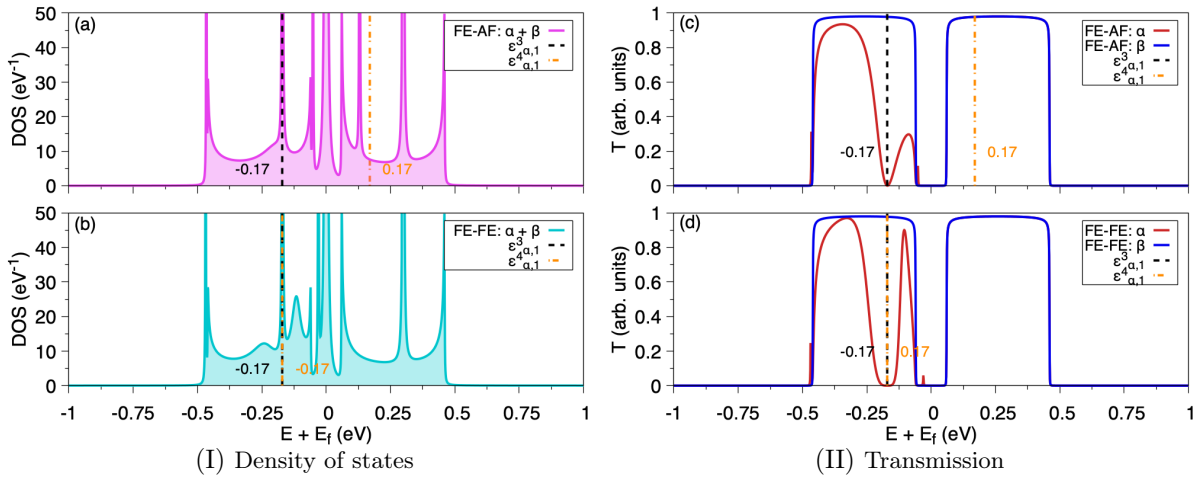

Figure 4.31.: DOS and T of the FE-AF and FE-FE systems. In this case, the interaction between the lower energy levels of the α-spin between atoms $1-3$ and $2-4$ was switched on. The black and orange dashed lines correspond to the on-site energies $\epsilon_{\alpha,1}^{3/4}$ of the defects 3, 4.

As expected (Fig. (4.31)), the spectrum looks rather similar to that in figure 4.28 since the energy $\epsilon_{\alpha,1}^{4}$ lays far away in energy with respect to $E_{\alpha,1}^{2}$. For the parallel case the Fano resonance also appears at $E = -0.17$ but this time is broadened due to the fact that now both of the energies of the defects are at the same position $\epsilon_{\alpha,1}^{3} = \epsilon_{\alpha,1}^{4} = -0.17$.

We notice also that the number of peaks outside of the conduction bands corresponds to the energy levels available at that energy range. The origin of such peaks can be either from the linear chain or the defects. We can now expeculate that by switching on other couplings ($t_{\sigma,k}^{ii}$), the spectra will present similar characteristics as in the previous examples but mirrored on the conduction band, which is indeed the case. Figure 4.32 shows these results; parameters to reproduce these images are given in B.1 and B.4.

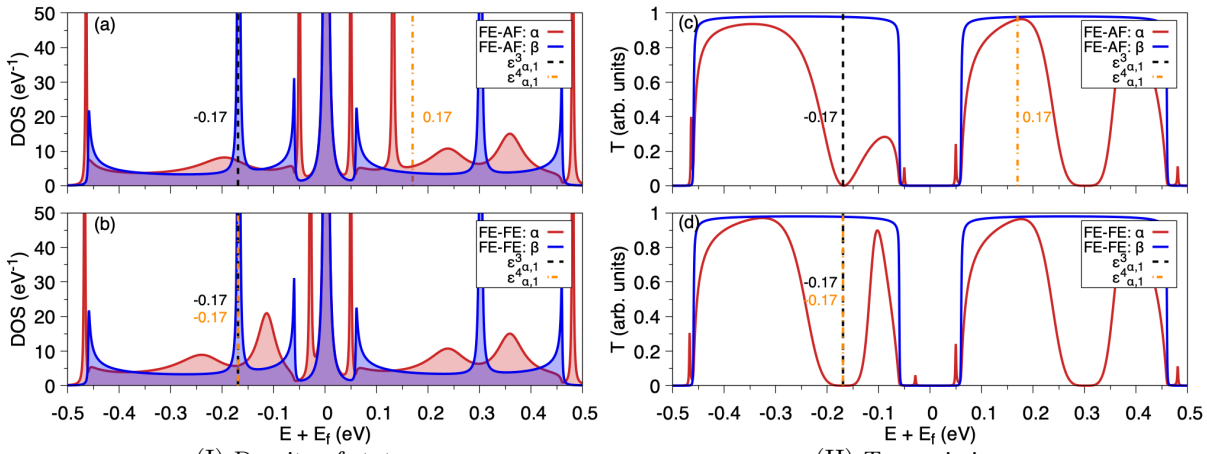

(I) Density of states (II) Transmission

Figure 4.32.: Spectra per spin channel when the interaction between alpha channel energy levels (i.e. $t^{(13,24)}_{\alpha,(11,22)} = 0.1$) is switched on. Upper row FE-AF case, lower row FE-FE.

To have a better understanding of DOS and transmission, one can also diagonalize the central Hamiltonian $\mathbf{H}^{\sigma}_{C}$ and visualize the *bare* eigenvalues (which in this context *bare* means that they are the eigenvalues of the central part (chain and defects) without taking anything else into consideration). Figure 4.33 shows the energy levels of the central system per spin channel. For the beta levels there is no difference in the distribution between FE-AF and FE-FE state since the matrices are identical. For the alpha channel though, the distribution is different due to the different on-site energies of atom 3 ($\epsilon^3_{\alpha,1}$), from which one can also visualize the energy levels responsible for the Fano resonances (between the energy range $[-0.1, 0.2]$ eV).

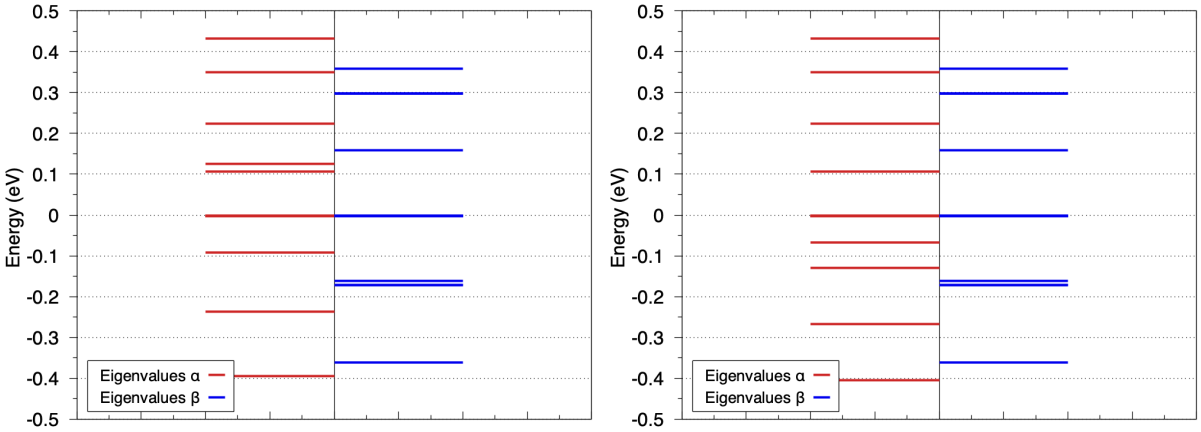

(a) Eigenvalues of $\mathbf{H}_C$ for the FE-AF case. (b) Eigenvalues of $\mathbf{H}_C$ for the FE-FE case.

Figure 4.33.: Eigenvalues per spin channel of the system in figure (4.32).

Moving forward, we can now switch on the interaction of the beta levels between the chain and the defects to have an overall picture of the full transmission spectra. We use the same value as for the alpha channel, i.e. $t^{(13,24)}_{\beta,(11,22)} = 0.1$.

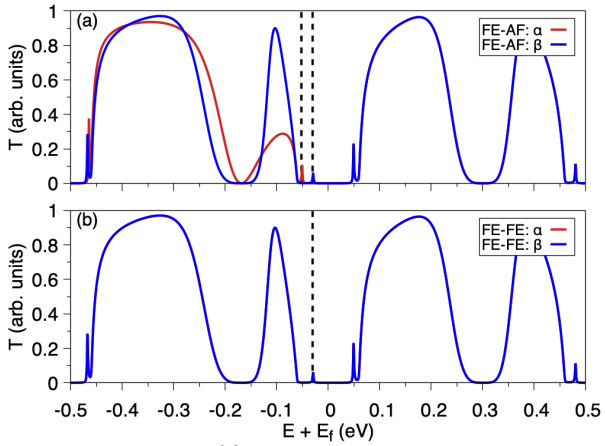

(I) Transmission.

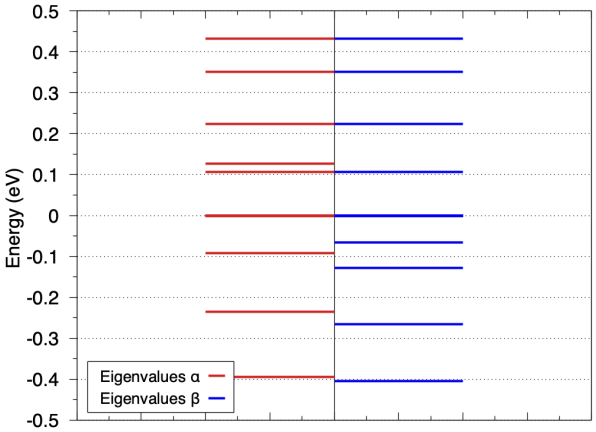

(II) Eigenvalues of $\mathbf{H}_C$ for the FE-AF case.

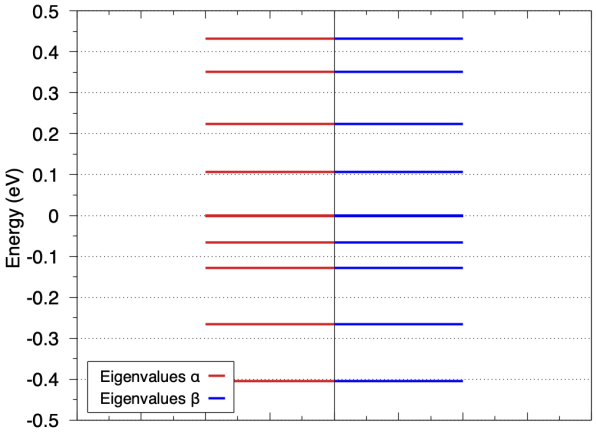

(III) Eigenvalues of $\mathbf{H}_C$ for the FE-FE case.

Figure 4.34.: Transmission profile as well as the energy levels of the central Hamiltonian when all the interactions in the empirical system are turned on.

In the FE-AF case, if one compares the energy arrangement between both spin channels, one realizes that the position of the on-site energy of atom 3 ($\epsilon^3_{\alpha,1}$) makes the valence band energy levels to reorganize differently than the beta levels, which not only leads to a different shape on the transmission on the valence region but the peaks around $E = 0.05$ eV for alpha and beta channels are now in different positions. The conduction band remains without any change.

7.2. Low energy regime

As has been already discussed in the CNT+2TbPc$_2$ simulations, for the low bias regime (in this work $V_{sd} \sim 20$ meV) the current and differential conductance will be proportional to the transmission coefficient value around the Fermi energy. In our simulations, the Fermi energy

is located at $E_f = 0$, therefore in our toy model we restrict the sampling range to where the bandgap is. To study the evolution of the non-zero transmission peaks around the band gap, figures 4.35 and 4.36 show a color plot of the transmission coefficient as a function of $t^{i,i+2}_{\sigma,k}$.

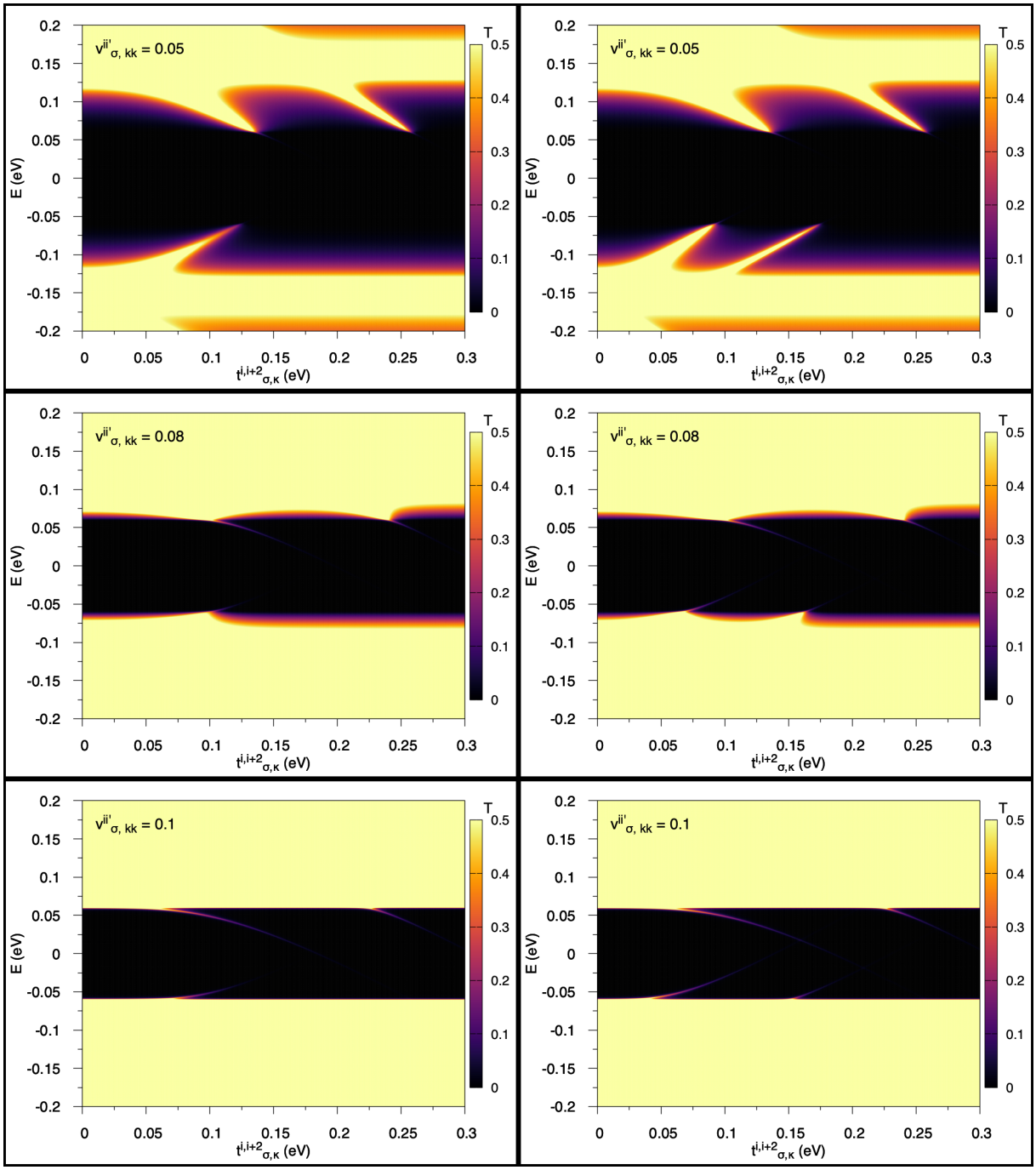

Figure 4.35.: Transmission coefficient spectra as a function of the coupling between the atoms 1/2 with atoms 3/4 for different values of the coupling of the central region with the leads. Left/right columns are the FE-AF/FE-FE cases respectively.

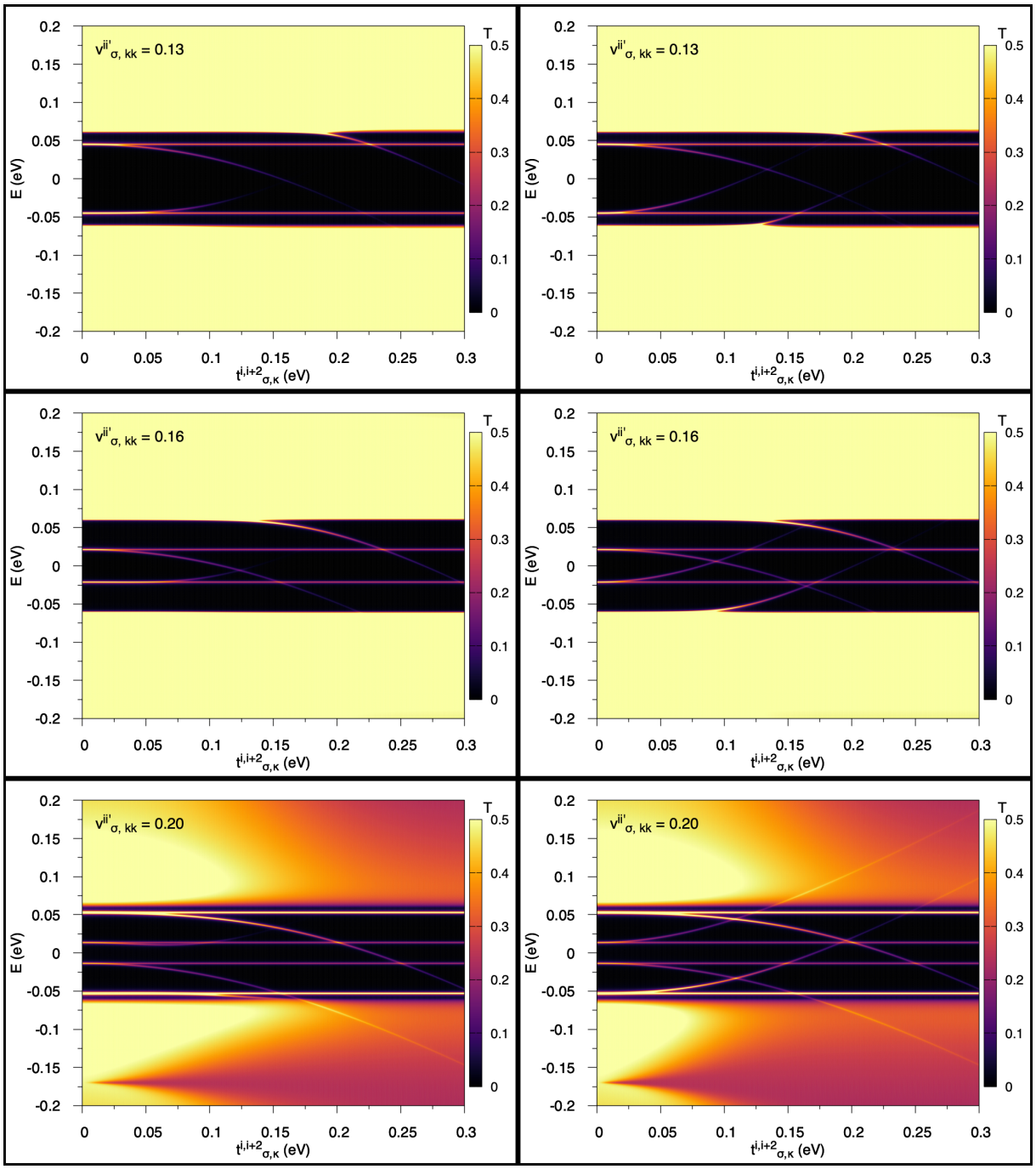

Figure 4.36.: Transmission coefficient spectra as a function of the coupling between the atoms 1/2 with atoms 3/4 for different values of the coupling of the central region with the leads. Left/right columns are the FE-AF/FE-FE cases respectively.

As it can be seen, the fact that the on-site energy $\epsilon^4_{\alpha,1}$ for in the FE-FE case, makes that an extra 'pole' emerges at the edge of the valence band. The energy range in which the poles within the bandgap have a finite value, increases as the coupling between the leads and the central region increases, which is of great interest in our case for having a non-zero current at the Fermi

window. In these cases, the evolution of the valence and conduction bands are irrelevant for the analysis of the next results.

With all this in mind, we can now calculate the differential conductance maps for our empirical system. Using the results from 4.35 we set the parameter $v^{ii'}_{\sigma,kk}$ to 0.2 eV. The full set of individual terms are written in tables B.1 and B.5

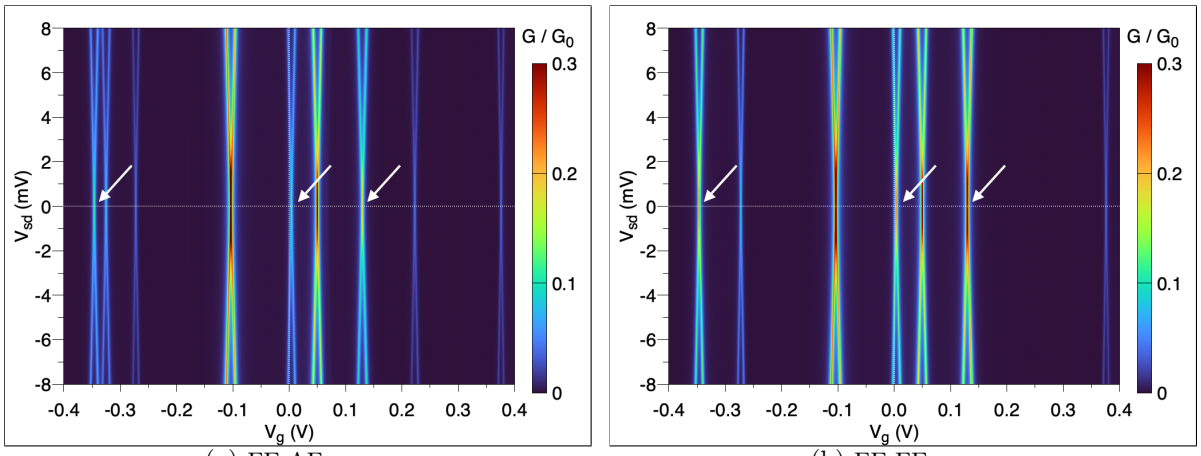

(a) FE-AF case. (b) FE-FE case.

Figure 4.37.: Stability diagrams for the empirical model simulating a linear chain of atoms with two defects on the central region. The differential conductance is in units of the quantum conductance G_0. The white arrows denote the peaks at which the FE-FE alignment shows a larger conductance value.

Figure 4.37 presents the stability diagrams for the empirical model for both spin configurations FE-AF and FE-FE from where we can see how the spectra resembles the simulations of the real system. The diamonds at $\sim [-0.35, 0.01, 0.13]$ V_g for the FE-FE case present a larger value for the conductance compared to the FE-AF case. The reason is that, in the FE-FE case, the total transmission is the sum of alpha and beta transmission coefficient different from zero around the Fermi window. For the same gate voltages though, the total transmission in the FE-AF case is just the sum of a transmission coefficient different from zero for one of the spin channels. To prove this, let us consider the diamond at $V_g = 0.13$V and plot its transmission spectra for both spin channels.

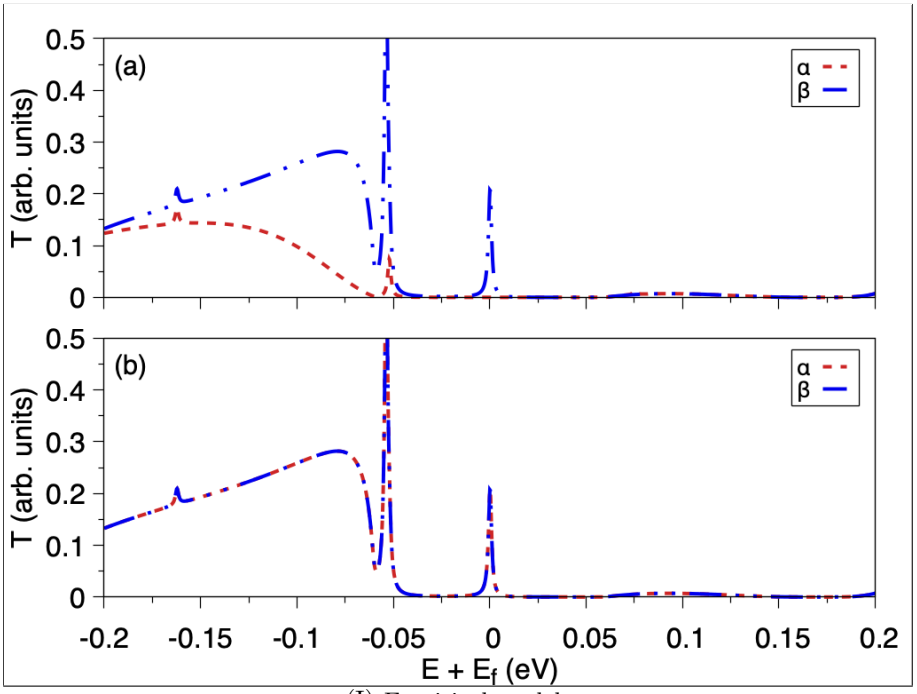

(I) Empirical model

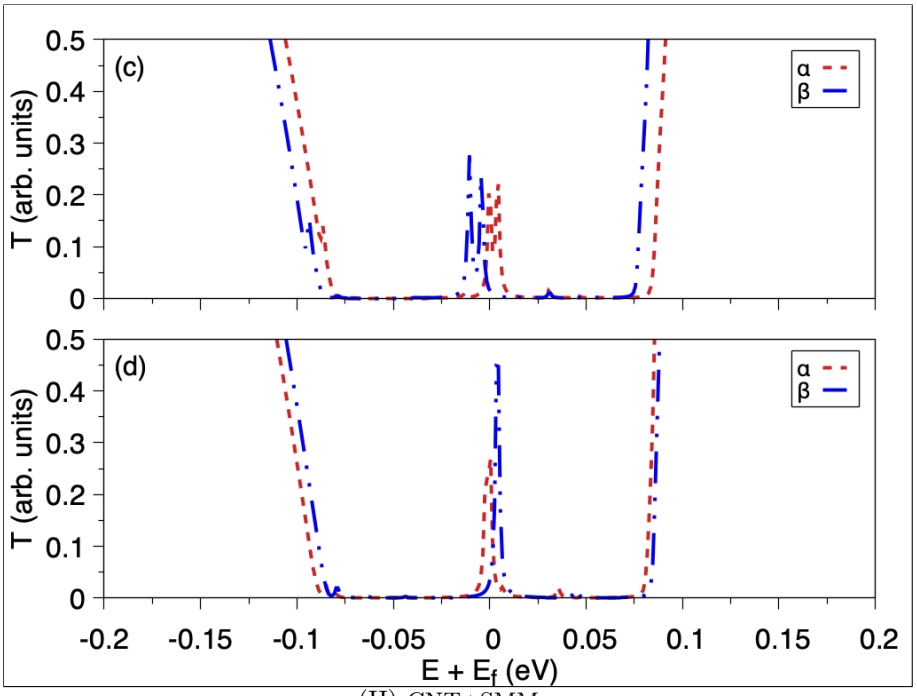

(II) CNT+SMMs

Figure 4.38.: Transmission coefficient per spin for the FE-AF (upper row) as well as for the FE-FE (lower row) case. At $E + E_f = 0$ the transmission peaks for alpha and beta overlap in the case of FE-FE alignment. In the FE-AF case, only the beta transmission is present. $V_g = 0.129$ V

Figure 4.38 shows a comparison between the transmission coefficient at the degeneracy points for the CNT+SMMs system as well as for the empirical model for both spin channels. It is obvious that the overlapping of the alpha and beta transmission peaks at $E + E_f = 0$ define the total

transmission and hence, the total conductance at the Fermi window. In the case of the empirical system, the behaviour is not exclusive of the region around the Fermi energy, but it is repeated in other energy regions of the spectra like in $E + E_f = (-0.17, -0.05)$ eV (i.e. at the edge of the valence band). This effect is clearly a consequence of the extra poles appearing inside of the band gap (see figure 4.35) in the FE-FE case.

The spin-valve mechanism observed in the experimental, as well as in the simulations is therefore a consequence of the hybridization of the energy levels between the tube and the magnets. These energy levels are equally occupied by the spin up and spin down electrons in the case of the non-zero external magnetic field (B) and the parallel alignment (FE-FE) in the experiments and simulations respectively. The influence of these energy levels on the valence / conductance bands as well as in the band gap is the same. The total transmission will be the overlap of the alpha and beta channels which is non-zero for the degeneracy points (the regions in the contour plots where $G \neq 0$).

In the case where $B = 0$ and the antiparallel case (experiment / simulations), the hybridized energy levels for the alpha and beta channels reorganize differently. The reason for this, is that the extra electron in the ligands is oriented randomly, therefore occupying different energy levels for both spin channels. The total transmission at some of the degeneracy points will not have the contribution of the alpha and beta transmissions, but rather just one of them, resulting on a lower total transmission with respect to the parallel case.

Finally, since the conductance is proportional to the transmission coefficient, the larger the total transmission around the Fermi window, the larger the conductance value will be. All these observations are in accordance with the observed patterns in the experiments and simulations.

5. Conclusions and Outlook

In this thesis, the problem of magnetoresistance in carbon nanotubes decorated with single molecule magnets was adressed. In order to model such highly correlated systems, one first has to establish a suitable level of theory which fulfills several criteria: first of all, the electronic as well as magnetic properties of single molecule magnets have to resemble those observed in experiments. This procedure has to be both reliable and not as expensive as other methods used to simulate SMMs (e.g. CASSCF, DFT with spin-orbit coupling or even DFT with hybrid functionals). Third, it has to provide useful input for post-DFT methods which can be used in the calculation of electronic transport through nanosystems. With this in mind, a new framework which consisted in a constrained DFT plus NEGF was explored.

In an initial approach, the CDFT method was used and compared to standard DFT in the simulation of SMMs in various phases and arrengements. It was proven that with the correct choise of parameters, CDFT overcomes some of the problems observed in DFT for systems with several electrons in open shell systems. For example, the spin localization was almost completely lost in some of the DFT calculations, meanwhile the constraints depicted both graphically and numerically the correct charge and magnetization of the magnets. A suitable carbon nanotube which resembles the experimental ones was chosen based on two parameters: the bandgap and the size in terms of the basis set. To this end, a semi-metallic tube with chirality (9, 0) was found to be the best candidate to build the CNTFET.

Computational resources are not much higher than those of regular spin polarized DFT, allowing us to simulate large periodic systems with highly correlated atoms (like terbium or lanthanides in general) with a sensible amount of resources. The advantages of using a method like CDFT is that we can control the total number of unpaired electrons per spin channel as well as their orientation and retain their magnetization with negligable spin contamination. This allowed us to simulate different spin states (one where the coupling between the terbium electrons and the phthalocyanines' delocalized electron was antiferromagnetic and a second state where the coupling was ferromagnetic) which resemble the system under different applied external magnetic field. Therefore, without the explicit introduction of a magnetic field, we got and insight of the phenomena that reproduces the spin-valve mechanism.

First of all, for the simulation of small bandgap CNTs, one needs good convergence of the results with respect to the basis sets. In this sense, to get rid of spurious states in the CNT spectra, a

short range basis set has to be used (of course a small basis set would work but then the accuracy of the calculation is compromised).
It was also shown that if one does not impose the constraints on the complete system (CNT + SMMs), artificial phenomena occurs like the schrinking of the bandgap, charge transfer and shift of the spin polarized DOS / transmission spectra with respect to each of the spin polarizations. This is important since the the spin-valve mechanism is increased or decreased with the size of the CNT bandgap.
The spin-valve mechanism was observed for the system composed of a (9, 0) CNT on top of which two $TbPc_2$ were deposited. For a parallel alignment of the ligands' spins of both SMMs, the conductance shows larger values for all Coulomb diamonds compared to the antiparallel alignment. The reason is that the energy levels of the composite system rearrenge differently for both spin configurations. In the ferromagnetic case the transmission for the alpha and beta channels overlap while in the antiferromagnetic they are separated. The total transmission, which is the sum of both spin channels is therefore larger for the ferromagnetic case. This makes the value of the current and the differential conductance by means of the Landauer Formula get higher contributions for the parallel alignment and thus, magnetoresistance appears. The giant magnetoresistance ratio was calculated to be (for some of the peaks), of the order of $\sim 300\%$, which is surprisingly close to the original experimental values. These observations were corroborated by the empirical model provided.
It is important to notice that, the Green's function used in this work does not comprises electron-electron interactions. If one would like to consider such types of interactions, an extra Coulomb term (U) in the single particle Hamiltonian must be taken into account. Then, one would have to make use of the equation-of-motion method to obtain an interacting Green's function which will give the corrections to the energy levels of the full system. The rest of the procedure described on this thesis would still be valid and thus, an extension to the presented results could be provided.
We want to stress, that the present workflow it's not exclusive of these single molecule magnets or even for such a substrate (CNT). In terms of the NEGF, any periodic system which presents a block-wise tri-diagonal structure can be modelled. With regards of the CDFT, systems with (at least in principle) any type of atoms with magnetic properties, presenting high correlations can be constrained to simulate the specific electronic state. It does not matter if this is not a ground state.

A. Explicit matrix form of the empirical Hamiltonian for the Spin valve

$$\mathbf{H}_C^{\alpha} = \begin{bmatrix}
E^1_{\alpha,1} & 0 & 0 & 0 & \tau^{12}_{\alpha,11} & 0 & 0 & 0 & t^{13}_{\alpha,11} & 0 & 0 & 0 & 0 & 0 & 0 & 0 \\
0 & 0 & 0 & 0 & 0 & 0 & 0 & 0 & 0 & 0 & 0 & 0 & 0 & 0 & 0 & 0 \\
0 & 0 & E^1_{\alpha,2} & 0 & 0 & 0 & \tau^{12}_{\alpha,22} & 0 & 0 & 0 & t^{13}_{\alpha,22} & 0 & 0 & 0 & 0 & 0 \\
0 & 0 & 0 & 0 & 0 & 0 & 0 & 0 & 0 & 0 & 0 & 0 & 0 & 0 & 0 & 0 \\
\tau^{21}_{\alpha,11} & 0 & 0 & 0 & E^2_{\alpha,1} & 0 & 0 & 0 & 0 & 0 & 0 & 0 & t^{24}_{\alpha,11} & 0 & 0 & 0 \\
0 & 0 & 0 & 0 & 0 & 0 & 0 & 0 & 0 & 0 & 0 & 0 & 0 & 0 & 0 & 0 \\
0 & 0 & \tau^{21}_{\alpha,22} & 0 & 0 & 0 & E^2_{\alpha,2} & 0 & 0 & 0 & 0 & 0 & 0 & 0 & t^{24}_{\alpha,22} & 0 \\
0 & 0 & 0 & 0 & 0 & 0 & 0 & 0 & 0 & 0 & 0 & 0 & 0 & 0 & 0 & 0 \\
t^{31}_{\alpha,11} & 0 & 0 & 0 & 0 & 0 & 0 & 0 & \epsilon^3_{\alpha,1} & 0 & 0 & 0 & 0 & 0 & 0 & 0 \\
0 & 0 & 0 & 0 & 0 & 0 & 0 & 0 & 0 & 0 & 0 & 0 & 0 & 0 & 0 & 0 \\
0 & 0 & t^{31}_{\alpha,22} & 0 & 0 & 0 & 0 & 0 & 0 & 0 & \epsilon^3_{\alpha,2} & 0 & 0 & 0 & 0 & 0 \\
0 & 0 & 0 & 0 & 0 & 0 & 0 & 0 & 0 & 0 & 0 & 0 & 0 & 0 & 0 & 0 \\
0 & 0 & 0 & 0 & t^{42}_{\alpha,11} & 0 & 0 & 0 & 0 & 0 & 0 & 0 & \epsilon^4_{\alpha,1} & 0 & 0 & 0 \\
0 & 0 & 0 & 0 & 0 & 0 & 0 & 0 & 0 & 0 & 0 & 0 & 0 & 0 & 0 & 0 \\
0 & 0 & 0 & 0 & 0 & 0 & t^{42}_{\alpha,22} & 0 & 0 & 0 & 0 & 0 & 0 & 0 & \epsilon^4_{\alpha,2} & 0 \\
0 & 0 & 0 & 0 & 0 & 0 & 0 & 0 & 0 & 0 & 0 & 0 & 0 & 0 & 0 & 0
\end{bmatrix} \tag{A.1}$$

$$\mathbf{H}_C^{\beta} = \begin{bmatrix}
0 & 0 & 0 & 0 & 0 & 0 & 0 & 0 & 0 & 0 & 0 & 0 & 0 & 0 & 0 & 0 \\
0 & E^1_{\beta,1} & 0 & 0 & 0 & \tau^{12}_{\beta,11} & 0 & 0 & 0 & t^{13}_{\beta,11} & 0 & 0 & 0 & 0 & 0 & 0 \\
0 & 0 & 0 & 0 & 0 & 0 & 0 & 0 & 0 & 0 & 0 & 0 & 0 & 0 & 0 & 0 \\
0 & 0 & 0 & E^1_{\beta,2} & 0 & 0 & 0 & \tau^{12}_{\beta,22} & 0 & 0 & 0 & t^{13}_{\beta,22} & 0 & 0 & 0 & 0 \\
0 & 0 & 0 & 0 & 0 & 0 & 0 & 0 & 0 & 0 & 0 & 0 & 0 & 0 & 0 & 0 \\
0 & \tau^{21}_{\beta,11} & 0 & 0 & 0 & E^2_{\beta,1} & 0 & 0 & 0 & 0 & 0 & 0 & 0 & t^{24}_{\beta,11} & 0 & 0 \\
0 & 0 & 0 & 0 & 0 & 0 & 0 & 0 & 0 & 0 & 0 & 0 & 0 & 0 & 0 & 0 \\
0 & 0 & 0 & \tau^{21}_{\beta,22} & 0 & 0 & 0 & E^2_{\beta,2} & 0 & 0 & 0 & 0 & 0 & 0 & 0 & t^{24}_{\beta,22} \\
0 & 0 & 0 & 0 & 0 & 0 & 0 & 0 & 0 & 0 & 0 & 0 & 0 & 0 & 0 & 0 \\
0 & t^{31}_{\beta,11} & 0 & 0 & 0 & 0 & 0 & 0 & 0 & \epsilon^3_{\beta,1} & 0 & 0 & 0 & 0 & 0 & 0 \\
0 & 0 & 0 & 0 & 0 & 0 & 0 & 0 & 0 & 0 & 0 & 0 & 0 & 0 & 0 & 0 \\
0 & 0 & 0 & t^{31}_{\beta,22} & 0 & 0 & 0 & 0 & 0 & 0 & 0 & \epsilon^3_{\beta,2} & 0 & 0 & 0 & 0 \\
0 & 0 & 0 & 0 & 0 & 0 & 0 & 0 & 0 & 0 & 0 & 0 & 0 & 0 & 0 & 0 \\
0 & 0 & 0 & 0 & 0 & t^{42}_{\beta,11} & 0 & 0 & 0 & 0 & 0 & 0 & 0 & \epsilon^4_{\beta,1} & 0 & 0 \\
0 & 0 & 0 & 0 & 0 & 0 & 0 & 0 & 0 & 0 & 0 & 0 & 0 & 0 & 0 & 0 \\
0 & 0 & 0 & 0 & 0 & 0 & 0 & t^{42}_{\beta,22} & 0 & 0 & 0 & 0 & 0 & 0 & 0 & \epsilon^4_{\beta,2}
\end{bmatrix} \tag{A.2}$$

$$\mathbf{H}_L^{\alpha} = \begin{bmatrix}
E^1_{\alpha,1} & 0 & 0 & 0 & \tau^{12}_{\alpha,11} & 0 & 0 & 0 \\
0 & 0 & 0 & 0 & 0 & 0 & 0 & 0 \\
0 & 0 & E^1_{\alpha,2} & 0 & 0 & 0 & \tau^{12}_{\alpha,22} & 0 \\
0 & 0 & 0 & 0 & 0 & 0 & 0 & 0 \\
\tau^{21}_{\alpha,11} & 0 & 0 & 0 & E^2_{\alpha,1} & 0 & 0 & 0 \\
0 & 0 & 0 & 0 & 0 & 0 & 0 & 0 \\
0 & 0 & \tau^{21}_{\alpha,22} & 0 & 0 & 0 & E^2_{\alpha,2} & 0 \\
0 & 0 & 0 & 0 & 0 & 0 & 0 & 0
\end{bmatrix} \tag{A.3}$$

$$\mathbf{H}_L^{\beta} = \begin{bmatrix} 0 & 0 & 0 & 0 & 0 & 0 & 0 & 0 \\ 0 & E^1_{\beta,1} & 0 & 0 & 0 & \tau^{12}_{\beta,11} & 0 & 0 \\ 0 & 0 & 0 & 0 & 0 & 0 & 0 & 0 \\ 0 & 0 & 0 & E^1_{\beta,2} & 0 & 0 & 0 & \tau^{12}_{\beta,22} \\ 0 & 0 & 0 & 0 & 0 & 0 & 0 & 0 \\ 0 & \tau^{21}_{\beta,11} & 0 & 0 & 0 & E^2_{\beta,1} & 0 & 0 \\ 0 & 0 & 0 & 0 & 0 & 0 & 0 & 0 \\ 0 & 0 & 0 & \tau^{21}_{\beta,22} & 0 & 0 & 0 & E^2_{\beta,2} \end{bmatrix} \tag{A.4}$$

$$\mathbf{H}_R^{\alpha} = \begin{bmatrix} E^1_{\alpha,1} & 0 & 0 & 0 & \tau^{12}_{\alpha,11} & 0 & 0 & 0 \\ 0 & 0 & 0 & 0 & 0 & 0 & 0 & 0 \\ 0 & 0 & E^1_{\alpha,2} & 0 & 0 & 0 & \tau^{12}_{\alpha,22} & 0 \\ 0 & 0 & 0 & 0 & 0 & 0 & 0 & 0 \\ \tau^{21}_{\alpha,11} & 0 & 0 & 0 & E^2_{\alpha,1} & 0 & 0 & 0 \\ 0 & 0 & 0 & 0 & 0 & 0 & 0 & 0 \\ 0 & 0 & \tau^{21}_{\alpha,22} & 0 & 0 & 0 & E^2_{\alpha,2} & 0 \\ 0 & 0 & 0 & 0 & 0 & 0 & 0 & 0 \end{bmatrix} \tag{A.5}$$

$$\mathbf{H}_R^{\beta} = \begin{bmatrix} 0 & 0 & 0 & 0 & 0 & 0 & 0 & 0 \\ 0 & E^1_{\beta,1} & 0 & 0 & 0 & \tau^{12}_{\beta,11} & 0 & 0 \\ 0 & 0 & 0 & 0 & 0 & 0 & 0 & 0 \\ 0 & 0 & 0 & E^1_{\beta,2} & 0 & 0 & 0 & \tau^{12}_{\beta,22} \\ 0 & 0 & 0 & 0 & 0 & 0 & 0 & 0 \\ 0 & \tau^{21}_{\beta,11} & 0 & 0 & 0 & E^2_{\beta,1} & 0 & 0 \\ 0 & 0 & 0 & 0 & 0 & 0 & 0 & 0 \\ 0 & 0 & 0 & \tau^{21}_{\beta,22} & 0 & 0 & 0 & E^2_{\beta,2} \end{bmatrix} \tag{A.6}$$

For the coupling matrices between the left and the central region we denote the atom numbers of the left lead with a primed variable

$$\mathbf{V}^{\dagger}_{\alpha,LC} = \begin{bmatrix} 0 & 0 & 0 & 0 & v^{12'}_{\alpha\alpha,11} & 0 & 0 & 0 \\ 0 & 0 & 0 & 0 & 0 & 0 & 0 & 0 \\ 0 & 0 & 0 & 0 & 0 & 0 & v^{12'}_{\alpha\alpha,22} & 0 \\ 0 & 0 & 0 & 0 & 0 & 0 & 0 & 0 \\ 0 & 0 & 0 & 0 & 0 & 0 & 0 & 0 \\ 0 & 0 & 0 & 0 & 0 & 0 & 0 & 0 \\ 0 & 0 & 0 & 0 & 0 & 0 & 0 & 0 \\ 0 & 0 & 0 & 0 & 0 & 0 & 0 & 0 \\ 0 & 0 & 0 & 0 & 0 & 0 & 0 & 0 \\ 0 & 0 & 0 & 0 & 0 & 0 & 0 & 0 \\ 0 & 0 & 0 & 0 & 0 & 0 & 0 & 0 \\ 0 & 0 & 0 & 0 & 0 & 0 & 0 & 0 \\ 0 & 0 & 0 & 0 & 0 & 0 & 0 & 0 \\ 0 & 0 & 0 & 0 & 0 & 0 & 0 & 0 \end{bmatrix} \tag{A.7}$$

$$\mathbf{V}^{\dagger}_{\beta,LC} = \begin{bmatrix} 0 & 0 & 0 & 0 & 0 & 0 & 0 & 0 \\ 0 & 0 & 0 & 0 & 0 & v^{12'}_{\beta\beta,11} & 0 & 0 \\ 0 & 0 & 0 & 0 & 0 & 0 & 0 & 0 \\ 0 & 0 & 0 & 0 & 0 & 0 & 0 & v^{12'}_{\beta\beta,22} \\ 0 & 0 & 0 & 0 & 0 & 0 & 0 & 0 \\ 0 & 0 & 0 & 0 & 0 & 0 & 0 & 0 \\ 0 & 0 & 0 & 0 & 0 & 0 & 0 & 0 \\ 0 & 0 & 0 & 0 & 0 & 0 & 0 & 0 \\ 0 & 0 & 0 & 0 & 0 & 0 & 0 & 0 \\ 0 & 0 & 0 & 0 & 0 & 0 & 0 & 0 \\ 0 & 0 & 0 & 0 & 0 & 0 & 0 & 0 \\ 0 & 0 & 0 & 0 & 0 & 0 & 0 & 0 \\ 0 & 0 & 0 & 0 & 0 & 0 & 0 & 0 \\ 0 & 0 & 0 & 0 & 0 & 0 & 0 & 0 \\ 0 & 0 & 0 & 0 & 0 & 0 & 0 & 0 \end{bmatrix} \tag{A.8}$$

B. Parameters for some of the figures in the thesis

State	$\epsilon^3_{\alpha,1}$	$\epsilon^3_{\alpha,2}$	$\epsilon^3_{\beta,1}$	$\epsilon^3_{\beta,2}$	$\epsilon^4_{\alpha,1}$	$\epsilon^4_{\alpha,2}$	$\epsilon^4_{\beta,1}$	$\epsilon^4_{\beta,2}$	$E^1_{\alpha,1}$	$E^1_{\alpha,2}$	$E^1_{\beta,1}$	$E^1_{\beta,2}$	$E^2_{\alpha,1}$	$E^2_{\alpha,2}$	$E^2_{\beta,1}$	$E^2_{\beta,2}$
FE-AF	-0.17	0.3	-0.17	0.3	0.1	0.3	-0.17	0.3	-0.26	0.26	-0.26	0.26	-0.26	0.26	-0.26	0.26
FE-FE	-0.17	0.3	-0.17	0.3	-0.17	0.3	-0.17	0.3	-0.26	0.26	-0.26	0.26	-0.26	0.26	-0.26	0.26

Table B.1.: On-site energies in the central system for the empirical model.

State	$t^{13}_{\alpha,1}$	$t^{13}_{\beta,1}$	$t^{13}_{\alpha,2}$	$t^{13}_{\beta,2}$	$t^{24}_{\alpha,1}$	$t^{24}_{\beta,1}$	$t^{24}_{\alpha,2}$	$t^{24}_{\beta,2}$	τ_α	τ_β	v_α	v_β	δ_α	δ_β
FE-AF	0.0	0.0	0.0	0.0	0.0	0.0	0.0	0.0	0.1	0.1	0.1	0.1	0.1	0.1
FE-FE	0.0	0.0	0.0	0.0	0.0	0.0	0.0	0.0	0.1	0.1	0.1	0.1	0.1	0.1

Table B.2.: Different coupling terms for the empirical model.

State	$t^{13}_{\alpha,1}$	$t^{13}_{\beta,1}$	$t^{13}_{\alpha,2}$	$t^{13}_{\beta,2}$	$t^{24}_{\alpha,1}$	$t^{24}_{\beta,1}$	$t^{24}_{\alpha,2}$	$t^{24}_{\beta,2}$	τ_α	τ_β	v_α	v_β	δ_α	δ_β
FE-AF	0.1	0.0	0.0	0.0	0.1	0.0	0.0	0.0	0.1	0.1	0.1	0.1	0.1	0.1
FE-FE	0.0	0.0	0.0	0.0	0.0	0.0	0.0	0.0	0.1	0.1	0.1	0.1	0.1	0.1

Table B.3.: Different coupling terms for the empirical model. $t^{13}_{\alpha\alpha,11} = t^{24}_{\alpha\alpha,11} = 0.1$

State	$t^{13}_{\alpha,1}$	$t^{13}_{\beta,1}$	$t^{13}_{\alpha,2}$	$t^{13}_{\beta,2}$	$t^{24}_{\alpha,1}$	$t^{24}_{\beta,1}$	$t^{24}_{\alpha,2}$	$t^{24}_{\beta,2}$	τ_α	τ_β	v_α	v_β	δ_α	δ_β
FE-AF	0.1	0.0	0.1	0.0	0.1	0.0	0.1	0.0	0.1	0.1	0.1	0.1	0.1	0.1
FE-FE	0.1	0.0	0.1	0.0	0.1	0.0	0.1	0.0	0.1	0.1	0.1	0.1	0.1	0.1

Table B.4.: Different coupling terms for the empirical model. $t^{13}_{\alpha\alpha,11} = t^{24}_{\alpha\alpha,11} = t^{13}_{\alpha\alpha,22} = t^{24}_{\alpha\alpha,22} = 0.1$

State	$t^{13}_{\alpha,1}$	$t^{13}_{\beta,1}$	$t^{13}_{\alpha,2}$	$t^{13}_{\beta,2}$	$t^{24}_{\alpha,1}$	$t^{24}_{\beta,1}$	$t^{24}_{\alpha,2}$	$t^{24}_{\beta,2}$	τ_α	τ_β	v_α	v_β	δ_α	δ_β
FE-AF	0.175	0.175	0.175	0.175	0.175	0.175	0.175	0.175	0.1	0.1	0.1	0.1	0.1	0.1
FE-FE	0.175	0.175	0.175	0.175	0.175	0.175	0.175	0.175	0.1	0.1	0.1	0.1	0.1	0.1

Table B.5.: Different coupling terms for the empirical model. $t^{13}_{\alpha\alpha,11} = t^{24}_{\alpha\alpha,11} = t^{13}_{\alpha\alpha,22} = t^{24}_{\alpha\alpha,22} = 0.175$

C. List of publications

Parts of this work have been published or are currently submitted in international journals.

Jonas Armleder, Timo Strunk, Franz Symalla, Pascal Friederich, Jorge Enrique Olivares Peña, Tobias Neumann, Wolfgang Wenzel, and Artem Fediai. Computing charging and polarization energies of small organic molecules embedded into amorphous materials with quantum accuracy. *Journal of Chemical Theory and Computation*, 17(6):3727–3738, 2021. PMID: 34038113.

Athanassios K. Boudalis, Jorge-Enrique Olivares-Peña, Eufemio Moreno-Pineda, Artem Fediai, Wolfgang Wenzel, Philippe Turek, and Mario Ruben. Room-temperature spin nutations in a magnetically condensed phase of [y(pc)2]$^{\cdot}$. *Chem. Commun.*, 57:11505–11508, 2021.

Jorge-Enrique Olivares-Peña, Ali Deniz Özdemir, Wenzel Wolfgang, and Artem Fediai. Explaining and amplifying the spin valve effect in supramolecular systems. *Physical Review Materials*, 2022. Submitted and in revision.

Nithin Suryadevara, Athanassios K. Boudalis, Jorge-Enrique Olivares-Peña, Eufemio Moreno-Pineda, Artem Fediai, Wolfgang Wenzel, Philippe Turek, and Mario Ruben. Molecular engineering of supramolecular spin qubits. 2022.

D. List of Figures

E. List of Tables

Acknowledgments

Trotzdem Deutsch nicht meine Muttersprache ist, Deutschland hat mir die wunderbare Möglichkeit Hochausbilding zu erreichen. Deswegen, bedanke ich mich hier auf die Sprache der Denker.
Erstmals, ich danke Gott, Ich glaube Du irgendwo, irgendwie dabei bist und hast das Universum die Chance zu existieren gegeben.
Zweitens, ich bedanke mich **Prof. Dr. Wolfgang Wenzel**, von ganzem Herzen, für die Möglichkeit in Seiner Forschungsgruppe zu arbeiten. Ich werde immer Ihnen etwas schulden.
Prof. Dr. Garst Markus, ich danke Ihnen für die Zeit um diese Arbeit zu lesen und für Ihre hilfreiche Kommentare.
Dr. Artem Fediai, es gibt nicht genugende Wörter um auszudrücken, wie viel hast Du mich gelernt: zu denken, meiner Gedanken zu strukturieren, Qualität zu fordern, Arbeitsmoral immer vor, schnell zu arbeiten... Ich schulde Dir meiner Arbeitszukunft. Danke. Dyakuyu.
Zu meiner Familie: Sie waren da, wann die Umstände extrem schwierig waren, wann mein Pfad nicht klar war, wann die Arbeit, Sport, Büchern oder Hobbies nicht mehr reichten, sie waren da für mich.
Padre: Siempre creíste en mi, siempre me apoyaste. Eres duro, pero justo. Fuiste, eres y serás siempre mi héroe. No existe mejor hombre que tú. Gracias.
Madre: Gracias por tu apoyo infinito y tomarme en tus brazos cuando lo he necesitado. Por hacerme creer que soy especial. Gracias.
Yorch: Hermano, hemos ido a veces separados, a veces juntos caminando por la vida; pero ha sido una hermosa caminata contigo. Gracias por todo.
Nanzol: Estuviste ahí, en los tiempos más obscuros de mi vida, me hablaste y calmaste, sufriste conmigo, y creśte en mi. Núnca lo voy a olvidar. Gracias.
Tonicol: Siempre has sido uno de los pocos motivos por los que sigo aquí, por lo que he hecho lo que he hecho. Como ya lo sabes: siempre voy a estar para ti.
Ein Mann kann sich nur durch seiner Freunde richtig kennen, und deshalb, ein paar Wörter für Euch alle:
Christoph: *Wir sind zwei Jungs, aus verschiedene Länder, mit fremder Sprachen, mit verschiedene Hintergründen und trotz, wir haben diesselbe Prinzipien, diesselbe Gedanken.* Du sagtest mir. Und wie immer, Du hast total recht! Besser Freund könnte nicht geben. Danke.
Iván: Tantos años, y sigues siendo parte fundamental de mi vida. Te lo dije una vez y lo diré hasta el final: siempre serás mi amigo. Gracias.

Marjan: We went through hell together, and you were a friend always available to talk with. I will never forget those days were I didn't feel so lonely because of your company. Hvala.
Johannes: Irgenwie, du hast du da geblieben, ein Mann mit Genetik befreundet mit einem ohne Genetik, aber gehen wir immer vorwärts und zusammen. Danke.
Clemens: Kumpel, ich hoffe du irgendwann verstehest, was bedeutet ein Mann zu sein. Du hast den Wille, jetzt, Los geht's! Wenn du mir brauchst, bin ich dabei. Danke.
Montse: Compañeros de oficina, y después amigos. Eres una buena persona, y eso es lo más valioso que puedes tener. Me da gusto saber que tengo una amiga como tú. Gracias.
Letztendlich, ich danke euch alle, die irgendwie ich in meinem Pfad getroffen habe und etwas hochwertige mir gelernt haben: Tenopala, Prof. Licona, Sandra, Karen... Juan.

Ohne Angst, ohne Ausreden, ohne Genetik...

F. Bibliography

[1] R. Lloyd Carroll and Christopher B. Gorman. The genesis of molecular electronics. *Angewandte Chemie International Edition*, 41(23):4378–4400, 2002.

[2] Arieh Aviram and Mark A. Ratner. Molecular rectifiers. *Chemical Physics Letters*, 29(2):277–283, 1974.

[3] Robert M. Metzger, Bo Chen, Ulf Höpfner, M. V. Lakshmikantham, Dominique Vuillaume, Tsuyoshi Kawai, Xiangli Wu, Hiroaki Tachibana, Terry V. Hughes, Hiromi Sakurai, Jeffrey W. Baldwin, Christina Hosch, Michael P. Cava, Ludwig Brehmer, and Geoffrey J. Ashwell. Unimolecular electrical rectification in hexadecylquinolinium tricyanoquinodimethanide. *Journal of the American Chemical Society*, 119(43):10455–10466, 1997.

[4] *Introducing Molecular Electronics*. Lecture Notes in Physics. Springer-Verlag Berlin Heidelberg, 2005.

[5] D. M. Eigler, C. P. Lutz, and W. E. Rudge. An atomic switch realized with the scanning tunnelling microscope. *Nature*, 352(6336):600–603, 1991.

[6] M. A. Reed, C. Zhou, C. J. Muller, T. P. Burgin, and J. M. Tour. Conductance of a molecular junction. *Science*, 278(5336):252–254, 1997.

[7] Mark Johnson and R. H. Silsbee. Interfacial charge-spin coupling: Injection and detection of spin magnetization in metals. *Phys. Rev. Lett.*, 55:1790–1793, Oct 1985.

[8] M. N. Baibich, J. M. Broto, A. Fert, F. Nguyen Van Dau, F. Petroff, P. Etienne, G. Creuzet, A. Friederich, and J. Chazelas. Giant magnetoresistance of (001)fe/(001)cr magnetic superlattices. *Phys. Rev. Lett.*, 61:2472–2475, Nov 1988.

[9] M. Di Ventra. *Electrical Transport in Nanoscale Systems*. Cambridge University Press, 2008.

[10] S. Datta. *Electronic Transport in Mesoscopic Systems*. Cambridge Studies in Semiconductor Physics and Microelectronic Engineering. Cambridge University Press, 1997.

[11] Jørgen Rammer. Quantum transport theory of electrons in solids: A single-particle approach. *Rev. Mod. Phys.*, 63:781–817, Oct 1991.

[12] Edward A. Laird, Ferdinand Kuemmeth, Gary A. Steele, Kasper Grove-Rasmussen, Jesper Nygård, Karsten Flensberg, and Leo P. Kouwenhoven. Quantum transport in carbon nanotubes. *Rev. Mod. Phys.*, 87:703–764, Jul 2015.

[13] Alois Roman Dirnaichner. *Charge and spin transport in carbon nanotubes: From Coulomb blockade to Fabry-Perot interface.* PhD thesis, Universität Regensburg, 4 2016.

[14] Jean-Christophe Charlier, Xavier Blase, and Stephan Roche. Electronic and transport properties of nanotubes. *Rev. Mod. Phys.*, 79:677–732, May 2007.

[15] Zhaohui Zhong, Nathaniel M. Gabor, Jay E. Sharping, Alexander L. Gaeta, and Paul L. McEuen. Terahertz time-domain measurement of ballistic electron resonance in a single-walled carbon nanotube. *Nature Nanotechnology*, 3:201–205, Apr 2008.

[16] Xinjian Zhou, Ji-Yong Park, Shaoming Huang, Jie Liu, and Paul L. McEuen. Band structure, phonon scattering, and the performance limit of single-walled carbon nanotube transistors. *Phys. Rev. Lett.*, 95:146805, Sep 2005.

[17] S. Datta and Cambridge University Press. *Quantum Transport: Atom to Transistor.* Cambridge University Press, 2005.

[18] S.M. Sze and K.K. Ng. *Physics of Semiconductor Devices.* Wiley, 2006.

[19] Calvin R. King, Jr. Density of states: 2d, 1d, and 0d. Website, December 2005. Online erhältlich unter `https://alan.ece.gatech.edu/ECE6451/Lectures/StudentLectures/King_Notes_Density_of_States_2D1D0D.pdf`; abgerufen am 1. November 2021.

[20] Eleftherios N. Economou. *Green's Functions in Quantum Physics.* Springer Series in Solid-State Sciences. Springer-Verlag Berlin Heidelberg, 2006.

[21] D. Ryndyk. *Theory of Quantum Transport at Nanoscale: An Introduction.* Springer Series in Solid-State Sciences. Springer International Publishing, 2015.

[22] Wikipedia. Delta-distribution. Website, Juni 2021. Online erhältlich unter `https://de.wikipedia.org/wiki/Delta-Distribution`; abgerufen am 10. November 2021.

[23] Magnus Paulsson. Non equilibrium green's functions for dummies: Introduction to the one particle negf equations. *arXiv*, -, Feb 2008.

[24] Reiner M. Dreizler and Eberhard K.U. Gross. *Density Functional Theory.* Springer-Verlag Berlin Heidelberg, 1990.

[25] W. Koch and M.C. Holthausen. *A Chemist's Guide to Density Functional Theory.* Wiley, 2015.

[26] C. Ullrich. *Time-Dependent Density-Functional Theory: Concepts and Applications*. Oxford Graduate Texts. OUP Oxford, 2012.

[27] P. Hohenberg and W. Kohn. Inhomogeneous electron gas. *Phys. Rev.*, 136:B864–B871, Nov 1964.

[28] Christoph R. Jacob and Markus Reiher. Spin in density-functional theory. *International Journal of Quantum Chemistry*, 112(23):3661–3684, 2012.

[29] P. H. Dederichs, S. Blügel, R. Zeller, and H. Akai. Ground states of constrained systems: Application to cerium impurities. *Phys. Rev. Lett.*, 53:2512–2515, Dec 1984.

[30] Benjamin Kaduk, Tim Kowalczyk, and Troy Van Voorhis. Constrained density functional theory. *Chemical Reviews*, 112(1):321–370, 2012. PMID: 22077560.

[31] Sander J. Tans, Alwin R. M. Verschueren, and Cees Dekker. Room-temperature transistor based on a single carbon nanotube. *Nature*, 393, 1998.

[32] Adrian Bachtold, Peter Hadley, Takeshi Nakanishi, and Cees Dekker. Logic circuits with carbon nanotube transistors. *Science*, 294(5545):1317–1320, 2001.

[33] Vinod K. Sangwan, Rocio Ponce Ortiz, Justice M. P. Alaboson, Jonathan D. Emery, Michael J. Bedzyk, Lincoln J. Lauhon, Tobin J. Marks, and Mark C. Hersam. Fundamental performance limits of carbon nanotube thin-film transistors achieved using hybrid molecular dielectrics. *ACS Nano*, 6(8):7480–7488, 2012. PMID: 22783918.

[34] M. Urdampilleta, S. Klyatskaya, J-P. Cleuziou, M. Ruben, and W. Wernsdorfer. Supramolecular spin valves. *Nature Materials*, 10:502–506, 2011.

[35] Thomas D. Kühne, Marcella Iannuzzi, Mauro Del Ben, Vladimir V. Rybkin, Patrick Seewald, Frederick Stein, Teodoro Laino, Rustam Z. Khaliullin, Ole Schütt, Florian Schiffmann, Dorothea Golze, Jan Wilhelm, Sergey Chulkov, Mohammad Hossein Bani-Hashemian, Valéry Weber, Urban Borštnik, Mathieu Taillefumier, Alice Shoshana Jakobovits, Alfio Lazzaro, Hans Pabst, Tiziano Müller, Robert Schade, Manuel Guidon, Samuel Andermatt, Nico Holmberg, Gregory K. Schenter, Anna Hehn, Augustin Bussy, Fabian Belleflamme, Gloria Tabacchi, Andreas Glöß, Michael Lass, Iain Bethune, Christopher J. Mundy, Christian Plessl, Matt Watkins, Joost VandeVondele, Matthias Krack, and Jürg Hutter. Cp2k: An electronic structure and molecular dynamics software package - quickstep: Efficient and accurate electronic structure calculations. *The Journal of Chemical Physics*, 152(19):194103, 2020.

[36] M P Lopez Sancho, J M Lopez Sancho, J M L Sancho, and J Rubio. Highly convergent schemes for the calculation of bulk and surface green functions. *Journal of Physics F: Metal Physics*, 15(4):851–858, apr 1985.

[37] Wikipedia. Delta-distribution. Website, October 2021. Online erhältlich unter `https://en.wikipedia.org/wiki/Gaussian_function`; abgerufen am 17. December 2021.

[38] L. J. de Jongh. Experiments on simple magnetic model systems. *Journal of Applied Physics*, 49(3):1305–1310, 1978.

[39] Athanassios K. Boudalis, Jorge-Enrique Olivares-Peña, Eufemio Moreno-Pineda, Artem Fediai, Wolfgang Wenzel, Philippe Turek, and Mario Ruben. Room-temperature spin nutations in a magnetically condensed phase of [y(pc)2]˙. *Chem. Commun.*, 57:11505–11508, 2021.

[40] F. Branzoli, P. Carretta, M. Filibian, S. Klyatskaya, and M. Ruben. Low-energy spin dynamics in the $[ypc_2]^0$ $s = \frac{1}{2}$ antiferromagnetic chain. *Phys. Rev. B*, 83:174419, May 2011.

[41] Andrei V. Postnikov, Jens Kortus, and Mark R. Pederson. Density functional studies of molecular magnets. *physica status solidi (b)*, 243(11):2533–2572, 2006.

[42] Naoto Ishikawa, Miki Sugita, Tadahiko Ishikawa, Shin-ya Koshihara, and Youkoh Kaizu. Lanthanide double-decker complexes functioning as magnets at the single-molecular level. *Journal of the American Chemical Society*, 125(29):8694–8695, 2003. PMID: 12862442.

[43] Naoto Ishikawa, Miki Sugita, and Wolfgang Wernsdorfer. Quantum tunneling of magnetization in lanthanide single-molecule magnets: Bis(phthalocyaninato)terbium and bis(phthalocyaninato)dysprosium anions. *Angewandte Chemie International Edition*, 44(19):2931–2935, 2005.

[44] Tsutomu Yamabayashi, Keiichi Katoh, Brian K. Breedlove, and Masahiro Yamashita. Molecular orientation of a terbium(iii)-phthalocyaninato double-decker complex for effective suppression of quantum tunneling of the magnetization. *Molecules*, 22(6), 2017.

[45] Dante Gatteschi and Roberta Sessoli. Quantum tunneling of magnetization and related phenomena in molecular materials. *Angewandte Chemie International Edition*, 42(3):268–297, 2003.

[46] Javier Tejada, Joan Manel Hernández, Enrique del Barco, and Xi Xiang Zhang. Quantum tunneling of the magnetic moment. *Contributions to Science*, 1:25–38, 1999.

[47] Mickael L. Perrin, Enrique Burzurí, and Herre S. J. van der Zant. Single-molecule transistors. *Chem. Soc. Rev.*, 44:902–919, 2015.

[48] Lidia Rosado Piquer and E. Carolina Sañudo. Heterometallic 3d–4f single-molecule magnets. *Dalton Trans.*, 44:8771–8780, 2015.

[49] George Christou, Dante Gatteschi, David N. Hendrickson, and Roberta Sessoli. Single-molecule magnets. *MRS Bulletin*, 25:66–71, 2000.

[50] Romain Vincent, Svetlana Klyatskaya, Mario Ruben, Wolfgang Wernsdorfer, and Franck Balestro. Electronic read-out of a single nuclear spin using a molecular spin transistor. *Nature*, 488:357–360, 2012.

[51] O. Kahn. *Molecular Magnetism*. VCH, 1993.

[52] Daniel N. Woodruff, Richard E. P. Winpenny, and Richard A. Layfield. Lanthanide single-molecule magnets. *Chemical Reviews*, 113(7):5110–5148, 2013. PMID: 23550940.

[53] E. M. Chudnovsky and L. Gunther. Quantum tunneling of magnetization in small ferromagnetic particles. *Phys. Rev. Lett.*, 60:661–664, Feb 1988.

[54] Humphrey L.C. Feltham and Sally Brooker. Review of purely 4f and mixed-metal nd-4f single-molecule magnets containing only one lanthanide ion. *Coordination Chemistry Reviews*, 276:1–33, 2014.

[55] Naoto Ishikawa, Miki Sugita, Naohiro Tanaka, Tadahiko Ishikawa, Shin-ya Koshihara, and Youkoh Kaizu. Upward temperature shift of the intrinsic phase lag of the magnetization of bis(phthalocyaninato)terbium by ligand oxidation creating an s = 1/2 spin. *Inorganic Chemistry*, 43(18):5498–5500, 2004. PMID: 15332799.

[56] Keiichi Katoh, Yoji Horii, Nobuhiro Yasuda, Wolfgang Wernsdorfer, Koshiro Toriumi, Brian K. Breedlove, and Masahiro Yamashita. Multiple-decker phthalocyaninato dinuclear lanthanoid(iii) single-molecule magnets with dual-magnetic relaxation processes. *Dalton Trans.*, 41:13582–13600, 2012.

[57] Jinkui Tang and Peng Zhang. *Lanthanide Single Molecule Magnets*. Springer, Berlin, Heidelberg, 2015.

[58] Naoto Ishikawa. Single molecule magnet with single lanthanide ion. *Polyhedron*, 26(9):2147–2153, 2007. Proceedings of the 10th International Conference on Molecule-based Magnets (ICMM 2006).

[59] Colette Boskovic, Maren Pink, John C. Huffman, David N. Hendrickson, and George Christou. Single-molecule magnets: Ligand-induced core distortion and multiple jahn−teller isomerism in [mn12o12(o2cme)8(o2pph2)8(h2o)4]. *J. Am. Chem. Soc.*, 123:9914–9915, 2001.

[60] Liuxia Ruan, Junwei Tong, Gaowu Qin, Lianqun Zhou, Xuechen Jiao, and Xianmin Zhang. Magnetic modification and the mechanism of tb-phthalocyanine single molecule magnets prepared by a high yield method. *European Journal of Inorganic Chemistry*, 2020(21):2112–2117, 2020.

[61] R. Rousseau, R. Aroca, and M.L. Rodríguez-Méndez. Extended hückel molecular orbital model for lanthanide bisphthalocyanine complexes. *Journal of Molecular Structure*, 356(1):49–62, 1995.

[62] Jiang Liu, Yan-Cong Chen, Jun-Liang Liu, Veacheslav Vieru, Liviu Ungur, Jian-Hua Jia, Liviu F. Chibotaru, Yanhua Lan, Wolfgang Wernsdorfer, Song Gao, Xiao-Ming Chen, and Ming-Liang Tong. A stable pentagonal bipyramidal dy(iii) single-ion magnet with a record magnetization reversal barrier over 1000 k. *Journal of the American Chemical Society*, 138(16):5441–5450, 2016. PMID: 27054904.

[63] Keiichi Katoh, Yusuke Yoshida, Masahiro Yamashita, Hitoshi Miyasaka, Brian K. Breedlove, Takashi Kajiwara, Shinya Takaishi, Naoto Ishikawa, Hironari Isshiki, Yan Feng Zhang, Tadahiro Komeda, Masakazu Yamagishi, and Jun Takeya. Direct observation of lanthanide(iii)-phthalocyanine molecules on au(111) by using scanning tunneling microscopy and scanning tunneling spectroscopy and thin-film field-effect transistor properties of tb(iii)- and dy(iii)-phthalocyanine molecules. *Journal of the American Chemical Society*, 131(29):9967–9976, 2009.

[64] J. L. Paillaud, M. Drillon, A. De Cian, J. Fischer, R. Weiss, and G. Villeneuve. Radical-based ferromagnetic chain in yttrium diphthalocyanine $[ypc_2]\cdot ch_2\ cl_2$. *Phys. Rev. Lett.*, 67:244–247, Jul 1991.

[65] J.L. Paillaud, M. Drillon, A. Decian, J. Fischer, R. Weiss, R. Poinsot, and A. Herr. Organic ferromagnetic chain in the yttrium diphthalocyanine [ypc2]·ch2cl2: X-ray structure and magnetic behavior. *Physica B: Condensed Matter*, 175(4):337–348, 1991.

[66] Dorsa Komijani, Alberto Ghirri, Claudio Bonizzoni, Svetlana Klyatskaya, Eufemio Moreno-Pineda, Mario Ruben, Alessandro Soncini, Marco Affronte, and Stephen Hill. Radical-lanthanide ferromagnetic interaction in a Tb^{iii} bis-phthalocyaninato complex. *Phys. Rev. Materials*, 2:024405, Feb 2018.

[67] Jun-Bo Lu, David C. Cantu, Manh-Thuong Nguyen, Jun Li, Vassiliki-Alexandra Glezakou, and Roger Rousseau. Norm-conserving pseudopotentials and basis sets to explore

lanthanide chemistry in complex environments. *Journal of Chemical Theory and Computation*, 15(11):5987–5997, 2019. PMID: 31580663.

[68] Lucia Vitali, Stefano Fabris, Adriano Mosca Conte, Susan Brink, Mario Ruben, Stefano Baroni, and Klaus Kern. Electronic structure of surface-supported bis(phthalocyaninato) terbium(iii) single molecular magnets. *Nano Letters*, 8(10):3364–3368, 2008. PMID: 18800852.

[69] Graeme Henkelman, Andri Arnaldsson, and Hannes Jónsson. A fast and robust algorithm for bader decomposition of charge density. *Computational Materials Science*, 36(3):354–360, 2006.

[70] Edward Sanville, Steven D. Kenny, Roger Smith, and Graeme Henkelman. Improved grid-based algorithm for bader charge allocation. *Journal of Computational Chemistry*, 28(5):899–908, 2007.

[71] W Tang, E Sanville, and G Henkelman. A grid-based bader analysis algorithm without lattice bias. *Journal of Physics: Condensed Matter*, 21(8):084204, jan 2009.

[72] U. Fano. Effects of configuration interaction on intensities and phase shifts. *Phys. Rev.*, 124:1866–1878, Dec 1961.

[73] Kwangwoo Hong and Woo Youn Kim. Fano-resonance-driven spin-valve effect using single-molecule magnets. *Angewandte Chemie International Edition*, 52(12):3389–3393, 2013.

[74] Igor V. Krainov, Janina Klier, Alexander P. Dmitriev, Svetlana Klyatskaya, Mario Ruben, Wolfgang Wernsdorfer, and Igor V. Gornyi. Giant magnetoresistance in carbon nanotubes with single-molecule magnets tbpc2. *ACS Nano*, 11(7):6868–6880, 2017. PMID: 28613829.

[75] P. Jarillo-Herrero, S. Sapmaz, C. Dekker, et al. Electron-hole symmetry in a semiconducting carbon nanotube quantum dot. *Nature*, 409:389–392, 2004.

[76] Zhizhou Yu, Jian Chen, Lei Zhang, and Jian Wang. First-principles investigation of quantum transport through an endohedral n@c60in the coulomb blockade regime. *Journal of Physics: Condensed Matter*, 25(49):495302, nov 2013.

[77] Bo Song, Dmitry A. Ryndyk, and Gianaurelio Cuniberti. Molecular junctions in the coulomb blockade regime: Rectification and nesting. *Phys. Rev. B*, 76:045408, Jul 2007.

[78] Zhi Yang, Baolong Zhang, Xuguang Liu, Xiuyan Li, Yongzhen Yang, Shijie Xiong, and Bingshe Xu. Size-dependent magnetic order and giant magnetoresistance in organic titanium–benzene multidecker cluster. *Phys. Chem. Chem. Phys.*, 16:1902–1908, 2014.

[79] Stefan Schmaus, Alexei Bagrets, Yasmine Nahas, Toyo K. Yamada, Annika Bork, Martin Bowen, Eric Beaurepaire, Ferdinand Evers, and Wulf Wulfhekel. Giant magnetoresistance through a single molecule. *Nature Nanotechnology*, 6:185–189, 2011.

[80] Norbert Nemec. *Quantum Transport in Carbon-based Nanostructures*. PhD thesis, Universität Regensburg, 7 2007.

[81] Matías Zilly. *Electronic conduction in linear quantum systems: Coherent transport and the effects of decoherence*. PhD thesis, Universität Duisburg-Essen, 4 2010.

[82] Andrey E. Miroshnichenko, Sergei F. Mingaleev, Sergej Flach, and Yuri S. Kivshar. Nonlinear fano resonance and bistable wave transmission. *Phys. Rev. E*, 71:036626, Mar 2005.

[83] Baogang Zhu, Rong Lü, and Shu Chen. Interplay between fano resonance and $\mathcal{PT}$ symmetry in non-hermitian discrete systems. *Phys. Rev. A*, 91:042131, Apr 2015.

[84] Ajith Ramachandran, Carlo Danieli, and Sergej Flach. Fano resonances in flat band networks. 01 2018.

[85] Peiqing Tong, Baowen Li, and Bambi Hu. Wave transmission, phonon localization, and heat conduction of a one-dimensional frenkel-kontorova chain. *Phys. Rev. B*, 59:8639–8645, Apr 1999.

[86] Andrey E. Miroshnichenko, Sergej Flach, and Yuri S. Kivshar. Fano resonances in nanoscale structures. *Rev. Mod. Phys.*, 82:2257–2298, Aug 2010.

[87] J.C. Cuevas and E. Scheer. *Molecular Electronics: An Introduction to Theory and Experiment*. EBSCO ebook academic collection. World Scientific Publishing Company Pte Limited, 2010.

[88] Sander J. Tans, Michel H. Devoret, Hongjie Dai, Andreas Thess, Richard E. Smalley, L. J. Geerligs, and Cees Dekker. Individual single-wall carbon nanotubes as quantum wires. *Nature*, 386, 1998.

[89] Joost VandeVondele and Jürg Hutter. Gaussian basis sets for accurate calculations on molecular systems in gas and condensed phases. *The Journal of Chemical Physics*, 127(11):114105, 2007.

[90] Qin Wu and Troy Van Voorhis. Constrained density functional theory and its application in long-range electron transfer. *Journal of Chemical Theory and Computation*, 2(3):765–774, 2006. PMID: 26626681.

[91] Nico Holmberg and Kari Laasonen. Efficient constrained density functional theory implementation for simulation of condensed phase electron transfer reactions. *Journal of Chemical Theory and Computation*, 13(2):587–601, 2017. PMID: 28009515.

[92] Anna Płomińska and Ireneusz Weymann. Tunnel magnetoresistance of a supramolecular spin valve. *EPL (Europhysics Letters)*, 125(1):18004, feb 2019.

[93] Wenjie Liang, D. Bockrath M., Bozovic, et al. Fabry - perot interference in a nanotube electron waveguides. *Nature*, 411:665–669, 2001.

[94] Jesper Nygård, David Henry Cobden, and Poul Erik Lindelof. Kondo physics in carbon nanotubes. *Nature*, 408:342–346, 2000.

[95] J. Appenzeller, R. Martel, Ph. Avouris, H. Stahl, U. Th. Hunger, and B. Lengeler. Phase-coherent transport in ropes of single-wall carbon nanotubes. *Phys. Rev. B*, 64:121404, Sep 2001.

[96] Arieh Aviram and Mark A. Ratner. Molecular rectifiers. *Chemical Physics Letters*, 29(2):277–283, 1974.

[97] Bernhard Mann and Hans Kuhn. Tunneling through fatty acid salt monolayers. *Journal of Applied Physics*, 42(11):4398–4405, 1971.

[98] Wenjie Liang, Matthew P. Shores, and Marc Bockrath. Kondo resonance in a single-molecule transistor. *Nature*, 417:1476–4687, 2002.

[99] C. Joachim, J. K. Gimzewski, and A. Aviram. Electronics using hybrid-molecular and mono-molecular devices. *Nature*, 408:1476–4687, 2000.

[100] Artem Fediai, Dmitry A. Ryndyk, Gotthard Seifert, Sven Mothes, Martin Claus, Michael Schröter, and Gianaurelio Cuniberti. Towards an optimal contact metal for cntfets. *Nanoscale*, 8:10240–10251, 2016.

[101] Rolf Landauer. Electrical resistance of disordered one-dimensional lattices. *The Philosophical Magazine: A Journal of Theoretical Experimental and Applied Physics*, 21(172):863–867, 1970.

[102] K. S. Novoselov, A. K. Geim, S. V. Morozov, D. Jiang, Y. Zhang, S. V. Dubonos, I. V. Grigorieva, and A. A. Firsov. Electric field effect in atomically thin carbon films. *Science*, 306(5696):666–669, 2004.

[103] A Celis, M N Nair, A Taleb-Ibrahimi, E H Conrad, C Berger, W A de Heer, and A Tejeda. Graphene nanoribbons: fabrication, properties and devices. *Journal of Physics D: Applied Physics*, 49(14):143001, mar 2016.

[104] P. Umari, O. Petrenko, S. Taioli, and M. M. De Souza. Communication: Electronic band gaps of semiconducting zig-zag carbon nanotubes from many-body perturbation theory calculations. *The Journal of Chemical Physics*, 136(18):181101, 2012.

[105] Min Ouyang, Jin-Lin Huang, Chin Li Cheung, and Charles M. Lieber. Energy gaps in "metallic" single-walled carbon nanotubes. *Science*, 292(5517):702–705, 2001.

[106] Stephen Hill, Saiti Datta, Junjie Liu, Ross Inglis, Constantinos J. Milios, Patrick L. Feng, John J. Henderson, Enrique del Barco, Euan K. Brechin, and David N. Hendrickson. Magnetic quantum tunneling: insights from simple molecule-based magnets. *Dalton Trans.*, 39:4693–4707, 2010.

[107] Ali K. Ismael, Iain Grace, and Colin J. Lambert. Connectivity dependence of fano resonances in single molecules. *Phys. Chem. Chem. Phys.*, 19:6416–6421, 2017.

[108] Christoph Schlegel. *Quantum Coherence in Molecular Magnets*. PhD thesis, Universität Stuttgart, 10 2009.

[109] Joris van Slageren. Introduction to molecular magnetism.

[110] Ajith Ramachandran, Carlo Danieli, and Sergej Flach. Fano resonances in flat band networks, 2018.